

1 **Redox-sensitive partitioning of vanadium and other heterovalent elements between apatite and**  
2 **biotite in high silica magmas**

3 Peteris Rozenbaks\* and James M. Brenan

4 *Department of Earth and Environmental Sciences, Dalhousie University, Halifax, Canada*

5 *\*Corresponding author*

6 *E-mail address: peteris.rozenbaks@dal.ca*

7  
8 **Abstract**

9 Apatite and biotite, ubiquitous minerals in a multitude of natural rocks, host a variety of  
10 trace elements, including those whose valence state, and hence ionic radius and charge, can vary  
11 over the oxygen fugacity ( $fO_2$ ) of natural magmatic systems. In this study, we determine trace  
12 element partition coefficients (concentration [C] ratios) between apatite and biotite ( $D^{ap/bt} =$   
13  $C^{apatite}/C^{biotite}$ ) in five suites of natural, mostly silicic, metaluminous to peraluminous rocks that  
14 formed under reduced to oxidized conditions (FMQ-3.6 to +6.2; FMQ = fayalite-magnetite-quartz  
15 buffer). In three of the suites, representing a narrower  $fO_2$  range (FMQ-3.6 to 2.9), trace element  
16 apatite/glass and biotite/glass partitioning coefficients ( $D^{ap/gl} = C^{apatite}/C^{glass}$  and  $D^{bt/gl} = C^{biotite}/C^{glass}$ ,  
17 respectively) were also determined. Elements considered include alkalis, alkaline earths, rare earth  
18 elements, transition metals, metalloids, and high field strength elements, of which V, As, Eu, Mo, Sn,  
19 and W are expected to be heterovalent over the  $fO_2$  range considered.

20 Results reveal changes in partitioning behavior of the heterovalent elements over the  $fO_2$   
21 range. With increasing  $fO_2$  from FMQ-3.6 to FMQ+2.9, values of  $D^{bt/gl}$  for V decrease from ~580 to  
22 ~50 whereas  $D^{ap/gl}$  increases from ~0.5 to ~5. Arsenic becomes more compatible in apatite with  
23  $D^{ap/gl}$  increasing from ~0.04 to ~1.6. Europium  $D^{ap/gl}$  values increase from ~20 to ~90. Molybdenum  
24  $D^{bt/gl}$  decreases from ~2 to ~0.1. Tin becomes more compatible with both minerals as  $fO_2$  increases,  
25 with  $D^{bt/gl}$  increasing from ~0.1 to ~1.0 and  $D^{ap/gl}$  from ~0.05 to ~0.3. Although the uncertainty on  
26  $D^{ap/gl}$  for W is too large to derive a meaningful  $fO_2$  relation, values for  $D^{bt/gl}$  decrease from ~0.13 to  
27 ~0.02 with increasing  $fO_2$ . As a result of  $D^{ap/gl}$  and  $D^{bt/gl}$  for V exhibiting opposite relations with  $fO_2$ ,  
28 values of apatite/biotite partitioning ( $D^{ap/bt}$ ) systematically increase from ~0.001 to ~0.5 with  
29 increase in  $fO_2$ . In addition to shifts in the relative proportions of oxidized and reduced species with

30  $fO_2$ , the observed partitioning relations for heterovalent elements could be caused by differences in  
31 other parameters that affect the activity of single species, species proportions, temperature, etc.  
32 These confounding aspects are assessed by comparison of the homovalent element partitioning  
33 data, which are relatively constant for the investigated samples, with the exception of the Mascota  
34 suite (Mexico). We suggest that  $D^{ap/bt}$  values for V in the Mascota suite are likely enhanced by the  
35 stabilization of higher valence V species in a more alkaline melt composition. Results therefore  
36 indicate that the observed variation in heterovalent element partitioning is predominantly the result  
37 of  $fO_2$  control on element species and corresponding ionic radius. With this interpretation, we  
38 present a preliminary V partitioning model that considers changes in the proportion of V species  
39 with  $fO_2$  and estimated values  $D^{ap/bt}$  for V species. Model results are used to estimate the  $fO_2$  of the  
40 peraluminous South Mountain Batholith (Nova Scotia, Canada) for which oxybarometry has not  
41 been straightforward. Estimated oxygen fugacities are consistent with other redox indications,  
42 however, other factors, including melt and biotite composition, need to be considered to enable  
43 general application of the model. The partitioning of V between apatite and ferromagnesian  
44 minerals has the potential of a novel oxybarometer, applicable to a broad range of igneous rocks,  
45 including Fe-Ti poor plutonic systems.

46       Keywords: apatite, biotite, vanadium, partitioning, trace element

47

## 48 **1. Introduction**

49       Oxygen fugacity ( $fO_2$ ) is one of the fundamental thermodynamic variables in geological  
50 systems as it drives redox reactions and controls phase stability (Frost, 1991). This in turn impacts  
51 aspects such as the mineral paragenesis, rock solidus, magma and ore genesis, composition of fluids  
52 and the mass transfer between solar system reservoirs (Gaillard et al., 2015; Moretti & Neuville,  
53 2021; Mungall, 2002; Taylor & Green, 1988). For heterovalent elements, oxygen fugacity is also  
54 linked to the identity and relative proportions of chemical species through redox reactions  
55 (Carmichael & Ghiorso, 1990). Because each element species has a specific charge and radius, a  
56 unique partitioning behavior between coexisting phases could result. Thus, with proper calibration,  
57 heterovalent element partitioning can be used as a proxy for igneous  $fO_2$  (Arató & Audétat, 2017c;  
58 Ballhaus et al., 1991; Burnham et al., 2015; Mallmann & O'Neill, 2013; Smythe & Brenan, 2015).

59           Among the suite of trace elements in natural igneous systems, vanadium (V) is somewhat  
60 unique as it can exist in four valence states:  $V^{2+}$ ,  $V^{3+}$ ,  $V^{4+}$ ,  $V^{5+}$  (Sutton et al., 2005). At the most  
61 common geological redox conditions of  $\pm 2$  log units relative to the fayalite-magnetite-quartz (FMQ)  
62 redox buffer (Cottrell et al., 2021), most of the V is speciated as  $V^{3+}$  and  $V^{4+}$  (Canil, 1999). These two  
63 species are expected to have similar partitioning behavior to  $Fe^{3+}$  and  $Ti^{4+}$  due to the same valence  
64 and similar ionic radii (IR): 0.064 nm<sup>1</sup> ( $V^{3+}$ ), similar to 0.0645 nm ( $Fe^{3+}$ ) and 0.058 nm ( $V^{4+}$ ), similar to  
65 0.0605 nm ( $Ti^{4+}$ ). Thus,  $V^{3+}$  is most compatible with  $Fe^{3+}$ -bearing phases (clinopyroxene, magnetite)  
66 and  $V^{4+}$  preferentially enters the titaniferous oxide minerals (Arató & Audétat, 2017b; Mallmann &  
67 O'Neill, 2009). Similarly,  $V^{2+}$  mimics  $Fe^{2+}$  due to the same charge and near-identical radii (0.079 and  
68 0.078 nm, respectively) resulting in high compatibility in ferromagnesian minerals, although this V  
69 species is sparse in terrestrial magmas (Sutton et al., 2005). Pentavalent vanadium, the dominant V  
70 species in highly oxidized conditions  $>FMQ+4$  (Sossi et al., 2018), is similar to other highly charged  
71 ions ( $Nb^{5+}$ ,  $Ta^{5+}$ ) and therefore is expected to accumulate in the melt phase as its size and charge  
72 make it generally incompatible with igneous rock forming mineral structures (summarized in  
73 Ballouard et al., 2020). This rich variety of V species and partitioning behaviors has enabled several  
74 experimentally calibrated V oxybarometers for mineral-melt systems that link V partitioning to  
75 magmatic redox state (Arató & Audétat, 2017c; Holycross & Cottrell, 2020, 2022; Mallmann &  
76 O'Neill, 2013; Sossi et al., 2018).

77           The application of mineral-melt oxybarometers, however, is often precluded by poorly  
78 constrained or absent melt composition estimates (e.g., in hypabyssal and plutonic systems).  
79 Therefore, oxybarometers involving intermineral partitioning are of use in systems for which the  
80 melt phase cannot be characterized. In moderately oxidized, iron-bearing igneous rocks, oxygen  
81 barometry involving coexisting cubic and rhombohedral oxides has been widely employed (Ghiorso  
82 & Evans, 2008; Ghiorso & Sack, 1991). Unfortunately, this method can be infeasible for many  
83 systems (e.g. chemically evolved granites, carbonatites) which are too iron-poor or have otherwise  
84 formed outside the stability field of coexisting oxides. Therefore, the development of  
85 oxybarometers involving heterovalent element partitioning between other rock-forming minerals is

---

<sup>1</sup> Unless otherwise specified, ionic radii (IR) are from Shannon (1976)

86 desirable. As a recent example, Holycross and Cottrell (2022) demonstrated systematic changes in  
87 rutile/clinopyroxene and rutile/garnet partitioning of V over a large  $fO_2$  range, and therefore the  
88 potential for oxybarometry in appropriate bulk compositions (i.e., eclogites). The changes in  
89 intermineral partitioning documented by Holycross and Cottrell (2022) are due to the unique  
90 behavior of rutile, and its preferential acceptance of the  $V^{5+}$  species, which is otherwise  
91 incompatible in ferromagnesian minerals. From the consideration of cation radius and charge of V  
92 species, as described below, we expect that apatite behaves in a similar way to rutile, with a  
93 preference for pentavalent V. Owing to its ubiquity in intermediate to felsic igneous rocks, and its  
94 common coexistence with apatite (Clarke et al., 2021), we have focused in this case on biotite to  
95 complete the intermineral partitioning pair.

96 Apatite, with the formula  $Ca^{IX}_4Ca^{VII}_6(P^{IV}O_4)_6(F,OH,Cl)_2$ , comprises a group of phosphate  
97 minerals, with three available cation sites (IV-, VII- and IX-fold), and most igneous endmembers  
98 distinguished by the occupant of the anion site (OH, Cl, F). In the VII- and IX-fold cation sites,  $Ca^{2+}$  is  
99 commonly substituted with  $Sr^{2+}$ ,  $Pb^{2+}$ ,  $Na^+$ ,  $REE^{3+}$ , and other similarly-sized cations (Pan and Fleet,  
100 2002), which are significantly larger ( $> 0.1$  nm) than any of the V species. However,  $V^{5+}$  may be  
101 compatible in the apatite structure as the oxyanion  $(VO_4)^{-3}$  substituted for  $(PO_4)^{-3}$ , as evidenced by the  
102 complete solid solution series between  $Ca_{10}(PO_4)_6F_2$  and  $Ca_{10}(VO_4)_6F_2$  confirmed by Kreidler &  
103 Hummel (1970). Biotite is a trioctahedral mica, represented by solid solution between the ferruginous  
104 annite,  $K^{XII}Fe^{VI}_3(AlSi_3)^{IV}O_{10}(OH,F,Cl)_2$ , and magnesian phlogopite,  $K^{XII}Mg^{VI}_3(AlSi_3)^{IV}O_{10}(OH,F,Cl)_2$ ,  
105 endmembers. In its octahedral site, common replacements include  $Al^{3+}$  (eastonite-siderophyllite  
106 substitution),  $Fe^{3+}$  and  $Ti^{4+}$  (Dymek, 1983), suggesting that  $V^{2+}$ ,  $V^{3+}$ , and  $V^{4+}$  could likewise be  
107 compatible. As demonstrated by Gao et al. (2023), although the pentavalent cations  $Nb^{5+}$  and  $Ta^{5+}$   
108 exhibit some level of compatibility in biotite ( $D_{Nb,Ta}^{bt/gl}$  of  $\sim 0.05$  to 3), values of  $D_{Ti^{4+}}^{bt/gl}$  are at least  
109 10x larger, therefore  $V^{5+}$  is expected to be the least compatible V species.

110 As oxidizing conditions increase the relative abundance of high-valence V species, enhanced  
111 partitioning of V into apatite over biotite is anticipated, thus linking  $D_{zV}^{ap/bt}$  to the igneous  $fO_2$  in a  
112 positive correlation. Pentavalent V is expected to have the highest D value for distribution between  
113 apatite and biotite, owing to its stability in the apatite structure as the  $(VO_4)^{-3}$  oxyanion. With  
114 decreasing charge and increasing ionic radius, other V species are generally expected to become

115 progressively less compatible in the apatite structure and more compatible in biotite, thus resulting in  
116 decreasing D values. The bulk distribution of all V species,  $D_{2V}^{ap/bt}$  is therefore dependent on the  
117 igneous speciation of V, which is controlled by the magmatic  $fO_2$  (Sutton et al., 2005). We test this  
118 hypothesis by measuring the partitioning of V and other trace elements, including those with several  
119 valence states, between apatite and biotite in natural igneous systems formed over a wide range of  
120 oxygen fugacity. Furthermore, to determine the redox sensitivity of the mineral/melt partitioning, D  
121 values for apatite/glass and biotite/glass partitioning were also determined.

## 122 **2. Materials and methods**

### 123 **2.1 Sample suites**

124 Samples of five, previously well-described volcanic and plutonic rock suites were analyzed in  
125 this study:

- 126 1) Picotani intrusive suite (sampled at the Revancha dyke and the Cerro Esquinani stock),  
127 related to the Macusani volcanics, southeastern Peru (Sandeman et al., 1997),
- 128 2) Tuk-Tuk dome, related to the Youngest Toba tuff member, Sumatra, Indonesia (Chesner  
129 et al., 2020),
- 130 3) Fish Canyon tuff, Colorado, USA (Whitney & Stormer, 1985),
- 131 4) Mascota minette, Jalisco, Mexico (Carmichael et al., 1996), and
- 132 5) Umiakovik pluton of the Nain intrusive suite, Labrador, Canada (Emslie & Stirling, 1993).

133 The relevant characteristics of the sample suites are provided in Table 1. The suites were  
134 selected based on the criteria that they contain unaltered biotite and apatite in a textural  
135 association suggesting phase equilibrium (i.e., planar contacts, lack of reaction textures). Except for  
136 the samples from Umiakovik and Mascota, all others contain a vitreous matrix, which enables  
137 determination of mineral-melt partitioning. Also considered is that other intensive parameters,  
138 including crystallization temperature (T) and oxygen fugacity are reasonably well known and span a  
139 sufficiently large range that meaningful relations between  $fO_2$  and partitioning of redox-sensitive  
140 elements could be obtained. Independent estimates of  $fO_2$  have been published for all the suites  
141 except the Macusani subvolcanics, in which the  $fO_2$  was determined in this study using the zircon  
142 Ce-U-Ti oxybarometer (Loucks et al., 2020). Estimated oxygen fugacities range from ~FMQ-3.6

143 (Macusani subvolcanics) to FMQ+6.2 (Mascota minette) and temperatures of 700-800°C (Table 1).  
144 Compositionally, samples range in whole-rock silica content from 48.7 to 73.2, and are  
145 metaluminous to strongly peraluminous with A/CNK (molar ratio  $Al_2O_3/[CaO+Na_2O+K_2O]$ ) values of  
146 0.5-1.2 (note that the glass analyses, reported below somewhat differ from these whole-rock values  
147 due to the presence of phenocrysts).

148 Samples were received from several collections. A Fish Canyon tuff hand sample from the  
149 classic sampling locality in a road cut on Colorado (USA) Highway 160 (Gleadow et al., 2015) was  
150 provided by Dr. Ray Donelick (Apatite.com Partners LLC). Three samples of Macusani subvolcanics  
151 were sourced from several collections – MAC137 (Revancha dyke) and MAC160 (Cerro Esquinani  
152 stock) hand samples were received from Dr. John Hanchar (Memorial University of Newfoundland)  
153 and MAC2 thin sections (Revancha dyke) from Dr. Hamish Sandeman (Geological Survey of  
154 Newfoundland and Labrador). A Mascota minette sample was selected from the collection of the  
155 Smithsonian Institution (catalog number NMNH 117626-21). Two samples of Tuk-Tuk tuff (TT and  
156 TT7), related to the Younger Toba tuff, were provided by Dr. Craig Chesner (Eastern Illinois  
157 University). Material from the Umiakovik Pluton were received as mineral separates from the  
158 Geochronology Laboratory Archive of the Geological Survey of Canada (sample EC-87-119, database  
159 number Z1280).

160 As-received rock hand samples were split into cm-sized fragments, and both rock fragments  
161 and mineral separates were mounted in 1" epoxy pucks, which were then prepared by grinding with  
162 progressively finer SiC grit, followed by 1 micron, then 0.3 micron alumina powder. Polished sections  
163 (100 micron thick) of the Mascota minette were prepared in the Petrography Laboratory at Saint  
164 Mary's University (Halifax, Canada). Sample billets for polished thick sections were lapped flat and  
165 mounted to frosted glass slides using epoxy. Sections were cut and lapped to ~100 microns thick,  
166 then polished using monocrystalline diamond suspensions down to 3 micron particle size. Final  
167 polishing was performed using 0.06 micron amorphous colloidal silica suspension.

## 168 **2.2. Analytical methods**

169 Reflected light image sample maps at a magnification of 2x were acquired by digital image  
170 acquisition of the entire mounts. Areas of particular interest were then investigated by imaging at

171 higher magnifications. High spatial resolution textural observations and some semi-quantitative  
172 chemical data on apatite, biotite and glass were obtained using a TESCAN MIRA 3 LMU Variable  
173 Pressure Schottky Field Emission Scanning Electron Microscope (SEM) at Saint Mary's University  
174 (Halifax, Canada). A beam voltage of 20 kV, beam current of 0.2 nA and an approximate working  
175 distance of 17 mm were used for all EDS spot analyses and imaging. The reflected light and  
176 backscattered electron images were used to identify mineral textures and morphology to select  
177 areas for further chemical analysis. Individual mineral grains were selected based on lack of zoning  
178 or an outer uniform zone being at least 25  $\mu\text{m}$  thick. Similarly, for matrix glass analysis, areas larger  
179 than 25  $\mu\text{m}$  and devoid of microcrysts were selected.

180 The major element composition of the mineral and glass phases was determined using the  
181 JEOL JXA-8230 Electron Probe Micro-Analyzer (EPMA) at the University of Toronto. Analytes and the  
182 phase-specific routine analytical conditions are summarized in Table 2. The spectral interference  
183 from the Fe  $L\alpha_{1,2}$  emission line (705 eV) on the F  $K\alpha$  line (676.8 eV) was determined by measuring  
184 the F  $ka$  intensity in Fe-metal, which was then used to calculate an appropriate correction factor.  
185 Analysis of Fe metal yielded F concentrations below detection limit ( $\leq 0.02$  wt%), confirming the  
186 efficacy of this correction method. Analytical accuracy was checked by analysis of fused beads of  
187 basalt reference materials BIR-1, BHVO-1 and a fragment of rhyolite glass CAM66. For BIR-1 and  
188 BHVO-1 the relative difference between the reported and measured values did not exceed 5% for  
189 oxides of  $>1$  wt.% abundance. For CAM66, the relative difference was  $<1\%$  for  $\text{SiO}_2$ ,  $\text{Al}_2\text{O}_3$ ,  $\text{K}_2\text{O}$   
190 (above 4 wt.%) and  $<15\%$  for FeO, CaO,  $\text{Na}_2\text{O}$  (above 1 wt.%). Although not certified standards, we  
191 also analyzed fragments of San Carlos biotite (Righter and Carmichael, 1996) and Durango apatite as  
192 checks on accuracy and reproducibility between analytical sessions. For San Carlos biotite, the  
193 relative difference between the reported (Righter & Carmichael, 1996) and measured values was  
194  $<3.6\%$  for oxides above 0.2 wt.%. For Durango apatite, the relative difference between the reported  
195 (Young et al., 1969) and measured values was  $<0.05\%$  for CaO and  $\text{P}_2\text{O}_5$ , 5.2% for F,  $<3.5\%$  for  $\text{SiO}_2$   
196 and Cl. Detailed precision and accuracy estimates are summarized in the Table ST1.

197 Trace element concentrations of apatite, biotite, and glass were determined using the laser  
198 ablation ICP-MS facility located in the Health and Environments Research Centre (HERC) Laboratory  
199 at Dalhousie University. The system employs a frequency quintupled Nd:YAG laser operating at 213

200 nm, coupled to a Thermo Scientific iCAP Q quadrupole mass spectrometer with He flushing the  
201 ablation cell to enhance sensitivity (Eggins et al., 1998). Zircon from the Macusani suite of samples  
202 was analyzed at the Micro-Analysis of Natural Trace-element and Isotope Systematics (MANTIS)  
203 laboratory at University of New Brunswick. The system employs an ArF laser operating at 193 nm,  
204 coupled to Agilent 7700x quadrupole mass-spectrometer using a mixture of He, Ar, and N as the  
205 carrier gas as described by McFarlane & Luo (2012). The details of all the trace element analyses are  
206 provided in Table 2. Each analytical session involved initial tuning using the NIST 610 glass reference  
207 material, using  $^{115}\text{In}$  to maximize sensitivity,  $^{248}\text{ThO}/^{232}\text{Th}$  of  $<0.005$  to minimize oxide production  
208 and  $^{238}\text{U}/^{232}\text{Th}$  of  $\sim 1$  to monitor mass fractionation. Where possible, the analyses were carried out  
209 in traverse track configuration to improve the signal stability. Factory supplied time resolved  
210 software was utilized for the acquisition of individual analyses. A typical analysis involved 20  
211 seconds of background acquisition with the ablation cell being flushed with the carrier gas, followed  
212 by laser ablation for 60 seconds, then 40-60 seconds of cell washout. Analyses were collected in a  
213 sequence in which two analyses were done on the NIST 610 standard reference material at the start  
214 of the acquisition cycle, then after every 20 analyses on the unknowns including secondary  
215 standards.

216 All LA-ICP-MS data reduction was done off-line using the Lolite version 4.0 software package  
217 (Paton et al., 2011). Time-resolved signals were individually examined based on the major elements  
218 in each phase and marker elements of potential contaminants – Na and K for glass and alkali  
219 feldspars, Ca for apatite, hornblende, and plagioclase, Ti for ilmenite, Zr for zircon, REE for monazite.  
220 Narrow spikes and otherwise anomalous spectra of the potential contaminant elements were used  
221 as indicators of signal impurity from inclusions or adjacent phases. Spikes near the margins of  
222 spectra were excluded by narrowing the signal selection, whereas the spectra containing multiple  
223 spikes were discarded. Spectra with abnormal features were also discarded if the extracted  
224 compositions deviated by  $>2$  standard deviations from the mean content of the markers of the  
225 potential contamination. Ablation yields were corrected by referencing to the EPMA-measured  
226 concentration of internal standards (Table 2). As V is an element of especial interest in this study,  
227 care was made to consider and resolve any significant analytical interferences with isobaric species  
228 that could affect analytical accuracy. Specific to halogen-bearing minerals like apatite and biotite is

229 the possibility of the  $^{35}\text{Cl}\text{-}^{16}\text{O}$  molecule on  $^{51}\text{V}$ . The magnitude of this interference was assessed by  
230 analyzing a synthetic endmember Cl-apatite (containing 6.81 wt% Cl; provided by John Hanchar,  
231 Memorial University), which was assumed to be vanadium-free. The calculated V concentration of  
232 this material, considered to be wholly from the  $^{35}\text{Cl}\text{-}^{16}\text{O}$  interference, is  $\sim 1.3 \mu\text{g/g}$ , resulting in a  
233 contribution of  $\sim 0.2 \mu\text{g/g/wt\% Cl}$ . The highest Cl concentrations in measured phases are 0.84 wt%  
234 in apatite (FCT), 0.24 wt% in biotite (Tuk-Tuk tuff) and 0.12 wt% in glass (FCT), resulting in maximum  
235 interference contributions of 0.16, 0.05 and 0.02  $\mu\text{g/g}$  in apatite, biotite and glass, respectively.  
236 Reported V concentrations reflect this minor correction. The measurement of accurate titanium  
237 concentrations in phosphate minerals is complicated by the polyatomic interferences of  
238 phosphorous oxides ( $^{31}\text{P}^{16}\text{O}^+$  for  $^{47}\text{Ti}$  and  $^{31}\text{P}^{18}\text{O}^+$  for  $^{49}\text{Ti}$ ). This was important to this study, as the  
239 partitioning of  $\text{Ti}^{4+}$  is considered a surrogate for  $\text{V}^{4+}$  applied to the vanadium partitioning model  
240 developed in subsequent sections. To estimate the potential interference, we carried out additional  
241 measurements of reagent grade hydroxyapatite powder (18.49 wt% P) containing 2.8  $\mu\text{g/g}$  Ti (Sigma  
242 Aldrich Certificate of Analysis). For this material, 10 analyses produced mean values of 80.1  $\mu\text{g/g}$  for  
243 mass 47 and 3.0  $\mu\text{g/g}$  for mass 49. The latter result is consistent with the Certificate of Analysis,  
244 indicating a minimal contribution from the  $^{31}\text{P}^{18}\text{O}^+$  interference. Furthermore, the mean background  
245 corrected signal for mass 47 is 2089 cps, but for mass 49 is 31 cps. Given the natural  $^{16}\text{O}$  to  $^{18}\text{O}$   
246 abundances (99.76% to 0.2%), the expected oxide contribution to the mass 49 signal is 4 cps, which  
247 amounts to a correction of 0.1  $\mu\text{g/g}$  for Ti in apatite analyses. Hence, we conclude that the signal for  
248 mass 47 in the apatite analyses is indeed almost entirely produced by  $^{31}\text{P}^{16}\text{O}^+$ , and the effect of  
249  $^{31}\text{P}^{18}\text{O}^+$  on the signal for mass 49 is negligible.

250 Comparison between the measured and reported values for secondary standards yields  
251 average relative differences of  $\sim 7\%$  for BIR-1 and BHVO-1 (Jochum et al., 2005) and  $\sim 14\%$  for  
252 Durango apatite (Marks et al., 2012). Measurements of our Durango apatite fragment were cross-  
253 verified against the specimen at the MANTIS lab, with the median relative differences being  $\sim 4.6\%$ .  
254 Summaries of the major and trace element concentrations of the analyzed phases are provided in  
255 the Tables ST1 and ST2, respectively.

## 256 **3. Results**

### 257 **3.1 Phase assemblage and textures**

258 *Fish Canyon tuff* is sampled at its relatively lithic-rich, lower part of the thick proximal  
259 vitrophyre ignimbrite. The sample consists of plagioclase, sanidine, biotite, hornblende, quartz,  
260 magnetite, titanite, and ilmenite phenocrysts in a matrix of microcrysts, phenocryst fragments, and  
261 glass. The relative proportions within the phenocryst assemblage in the sample are close to the ones  
262 reported by Whitney and Stormer (1985) - ~55% plagioclase, ~15% alkali feldspar, 10% biotite, 10%  
263 hornblende, 5% quartz, 5% trace minerals. The matrix is predominantly composed of glass shards,  
264 crystal and pumice fragments, devitrified glass with several pockets of massive, fresh glass. Biotite is  
265 typically fresh, euhedral, often kinked, and compositionally uniform (Figure 1a), often contains  
266 inclusions of apatite, Fe-Ti oxides, and zircon. Apatite is present as up to 300  $\mu\text{m}$  long, euhedral,  
267 equant to tabular phenocrysts and biotite-hosted inclusions. Texturally, apatite crystals are uniform,  
268 featuring few inclusions of zircon and Fe-Ti oxides.

269 *Macusani subvolcanics* comprise samples from the Revancha dyke and the Cerro Esquinani  
270 stock, which consist of plagioclase, sanidine, biotite phenocrysts with trace amounts of monazite,  
271 apatite, ilmenite, and zircon set in a massive, uniform holohyaline matrix without any macroscopic  
272 evidence of weathering or hydrothermal alteration. The Revancha dike exhibits a glass-rich (up to 74  
273 vol%) margin (represented by MAC2) and a crystal-rich (up to 50 vol%) porphyritic interior,  
274 separated by a flow-banded facies with an intermediate glass content (represented by MAC137;  
275 Sandeman & Clark, 2003). MAC137 (Figure 1b) is rich in biotite phenocrysts and microphenocrysts,  
276 typically reverse-zoned, particularly the older, larger phenocrysts, which commonly exhibit  
277 resorption features. Iron numbers (molar  $\text{Fe}/[\text{Fe}+\text{Mg}]$ ; Fe#) of the analyses bt02 (rim) and bt03  
278 (interior, Figure 1b) are 0.48 and 0.51 respectively. The smaller biotite microphenocrysts, however,  
279 are euhedral and lack zoning. Apatite is euhedral to subhedral, commonly equant, texturally  
280 uniform without obvious zoning. Apatite crystals are present as microphenocrysts and biotite-  
281 hosted inclusions. Apatite phenocrysts, up to hundreds of microns in size, host ubiquitous melt,  
282 zircon, ilmenite, and monazite inclusions (Figure 1 c,d), few crystals feature inherited cores (Fig. 1e).  
283 Mineral textures in the more crystal-poor MAC2 (Figure 1c) are generally the same as in MAC137.  
284 Glass in both samples is unaltered, but rich in microlites with a few clear areas, typically surrounded

285 by perlitic cracks. In the Cerro Esquinani stock sample (MAC160), biotite is unzoned, with some  
286 occurrences of partial resorption. Both apatite and zircon are present, but less abundant in Cerro  
287 Esquinani than in the Revancha dyke. Zircon is rare, occurring as small (<30  $\mu\text{m}$ ), euhedral  
288 microphenocrysts and as inclusions in other minerals (Supplementary Figure S1). Typical of igneous  
289 zircons, the zircon grains exhibit concentric growth and sector zoning; inherited cores  
290 (Supplementary Figure S1a) are comparatively uncommon.

291 *Tuk-Tuk tuff* samples are light gray-to-white, vesicular (6-7 vol%; Figure 1e), comprised of  
292 glass (47-72 vol%), quartz (6-12 vol%), sanidine (1-12 vol%), plagioclase (9-34 vol%), biotite (1-4  
293 vol%), and hornblende ( $\leq 2$  vol%) with trace amounts of zircon, allanite, magnetite, ilmenite,  
294 orthopyroxene, and apatite (Chesner et al., 2020). Biotite in both samples is euhedral and kinked  
295 crystals are common. Biotite does not exhibit observable compositional zoning and resorption  
296 features in biotite are rare. Biotite-hosted inclusions of zircon, monazite, magnetite, and feldspar  
297 are common in both samples, and melt inclusions are rare. Biotite in TT7 contains ubiquitous  
298 inclusions of columnar apatite crystals, which are more common than the free apatite phenocrysts.  
299 Apatite crystals are typically <100  $\mu\text{m}$  long, euhedral, compositionally uniform, and lack mineral or  
300 melt inclusions. Sample TT, however, is completely devoid of apatite.

301 *The Mascota augite minette* sample consists of augite (~13 vol%), biotite (~10 vol%), and  
302 apatite (~3 vol%) phenocrysts and microphenocrysts in a very fine-grained matrix of augite, biotite  
303 and Fe-Ti oxides. Biotite is predominantly euhedral with the largest phenocrysts (>1000  $\mu\text{m}$ )  
304 exhibiting sieve textures, resorption features, and normal zoning. Smaller biotite crystals (<100  $\mu\text{m}$ )  
305 are uniform and euhedral. Compared to the other analysed biotite populations, Mascota biotite  
306 contains much fewer inclusions of apatite and other minerals. Apatite is represented by euhedral,  
307 columnar to tabular, up to 500  $\mu\text{m}$  long crystals lacking any observable zoning and inclusions.  
308 Apatite crystals in contact with biotite are usually not entirely surrounded by biotite.

309 *The Umiakovik biotite-hornblende granite* sample consists of alkali feldspar (43 vol.%), quartz  
310 (25 vol.%), plagioclase (20 vol.%), biotite (7 vol.%), hornblende (5 vol.%) and trace amounts of  
311 apatite, zircon, ilmenite, and fluorite (Emslie & Loveridge, 1992). Biotite is dark brown, often bent,  
312 subhedral, up to 1-2 mm large crystals without noticeable zoning in reflected light or SEM. Biotite

313 occasionally contains up to 20 microns sized apatite and zircon inclusions. Apatite crystals are  
314 typically up to 400 microns in size, are euhedral with a prismatic habit, and pale green to  
315 transparent in color. Backscatter electron imaging reveals that approximately 30% of apatite  
316 crystals exhibit a distinct darker, rounded core with >20 micron thick, bright rim. Inclusions in  
317 apatite are rare, usually comprising micron-sized zircons.

### 318 **3.2. Major element compositions of the glasses**

319 The analysed suite of matrix glasses represents silica-rich (71-75 wt% SiO<sub>2</sub>), moderately to  
320 strongly peraluminous (A/CNK=1.0-1.4), K- (4.9-5.7 wt% K<sub>2</sub>O) and Na-rich (2.4-3.0 wt% Na<sub>2</sub>O),  
321 rhyolitic melt compositions, poor in MgO, FeO, CaO, and TiO<sub>2</sub>. The glass compositions imply a highly  
322 polymerized melt structure, with the ratio of non-bridging oxygens to tetrahedrally coordinated  
323 cations (NBO/T; Virgo et al., 1980) of 0.04-0.12 and optical basicity ( $\Lambda$ ; Ottonello et al., 2001) of  
324 0.504-0.505. The electron microprobe data totals are typically 95-97 wt%, which suggests the  
325 presence of dissolved H<sub>2</sub>O. Among other volatiles, F and SO<sub>3</sub> were below detection limits (0.2 and  
326 0.1 wt% respectively), whereas Cl contents vary between 0.03 wt% (Macusani subvolcanics) and  
327 0.12 wt% (FCT) with intermediate values of 0.08-0.09 wt% in the Tuk-Tuk samples. Within this  
328 rather uniformly rhyolitic sample suite, the Macusani subvolcanics stand out as the most  
329 peraluminous and least alkaline (Figure 2), thus overlapping with the genetically related effusive  
330 Picotani and Quenamari samples reported by Pichavant et al. (2024). Glass from the Fish Canyon  
331 tuff represents the most potassic and silicic composition, and the Tuk-Tuk tuffs are the most sodic  
332 and calcic in the sample group (Figure 2).

### 333 **3.3. Major element composition of mineral phases**

334 *Biotite* compositional diversity is reflected by values of iron number (Fe#; Fe<sup>2+</sup>/[Fe<sup>2+</sup>+Mg];  
335 molar basis), which describes the solid solution between phlogopite and annite (Figure 3). The  
336 variation in Fe# is greater between groups than within most groups, thus resulting in discrete Fe#  
337 ranges for MM (0.15-0.21), FCT (0.38-0.42), TT and TT7 (0.57 – 0.61), MAC160 (0.45-0.52), and UP  
338 (0.83-0.90). The Revancha biotite Fe# range is broader (0.24-0.53), which corresponds to a relatively  
339 higher variability in all other major element abundances. The Na content in Revancha biotites  
340 exhibits a negative covariation with the Fe#, whereas Al, Mn, and Cl are positively correlated, but Ti  
341 and F contents show no covariation. The Ti content in the most Mg-rich Revancha biotites

342 (Fe<sup>#</sup>>0.42) is highly variable (0.2 – 0.7 atoms per formula unit [a.p.f.u.], based on 22 negative  
343 charges) in contrast to the more Fe-rich biotites, which show less variation in Ti (0.3 - 0.4 a.p.f.u.).

344 Across the analyzed rock suites, other major element abundances in biotite overlap, leaving  
345 only few outliers. The strongly peraluminous composition of the Macusani subvolcanics is reflected  
346 in biotite with a slight increase in total Al and tetrahedral Al, the latter corresponding to a decreased  
347 silica content due to the common Al-Si substitution in the tetrahedral site. Based on the MnO  
348 content, the biotite suites can be divided into low-Mn biotite (MAC and MM) and high-Mn (FCT, TT,  
349 UP) biotite (Figure 3c). The Umiakovik biotite, which is annite-rich and generally variable in its major  
350 element content, is particularly low in Na, slightly exceeding the detection limit of 0.02 wt% (Fig.  
351 3d).

352 The major element content of apatite is generally uniform across the suites – Ca contents  
353 typically exceed 9.5 a.p.f.u., which almost entirely fills the 7-fold and 9-fold coordination sites.  
354 Tetrahedral sites are primarily filled with P (5.6-5.8 a.p.f.u.) with a minor Si component (0.1-0.2  
355 a.p.f.u.). The anion site is dominated by F (1-2 a.p.f.u.), leaving <1 a.p.f.u. of OH<sup>-</sup>, and trace amounts  
356 of Cl in a negative correlation with Fe in apatite. Mascota apatite is richer in Si (~0.2 a.p.f.u.)  
357 compared to other suites (~0.1 a.p.f.u.).

### 358 **3.4. Trace element compositions**

359 The trace element content of the analyzed glasses are normalized to the average upper crust  
360 (Rudnick & Gao, 2003) in Figure 5, where elements are grouped according to their chemical  
361 classification as alkalis (Li, Rb, Cs), alkaline earth (Sr, Ba), transition metal (Sc, V, Mn, Co, Ni, Cu, Zn,  
362 Mo), metalloid (Ga, Ge, Cd, In, Sn, Pb, Bi), rare earth elements (La, Ce, Pr, Nd, Sm, Eu, Gd, Tb, Dy, Ho,  
363 Er, Tm, Yb, Lu), and high field strength elements (Zr, Nb, Hf, Ta, W). Within each group the elements  
364 are ordered according to mass number. Relative to crustal abundances, the analyzed glasses are  
365 enriched in most alkalis, high field-strength elements and post-transition metals, but depleted in  
366 alkaline earth elements (except Ba) and transition metals. In their rare-earth element compositions,  
367 the matrix glasses are relatively depleted in intermediate REE (FCT and TT) or heavy REE (MAC) with  
368 a distinct negative Eu anomaly in MAC and TT. In this study, Eu anomaly is defined as  $(Eu/Eu^*_{CN})$ ,  
369 where  $Eu^* = (Sm \times Gd)^{0.5}$  and all element concentrations are normalized to McDonough & Sun (1995)

370 chondritic abundances. Macusani glasses are generally the most enriched in incompatible elements  
371 (with anomalously high Li, Cs, As, In, Sn concentrations in all Macusani glasses, Bi, Pb, Rb, Sb, U, W in  
372 Revancha glasses, and Zn in Cerro Esquinani glasses). The abundance of heterovalent elements in  
373 matrix glasses often strongly vary across the sample suite. Vanadium is relatively depleted in all  
374 glasses with the normalized abundance varying between  $\sim 0.04$  in Fish Canyon tuff to  $\sim 0.008$  in  
375 Revancha glasses. Molybdenum is generally enriched (up to  $\sim 5x$  the upper crustal abundance in Fish  
376 Canyon tuff), however, in Cerro Esquinani glass it is slightly depleted. Arsenic, indium, and tin are  
377 strongly enriched (4-20x) in the Revancha dyke, and are slightly depleted (0.9-0.5x) in Fish Canyon  
378 tuff. Tungsten and uranium are also the most enriched in Revancha glasses ( $\sim 7x$ ) and least enriched  
379 (1-2x) in Tuk-Tuk glasses.

380 The trace element abundances of biotite were found to correlate with their major element  
381 composition. Within the low-Al biotite group (all but MAC biotites), most of the trace elements  
382 correlate with the Fe#: Cs, Ge, Pb, Rb, Sc, Sn, Ta, V are in a positive correlation whereas Ba, Co, Cu,  
383 Eu, Hf, Ni, Sr, and Zr correlate negatively with Fe# (Supplementary Figure S5). The aluminous biotites  
384 of the evolved Macusani suite are enriched in trivalent (In, REE, Sc, As), pentavalent (P, Nb, Ta),  
385 other incompatible elements (Rb, Pb, Ge, Bi) and V relative to the less aluminous biotites.

386 The strontium content of apatite correlates with the bulk rock silica content in a trend (in  
387 order of increasing Sr) of UP-MAC137-MAC2-TT7-MAC160-FCT-MM. Within this series, Ba, V, Zn, Zr  
388 increase and REE+Y decrease with increasing Sr. MAC and MM apatite populations record the  
389 broadest Sr ranges (554-179  $\mu\text{g/g}$  and 7875-5365  $\mu\text{g/g}$ , respectively) and reveal compositional  
390 trends: in MM, Ba, REE, Mn, Ta, Th, Ti, V are positively correlated with Sr, whereas in MAC, Ba,  
391 LREE, Th, V, Zr are positively correlated and HREE, Mn are negatively correlated with Sr. The  
392 variation of trace elements in Macusani apatites is similar to that of other apatites. Apatite from the  
393 Umiakovik pluton show the largest variability in compatible trace elements (REE, Y, U, Th) without  
394 any correlation to Sr. Instead, the silica content is in a positive correlation with trivalent (Ga, As,  
395 REE+Y), tetravalent (Ge, Zr, Hf, Th), and other highly charged ions (Ta, W, U) and Rb, without  
396 correlation to Mn, Fe, and Sr. The magnitude of the Eu anomaly in UP apatites strongly correlates  
397 with increasing Si content.

### 398 **3.5. Apatite and biotite chemistry as tracers of evolution of Macusani subvolcanics**

399           The measured biotite and apatite compositions in the Ravencha dyke samples (MAC2,  
400 MAC137) from the Macusani subvolcanics show a high degree of variability in their major (Fig. 3a-d)  
401 and trace element abundances (Supplementary Figure S4-5), which often do not follow the  
402 expectations for a continuous liquid line of descent (e.g. Fe# and Al<sup>IV</sup> in biotite, total REE content in  
403 apatite, F/Cl in either mineral). This compositional heterogeneity has been attributed to a thermal  
404 pulse and volatile (H<sub>2</sub>O, Cl, F) influx due to mafic magma underplating (Sandeman & Clark, 2004). To  
405 extract natural partition coefficients, which represent natural equilibrium mineral and glass matrix  
406 compositions, therefore requires identification of co-crystallizing phase assemblages. Based on  
407 biotite Fe#, F/Cl, Na, and Rb/K (Fig. 3d-g), two distinct biotite generations can be distinguished in  
408 these samples: 1) more primitive, magnesian (Fe# <0.41), F-rich (F/Cl >30), and Rb-poor (Rb/K  
409 <0.008) and 2) more evolved, ferrous (Fe# >0.46), Cl-rich (F/Cl <15), and Rb-rich (Rb/K >0.010). Here  
410 we consider the more evolved second generation biotite as in equilibrium with the surrounding  
411 glass, which is supported by biotite-glass Fe-Mg exchange and interelement partitioning systematics  
412 consistent with previous experimental studies (see below). In contrast to the Ravencha dyke,  
413 sample MAC160 from the Cerro Esquinani stock yielded biotite with a more narrow compositional  
414 range, which is overall similar to the more evolved Ravencha dyke group, but the latter with lower  
415 Rb/K values. Biotite in MAC160 is compositionally uniform and considered to have formed in a  
416 single crystallization event.

417           In Macusani samples, two apatite generations can be distinguished based on Sr and  
418 chondrite-normalized La/Sm, (La/Sm)<sub>CN</sub>: one with low Sr (170-400 µg/g) and low (La/Sm)<sub>CN</sub> (0.6-1.2)  
419 and the other with high Sr (450-560 µg/g) and high (La/Sm)<sub>CN</sub> (1.3-2.2) (Supplementary Figure 9).  
420 Both compositional parameters can be associated with a control by plagioclase. As LREE are more  
421 compatible in plagioclase than HREE (Bindeman & Davis, 2000; Pichavant et al., 2024), co-  
422 precipitation with plagioclase diminishes the (La/Sm)<sub>CN</sub> ratio. As well, a decrease in Sr content in  
423 apatite is known to reflect fractionation of a Ca-rich phase, such as plagioclase (e.g., Belousova et  
424 al., 2001). For the Ravencha dyke, a proposed thermal event has destabilized plagioclase, as  
425 evidenced by dissolution features (Sandeman & Clark, 2004), which in turn would liberate Sr to the  
426 melt. Due to the absence of other abundant and stable Ca-bearing phases in the Macusani

427 subvolcanics, Sr is expected to accumulate in the melt and result in progressively increasing Sr  
 428 content in apatite. Thus, the earlier apatite compositions, which crystallized together with  
 429 plagioclase prior to the thermal event, are expected to have relatively lower Sr and (La/Sm)<sub>CN</sub>  
 430 values, whereas the post-thermal apatite is expected to record an increase in both these  
 431 parameters. Therefore, apatite with (La/Sm)<sub>CN</sub>>1.2 and Sr>400 µg/g are accepted as the latest  
 432 generation of apatite in Macusani subvolcanics and in equilibrium with the host glass.

### 433 3.6. Trace element mineral/melt partition coefficients

434 Partition coefficients ( $D_i^{A/B}$ ) in this study are defined as  $C_i^A/C_i^B$ , where C are element (i)  
 435 concentrations (µg/g weight basis) in phase A ( $C_i^A$ ) and phase B ( $C_i^B$ ). The associated uncertainty on  
 436 partition coefficients is calculated from:

$$437 \quad \sigma = D_i^{A/B} \sqrt{\left(\frac{\Delta C_i^A}{C_i^A}\right)^2 + \left(\frac{\Delta C_i^B}{C_i^B}\right)^2} \quad (1)$$

438 , in which  $\sigma$  is the uncertainty of  $D_i^{A/B}$ ,  $\Delta C_i^A$  and  $\Delta C_i^B$  are the standard deviations of the  
 439 measurements of the element i in phases A and B, respectively. A summary of the mineral/melt  
 440 partition coefficients for all elements that were above the limit of detection is provided in Tables 3  
 441 and 4 and plotted in Figure 6.

442 *Apatite.* Values of  $D^{ap/gl}$  are summarized in Figure 6b, which includes comparison to the results of  
 443 experimental studies on basaltic-andesitic systems at 1.0 GPa and 1250 °C (Prowatke & Klemme,  
 444 2006), basanitic-granitic systems at 950-1120 °C, 0.75-2.0 GPa (Watson & Green, 1981), basaltic  
 445 system at 1050 – 1100 °C, 1.0 GPa (Ji & Dygert, 2024) and a study of a natural phonolite system at  
 446 950±25 °C and 0.2 GPa (Li et al., 2023). Also considered were the experiments of Stokes et al.  
 447 (2019), carried out in compositions ranging from trachyte to basalt at 1250-1400°C and 1.0 GPa.  
 448 Among the measured trace elements, the REE are the most compatible in apatite, with the lowest  
 449  $D^{ap/gl}$  values for alkalis (Rb, Cs). The compatibility of the REE is a downward concave function of  
 450 atomic number with the highest D values recorded for Gd and the lowest for La and Lu. Overall, the  
 451 natural rare earth element D values are up to 10x higher than the range reported in experimental  
 452 studies, the origin of which is discussed in the section below on mineral-melt equilibrium. Other  
 453 compatible trace elements include Ge and Mn with D values in all suites of ~20 and 10, respectively.

454  $D_{\text{Ge}}^{\text{ap/gl}}$  has not been previously reported but likely follows Si substituting for  $(\text{PO}_4)^{3-}$  as the oxyanion  
455  $(\text{GeO}_4)^{4-}$  (Pan & Fleet, 2002). Values of  $D_{\text{Mn}}^{\text{ap/gl}}$  are consistent with experimental determinations  
456 involving highly polymerized ( $\text{NBO}/\text{T} = 0.03 - 0.10$ ) and peraluminous melts ( $\text{ASI} = 1.0-1.3$ ) reported  
457 by Stokes et al. (2019). Natural partition coefficients for Sr, Th, and U correspond to the upper limits  
458 of the range recorded in the experimental studies of Ji & Dygert (2024). Values of  $D_{\text{V}}^{\text{ap/gl}}$  from the  
459 natural samples range between 0.5 and 5, generally increasing with the  $f\text{O}_2$  estimated for each suite,  
460 with a further discussion of this provided below; we are unaware of any previous experimental  
461 measurements of  $D_{\text{V}}^{\text{ap/gl}}$  for comparison. Transition metals are more incompatible with increasing  
462 atomic number, ranging from  $D_{\text{Cu}}^{\text{ap/gl}} \sim 1$  to  $D_{\text{Zn}}^{\text{ap/gl}} \sim 0.1$ , with the latter values for  $D_{\text{Zn}}^{\text{ap/gl}}$  consistent  
463 with the range reported by Ji & Dygert (2024). Apatite-melt partition coefficients for Pb coincide  
464 with the lower limit of the experimentally determined range reported by Prowatke & Klemme  
465 (2006) and Li et al. (2023). Like V,  $D^{\text{ap/gl}}$  for Sn and Bi have not been reported from experiments, with  
466 Bi showing weak incompatibility ( $D^{\text{ap/gl}}$  of  $\sim 0.3$  to 1), similarly for Sn, although the D range is larger  
467 (0.05 to 1) and reflects some  $f\text{O}_2$  dependence (see below). Elements from the LIL and HFSE groups  
468 are the least compatible in apatite, with D values generally below 0.1, overlapping with the range of  
469 determinations from Prowatke and Klemme (2006), although the corresponding uncertainties are  
470 large due to the low abundance of these elements in the natural samples.

471 *Biotite.* Values of  $D^{\text{bt/gl}}$  are assembled in Figure 6b and compared to the experimental  
472 determinations of Icenhower and London (1995), Stepanov and Hermann (2013), Pichavant et al.,  
473 (2016), Gion et al. (2018), Were and Keppler (2021), Wei et al. (2024) and determinations from  
474 glassy volcanic rock suites (El Hoyazo dacite, SE Spain; Acosta-Vigil et al., 2010) including previous  
475 measurements for the FCT (Bachmann et al., 2005) and the effusive Macusani suites (Pichavant et  
476 al., 2024) related to the Macusani subvolcanics analyzed in this study. Previous biotite-melt  
477 partitioning experiments were done on rhyolitic compositions over the temperature range of 600-  
478 1000 °C, pressures from 0.1 to 2.5 GPa and most  $f\text{O}_2$  near FMQ+1, but Wei et al. (2024) investigated  
479 FMQ-1 to FMQ+8.

480 Of the elements considered, the transition metals are generally the most compatible in  
481 biotite, with the largest  $D^{\text{bt/gl}}$  for V, Co, and Ni ( $>50$ ), and other transition metals (Sc, Mn, Zn, Cu)  
482 being moderately compatible ( $D^{\text{bt/gl}}$  1-10). Alkalis, alkali earth metals, and metalloids are moderately

483 compatible ( $D^{bt/gl}$  1-10; Ba, Rb, Ga, In) to moderately incompatible (Li, Cs, Sr, Ge, Pb, Bi with  $D^{bt/gl}$   
484 0.1-1). High field strength elements (Zr, Hf, W, Mo) are strongly incompatible ( $D^{bt/gl} = 0.5-0.01$ ).  
485  $D_{Nb}^{bt/gl}$  (2-10) exceeds the  $D_{Ta}^{bt/gl}$  (0.6-3) in all cases. Rare earth elements are the most incompatible  
486 group with  $D_{REE+Y}^{bt/gl} < 0.2$ , except Eu with  $D^{bt/gl}$  of 0.1 to 1.0. The natural  $D^{bt/gl}$  values determined in  
487 this study, overlap with the experimentally determined range of partitioning coefficients. The values  
488  $D^{bt/gl}$  for Co, Ni, Zn, Mn, Nb, Ta, Ba, Rb, Cs, Mo, Eu, Gd, Zr overlap with the experimental  
489 determinations by Were & Keppler (2021). Results from Gion et al. (2018) showed that  $D^{bt/gl}$  for In  
490 increases with biotite Fe#, proportion of IV-fold Al and Ti content. Our natural determinations are  
491 consistent with the experimental values by Gion et al. (2018) despite the natural biotites having a  
492 higher annite component than any of the synthetic biotites reported by Gion et al (2018). For Y, Sc,  
493 Ge, and Hf, we are not aware of any experimentally established  $D^{bt/gl}$ , however, our findings agree  
494 with the other natural determinations. Partition coefficient values for Sr (0.1-0.4) are within the  
495 range found by Icenhower & London (1995), below the  $D_{Sr}^{bt/gl}$  value (0.57) reported by Were &  
496 Keppler (2021) in a single, more calcic melt (1.87 wt% CaO, compared to <1.1 wt% in our samples  
497 and Icenhower & London experiments) at 800 °C. Our determined range of  $D_{Li}^{bt/gl}$  of 0.1-0.7 overlaps  
498 with results from experiments involving peraluminous compositions, with values 0.4 to 1 reported  
499 by Pichavant et al. (2016), and 0.8-1.7 determined by Icenhower & London (1995). Both sets of  
500 experiments indicate that  $D_{Li}^{bt/gl}$  decreases with melt ASI and increases with biotite  $Al^{IV}$  content. In  
501 that context, the similarity of our results with those of Pichavant et al. (2016) is consistent with  
502 both melt composition (72.6-75.7 wt%  $SiO_2$ ) and biotite  $Al^{IV}$  content (2.33-2.56 a.p.f.u.) similar to the  
503 samples investigated here (72.3-74.8 wt%  $SiO_2$  in glass, 2.28-2.61  $Al^{IV}$  a.p.f.u. in biotite).

504 Partitioning systematics for V, W, Eu, Sn, and Mo indicate a redox-sensitivity (Fig. 10).  
505 Vanadium  $D^{bt/gl}$  decreases from 586 to 56 with increasing  $fO_2$  with the range corresponding to the  
506 results from El Hoyazo dacite (335-15) by Acosta-Vigil et al. (2012). Experimental determinations of  
507  $D_V^{bt/gl}$  by Were & Keppler (2021) suggest a more moderate compatibility (23-47) in biotite, however,  
508 their measurements involved Ti-poor biotites (<1.6 wt%  $TiO_2$ ) in comparison to compositions from  
509 the natural samples (3.9-4.5 wt%  $TiO_2$ ). As discussed in Section 4.2, increasing the biotite  $TiO_2$   
510 content is expected to increase  $D_V^{bt/gl}$ . Values of  $D^{bt/gl}$  for W decrease from 0.13 to 0.02 with  
511 increasing oxygen fugacity. These values are below the determinations reported by Pichavant et al.

512 (2024) for the Macusani volcanics ( $0.38 \pm 0.06$ ) and from the experiments of Were & Keppler (2021)  
513 ( $1.2 \pm 0.8$ ), but agrees with the findings of Dailey et al. (2018) involving the Spor Mountain topaz  
514 rhyolite ( $0.06 \pm 0.06$ ). As tungsten is predominantly hexavalent even at the most reducing terrestrial  
515  $fO_2$  conditions (O'Neill et al., 2008), this element is expected to be incompatible with most rock-  
516 forming minerals (Arevalo & McDonough, 2008; Fonseca et al., 2014), which is inconsistent with the  
517 relatively large partition coefficients reported by Were & Keppler (2021). The value of  $D^{bt/gl}$  for Sn  
518 varies between  $\sim 0.1$  and 1, with an increase in value with  $fO_2$  of the sample suite. This result is  
519 consistent with the experimental measurements of  $D_{Sn}^{bt/gl}$  reported by Wei et al. (2024) in which  
520 values increase from  $\sim 0.02$  at FMQ-1 to  $\sim 3$  at FMQ+8. Values of  $D_{Mo}^{bt/gl}$  decrease with increasing  $fO_2$   
521 – from  $1.6 \pm 1.2$  in MAC samples, to  $0.7 \pm 0.3$  in Tuk-Tuk tuff, and  $0.09 \pm 0.03$  in FCT. Determinations of  
522  $D_{Mo}^{bt/gl}$  by Dailey et al. (2018) in the reduced Spor Mountain rhyolites (1.1-1.3) overlap with our  
523 measurements in the MAC samples, whereas Were & Keppler (2021) report values of  $0.29 \pm 0.15$ ,  
524 close to the similarly oxidized Tuk-Tuk tuff.

525 The natural biotite-melt partition coefficients presented here are also generally consistent  
526 with values reported for mineral/glass pairs from similar samples. Bachmann et al. (2005) measured  
527 a number of the same trace elements in biotite and glass (as well as other phenocryst phases) from  
528 samples of the FCT, yielding similar values to our empirical determinations (Supplementary Figure  
529 S8). Our results from the MAC subvolcanic samples are in general agreement with the results for  
530 the Macusani tuffs reported by Pichavant et al. (2024) (Supplementary Figure S7), except the values  
531 for  $D_{Li}^{bt/gl}$  of 0.12-0.57 determined in this study are much lower than the  $D_{Li}^{bt/gl}$  of  $\sim 3.7$  reported for  
532 the Macusani tuffs. Values of  $D_{Li}$  for the Macusani subvolcanics are consistent with results from  
533 other suites measured in this study along with experimental determinations of Pichavant et al.  
534 (2016) and Acosta-Vigil et al. (2012) involving melts of dacitic composition. As an explanation for the  
535 higher values of  $D_{Li}^{bt/gl}$  measured by Pichavant et al. (2024), those authors have suggested that a  
536 secondary Li enrichment or redistribution in the Macusani tuffs could have altered the Li content in  
537 phenocrysts and matrix. Furthermore, we note that the composition of biotite from the samples for  
538 which  $D^{bt/gl}$  were measured by Pichavant et al (2024) differ somewhat from those measured here, in  
539 that the Macusani tuffs are generally more compositionally evolved, with higher Fe# ( $\sim 0.65 - 0.80$ ),  
540  $Al_2O_3$  (19.0-21.4 wt.%), and Rb content (912-2242  $\mu g/g$ ) compared to our samples (Fe# < 0.54,

541  $\text{Al}_2\text{O}_3 < 19.7$  wt.%,  $\text{Rb} < 1150$   $\mu\text{g/g}$ ). As well, the partitioning of Li into biotite may be enhanced by  
542 decreasing T as documented by Icenhower and London (1995). It is therefore possible that the  
543 overall more evolved nature of the Macusani tuff biotites could suggest a lower crystallization  
544 temperature, accounting for the higher value of  $D_{\text{Li}}^{\text{bt/gl}}$ .

### 545 **3.7. Oxybarometry of Macusani subvolcanics and other sampled suites**

546 The oxygen fugacity of the Macusani igneous suites has been qualitatively assessed by  
547 Pichavant et al. (1988a) and Sandeman & Clark (2003). Both studies suggest a low  $f\text{O}_2$  (below FMQ)  
548 thus identifying Macusani magmas as valuable reduced endmembers of silicic melt suite. However,  
549 to assess the redox controls on heterovalent element partitioning, a quantitative  $f\text{O}_2$  estimate of the  
550 Macusani magmas is essential. For this purpose, we use the Macusani zircon REE and other trace  
551 element concentrations in zircon Ce-U-Ti oxybarometer by Loucks et al. (2020) to determine the  
552 oxygen fugacity of the Revancha dyke (measured in sample MAC137) and the Cerro Esquinani stock  
553 (MAC 160) samples.

554 As described above, zircon occurs in both sample suites as small ( $< 50$   $\mu\text{m}$ ), euhedral crystals,  
555 exhibiting well-developed, concentric growth zoning, with rare textural evidence of xenocrystic  
556 cores. In total, 24 zircon analyses were obtained from these samples. Analysis of the zircons was  
557 particularly challenging because of their small size, and therefore susceptibility to contamination by  
558 the laser sampling inclusions of other minerals, or surrounding glass. To minimize the non-zircon  
559 contribution, the time-resolved spectrum for each zircon analysis was carefully reviewed, and the  
560 REE and zircon-incompatible element (Na, Al) patterns were used to filter those subject to  
561 contamination within the ablated volume. Following this, 11 measurements from the Revancha  
562 dyke and 4 measurements from the Cerro Esquinani stock were accepted as representative of  
563 uncontaminated zircon trace element compositions.

564 The oxybarometer of Loucks et al. (2020) uses the redox-sensitivity of zircon Ce/U ratio, which  
565 is corrected for magmatic differentiation using zircon Ti/U value. The measured trace element  
566 concentration of zircon, and resulting oxygen fugacities are provided in the Supplementary Table S1.  
567 The oxybarometry results suggest similar, reduced  $f\text{O}_2$  values for both Macusani subvolcanic units:  
568 FMQ- $3.6 \pm 0.9$  for the Revancha dyke and FMQ- $2.9 \pm 0.6$  for the Cerro Esquinani stock. This overlaps

569 with results of a different calibration of zircon/melt Ce partitioning oxybarometer by Smythe &  
570 Brenan (2016), which suggests FMQ-2.9±0.9 and FMQ-1.9±1.0 for the same suites, respectively. The  
571 results are consistent with the absence of magnetite and the very low Fe<sub>2</sub>O<sub>3</sub> content (<1 wt.%) in  
572 ilmenite from the Revancha dyke and Macusani tuffs (Pichavant et al., 1988b; Sandeman & Clark,  
573 2003).

574 Igneous  $fO_2$  of the other sampled suites have been established using Fe-Ti oxides (Chesner,  
575 2012; Johnson & Rutherford, 1989), melt Fe<sup>3+</sup>/Fe<sup>2+</sup> (Carmichael et al., 1996), and Ce zircon/melt  
576 partitioning (Smythe & Brenan, 2016). To minimize the potential biases between  $fO_2$  measurements  
577 based on different equilibria, we have applied zircon Ce-U-Ti oxybarometer to the sampled suites  
578 where possible. As argued by Loucks et al. (2020), their  $fO_2$  estimate for FCT and TT are consistent  
579 with Fe-Ti oxybarometry, and, in case of TT, also with the Ce partitioning oxybarometer. In Mascota  
580 minettes, application of zircon-based oxybarometry is precluded by absence of the mineral, thus we  
581 retain the Carmichael et al. (1996)  $fO_2$  estimate. For the Umiakovik pluton, the zircon-based  
582 oxybarometers produce contradicting results for the same zircon compositions: FMQ-2.4±0.7  
583 (Smythe & Brenan, 2016) and FMQ-0.8±0.7 by using Smythe & Brenan data in Loucks et al.  
584 oxybarometer. Here, Smythe and Brenan results are more consistent with other redox evidence in  
585 the Umiakovik pluton: low Fe<sub>2</sub>O<sub>3</sub> content in ilmenite and low ferric/ferrous iron ratio in biotite  
586 (Emslie & Stirling, 1993). We suspect that the higher  $fO_2$  values generated by Loucks oxybarometer  
587 are a consequence of zircon recrystallization, evidenced by zircon textures reported by Smythe &  
588 Brenan (2016). Recrystallization can produce uranium-poor zircon compositions (Pidgeon, 1992),  
589 which would strongly affect the results of Ce-U-Ti oxybarometer while having a lesser impact on Ce  
590 partitioning. Thus we deem the results of Ce partitioning oxybarometry to be representative of the  
591 igneous  $fO_2$  of the Umiakovik pluton.

## 592 **4. Discussion**

### 593 **4.1. Evidence for crystal-melt equilibrium**

#### 594 *Textural evidence*

595 Biotite crystals have been observed in all of the analyzed samples, occurring as ubiquitous,  
596 lamellar phenocrysts and microphenocrysts. Phenocrysts are chemically uniform and euhedral in  
597 FCT and TT samples, whereas the larger biotites from both MAC and MM samples frequently exhibit

598 resorption features and compositional zoning observable in both optical and BSE imaging. Biotite  
599 microphenocrysts, however, are commonly euhedral and unzoned, with the exception of the  
600 Revancha dyke, where reversly zoned biotite is present (Fig. 1c).

601 Apatite in the sample suite is present in trace amounts as microphenocrysts and biotite-  
602 hosted inclusions. Apatite microphenocrysts are commonly euhedral, and tabular to equant. In most  
603 samples apatite is chemically uniform, with rare cases of concentric growth zoning or inherited,  
604 partially resorbed cores, as observable in BSE imaging (Fig. 1e). Apatites from the UP, however,  
605 commonly display bright, up to 20-30  $\mu\text{m}$  thick rims in BSE images, suggesting at least two stages of  
606 apatite growth. In most samples, apatite phenocrysts are free from inclusions, with the exception of  
607 Revancha dyke samples, where apatite phenocrysts (ocasionally exceeding 1000  $\mu\text{m}$  size) contain a  
608 multitude of mineral (monazite, zircon) and melt inclusions.

609 As natural intra-crystal and intercrystal compositional variation is present in at least some of  
610 the samples, further verification of mineral-melt equilibria must be provided, as described in the  
611 sections that follow.

#### 612 *Mineral /melt equilibria*

613 Comparison to experimentally established major element exchange coefficients ( $K_d$ ) and  
614 trace element D values for mineral/melt partitioning enables evaluation of the chemical equilibrium  
615 between biotite, apatite, and glass from the natural samples. Biotite-glass major element  
616 equilibrium was assessed using Fe-Mg exchange partitioning, expressed as:

$$617 \quad K_D^{Fe-Mg} = \left( \frac{X_{Fe}^{bt}}{X_{Fe}^{gl}} \right) \left( \frac{X_{Mg}^{bt}}{X_{Mg}^{gl}} \right) \quad (2)$$

618 where X are mole fractions of elements (Fe, Mg) in biotite (bt) and glass (gl). Figure 7a  
619 provides a comparison of  $K_D^{Fe-Mg}$  values determined in the natural samples to the results of the  
620 experimental studies involving water-saturated granitic melts (Were & Keppler, 2021; Icenhower &  
621 London, 1997). Results of the experimental studies suggest an overlapping range of  $K_D^{Fe-Mg}$  from  
622 0.060 to  $\sim$ 0.177 that would be characteristic of biotite and granitic melts in equilibrium. The range  
623 of  $K_D^{Fe-Mg}$  from the natural samples is 0.06 to 0.277, which is similar to the experimentally  
624 determined values, consistent with Fe-Mg exchange equilibrium.

625 Experimentally established values of  $D_{Sr}^{ap/gl}$  (Prowatke & Klemme, 2006; Watson & Green,  
 626 1981) were used to assess apatite-melt equilibrium. Strontium was selected for verification of  
 627 equilibrium due to its measureable abundance in the analyzed glasses and high compatibility in  
 628 apatite. Most of the  $D_{Sr}^{ap/gl}$  values obtained in this study are similar to or greater than the highest  
 629 values reported from experiments (~5; Prowatke and Klemme, 2006). Significantly, Prowatke and  
 630 Klemme (2006) found a strong negative correlation between the melt CaO content and  $D_{Sr}^{ap/gl}$ , with  
 631 the highest partition coefficients recorded for the most CaO poor melts (i.e., ~5 wt% CaO; Figure 7b).  
 632 A similar, but less pronounced trend in Sr partitioning was observed by Watson and Green (1981) in  
 633 felsic compositions at lower temperature, which suggests a more complex compositional and/or  
 634 temperature control of  $D_{Sr}$ . Our results further support this suggestion, as they do not overlap with  
 635 the Prowatke and Klemme (2006) and Watson and Green (1981) results, but instead plot at the low  
 636 CaO (i.e., <1 wt%) extension of the experimentally-determined  $D_{Sr}$  trends (Figure 7).

637 Another test for mineral-melt equilibrium is to compare the measured partition coefficients  
 638 for isovalent elements with predictions from the lattice strain model formulated by Blundy and  
 639 Wood (1994). The model is used to model mineral/melt partition coefficient coefficient of trace  
 640 element  $i$  ( $D_i$ ) at specific P-T-X conditions as a function of “strain-compensated partition coefficient”  
 641 [ $D_0(P,T,X)$ ], temperature (T), Young’s modulus of the host crystal (E), radii of the trace element  $i$  and  
 642 substituted element ( $r_i$  and  $r_0$ , respectively):

$$643 \quad D_i(P, T, X) = D_0(P, T, X) \cdot \exp \left[ \frac{-4\pi E N_A \left[ \frac{r_0}{2}(r_i - r_0)^2 + \frac{1}{3}(r_i - r_0)^3 \right]}{RT} \right] \quad (3)$$

644 where  $N_A$  is Avogadro number and R is the gas constant. Assuming crystal-melt equilibrium  
 645 at constant P,T and X,  $D_i$  values for a series of isovalent trace elements is a concave function of  $r_i$   
 646 with the maxima at strain-free substitution ( $r_i=r_0$ ) and decreasing  $D_i$  as the mismatch between  $r_i$  and  
 647  $r_0$  increases. Thus, plots of  $D_i$  versus  $r_i$ , termed Onuma diagrams (Onuma et al., 1968), result in  
 648 concave functions with maxima at  $D_0$  and  $r_0$ , and the width of the parabola decreasing with  
 649 increasing E. Blundy-Wood lattice strain model has been confirmed in numerous experiments and  
 650 natural studies (e.g., Beattie, 1994; Lee et al., 2007; Shimizu et al., 2017; van Westrenen & Draper,  
 651 2007; Zajacz & Halter, 2007) including several focused on biotite (LaTourrette et al., 1995; Schmidt

652 et al., 1999; Were & Keppler, 2021) and apatite (Klemme & Dalpé, 2003; W. Li et al., 2023; Prowatke  
653 & Klemme, 2006). Thus, results for mineral-melt equilibrium are tested by adherence to the  
654 expectations from the successful Blundy-Wood lattice strain model.

655 In applying the Blundy-Wood model, temperatures of crystal-melt equilibrium were  
656 estimated from the Ti-in-biotite calibration of Henry et al. (2005) due to the peraluminous and  
657 titania-rich sample compositions, which are saturated with ilmenite or other Fe-Ti oxide phase.  
658 Values of  $D_0$ ,  $r_0$ , and  $E$  were determined using least squares regression for each isovalent series of  
659 trace element  $D_i$  values (Supplementary Table ST7). Values of  $r_i$  for a specific trace element will  
660 depend on both ionic charge and coordination (Shannon, 1976), and were therefore selected with  
661 guidance from previous partitioning and mineral structural studies (Padilla & Gualda, 2016; Pan &  
662 Fleet, 2002; Pichavant et al., 2024; Were & Keppler, 2021) and size-charge considerations.  
663 Partitioning arrays are shown in Figures 8 and 9 for apatite and biotite, respectively.

664 The apatite structure contains three types of cation sites: VII- and IX-fold coordination  
665 (generally occupied by Ca with  $r_0$  being 0.106 in VII-fold and 0.118 in IX-fold coordination) along with  
666 tetrahedrally coordinated site typically containing phosphorous with  $IR=0.017$  nm (Pan & Fleet,  
667 2002). The larger ions ( $IR$  exceeding 0.07 nm in VIII-fold coordination) are assumed to solely enter  
668 the VII- and IX-fold sites, with radii corresponding to an intermediate VIII-fold coordination.

669 Divalent and trivalent cations are the most compatible with the VII- and IX-fold coordinated  
670 sites. Both of the isovalent arrays adhere to concave  $D_i$ - $r_i$  functions (Fig. 8) with similar  $r_0$  values  
671 (0.111-0.113 nm for divalent and 0.106-0.108 nm for trivalent ions) with the trivalent array having a  
672 higher  $E$  (270-349 MPa) and  $D_0$  (103 – 177) than the divalent series ( $E=250$ -303 MPa,  $D_0=64$ -129).  
673 The values of  $r_0$  of the trivalent series (0.106-0.108 nm) are similar to the  $IR$  of  $Ca^{VII}$  (0.106 nm; Pan  
674 & Fleet, 2002), which explains the REE preference for entering in the smaller  $Ca^{VII}$  site, observed in  
675 earlier studies (Pan & Fleet, 2002). The larger  $r_0$  values of the divalent array (0.111-0.113 nm) are  
676 between the  $IR$  of the  $Ca^{VII}$  and  $Ca^{IX}$  thus suggesting an equal divalent ion distribution between the  
677  $Ca^{VII}$  and  $Ca^{IX}$  sites. Several of the less compatible divalent elements (Zn, Mg, Pb, Ba), however,  
678 deviate from fitted  $D_i$ - $r_i$  functions (Fig. 8). Each of these elements show a preference for one of the  
679 Ca sites: Pb, Ba and Zn preferentially enter the  $Ca^{VII}$  site, but Mg the  $Ca^{IX}$  site (Elliott, 1994; Pan &

680 Fleet, 2002). Furthermore, the partitioning of Mg in apatite is enhanced by high melt polymerization  
681 with this effect amplified at low temperature (Zhan et al., 2022). Experimentally determined  $D_{Mg}$  in  
682 low-P-T siliceous peraluminous systems exceed unity (Trend 2 - Zhan et al., 2022), which coincides  
683 with the elevated  $D_{Mg}$  values (up to 6.0) in the Macusani samples.

684 Similar to the trivalent series, the tetravalent series (Hf-Zr-Th) with  $r_0=0.106-0.109$  indicate  
685 affinity for the  $Ca^{VII}$  site as previously described by Luo et al. (2009). Related to the tetravalent  
686 series, the ratio of  $D_U/D_{Th}$  is below 1 in the reduced Macusani rocks, equals 1 in Tuk-Tuk tuff, and  
687 exceeds 1 in the oxidized Fish Canyon tuff. While thorium exists exclusively in the tetravalent state,  
688 uranium in silicate melts can be present in valence states (Schreiber, 1983) of  $U^{4+}$  (IR=0.100 nm in  
689 VIII-fold coordination),  $U^{5+}$  (IR=0.084 nm in VII-fold coordination),  $U^{6+}$  (IR=0.081 nm in VII-fold  
690 coordination). With a charge and size being the closest to  $Ca^{2+}$  in VII-fold coordination,  $U^{4+}$  is the  
691 most compatible in the apatite structure (Clarke & Altschuler, 1958). Thus,  $D_U/D_{Th}$  is likely to vary as  
692 a function of  $U^{4+}/\Sigma U$  in melt, which is in part controlled by the  $fO_2$ , stabilizing the more compatible  
693  $U^{4+}$  under reduced conditions (Fonseca et al., 2014).

694 Monovalent ions are generally incompatible ( $D_i < 0.1$ ) in the apatite structure. The arrays of  
695 Na-K-Rb reach the maxima at near  $r_{Na}$  ( $r_0=0.115-0.120$ ), which suggests a preference for entering the  
696 larger, IX-fold coordination site.  $D_{Li}$ , however, exceeds the values expected from the monovalent  $r_i$ -  
697  $D_i$  fit. The relatively lower IR of lithium (0.092 nm in VIII-coordination with no data about any higher  
698 coordination) could lead to a preference for a lower coordination.

699 Although the relative apatite-melt partitioning of the trivalent REE + Y is consistent with the  
700 lattice strain model, as mentioned previously, absolute values of partition coefficients for this  
701 element group are up to 10 times higher than those reported in previous experimental studies  
702 (Watson & Green, 1981; Prowatke & Klemme, 2006). Mineral or melt composition effects may  
703 serve as possible explanations, as past work has shown that the  $D_{REE}^{ap/gl}$  increases both with the Si  
704 content in apatite and the degree of melt polymerization, the latter simply expressed as melt  $SiO_2$   
705 content. The Si contents of the apatites measured in this study are comparable to those produced  
706 in past experiments, so that is an unlikely cause. However, the natural glasses are significantly more  
707 evolved ( $SiO_2 = 72-75$  wt.%) than the range from previous experimental studies ( $SiO_2 = 36-70$  wt%).

708 Prowatke & Klemme (2006) combined their data with the results from Watson and Green (1981) to  
709 show that  $D_{Sm}^{ap/gl}$ , a representative REE, increases approximately exponentially with melt SiO<sub>2</sub>  
710 content. This relationship is shown in Figure 7c, along with results from this study, Little Glass  
711 Mountain (LGM) rhyolite (USA) reported by Brophy et al. (2011), and from Erebus (Antarctica),  
712 reported by Li et al. (2023) Values of  $D_{Sm}^{ap/gl}$  determined in this study are similar to those measured  
713 for the LGM sample, which is consistent with overlapping glass SiO<sub>2</sub> concentrations. All datasets  
714 seem to project smoothly from the experimental results, suggesting that the unusually large values  
715 of  $D_{Sm}^{ap/gl}$  (and by extension other REE + Y) measured in this study are the result of melt composition  
716 control.

717 As for biotite, its structure comprises three kinds of cation sites – XII-fold coordinated  
718 (usually hosting LILE, e.g. K), VI-fold coordinated, most commonly hosting di- and trivalent elements  
719 (e.g., Mg, transition metals, REE), and a IV-fold coordinated site, typically occupied by Si or Al  
720 (Bailey, 1984). The Onuma diagram for biotite-melt partitioning (Figure 9) reveals five groups of  
721 concave isovalent element arrays: monovalent elements in XII-fold coordination (comprising Na, K,  
722 Rb, Cs), divalent elements in VI-fold coordination (Mg, Co, Fe, Mn), trivalent elements in VI-fold  
723 coordination Ga, Sc, In, Lu, Yb, Y), trivalent elements in IV-fold coordination (Al, Ga, In), and  
724 tetravalent elements in IV-fold coordination (Si, Ge, Hf, Zr). For the XII-fold coordinated site, the  
725 monovalent element array peaks at  $r_0 = 0.164-0.170$  nm with  $D_0 = 1.6-2.1$ , consistent with K as the  
726 most suitable occupier. Divalent Ba<sup>XII</sup> has an  $IR=0.161$  nm, which results in high  $D_{Ba}^{bt/gl}$  values (2.4-  
727 8.4), however, developing a meaningful Brice fit for divalent elements is precluded by the large  
728 uncertainties of  $D_{Ca}^{bt/gl}$  and the electron configuration of Pb, which leads to formation of partial  
729 covalent bonds, which do not obey the Wood-Blundy  $r_i-D_i$  model (Engel et al., 1975; Were &  
730 Keppler, 2021). The biotite octahedral site is known to accommodate cations of several valence  
731 states (Nickel, 1954). In this study, two isovalent arrays are fitted: divalent elements form the higher  
732 D tier with  $r_0 = 0.065 - 0.070$  nm and  $D_0 = 165-447$ , compared to the trivalent cation array with  
733 overlapping  $r_0 = 0.067-0.072$  and lower  $D_0$  values = 2.7-13.0. The  $r_0$  value of the divalent array  
734 appears to decrease with increasing Al content and the opposite is true for the trivalent array. In the  
735 divalent series, Mg<sup>2+</sup> ( $IR=0.072$  nm in VI-fold coordination) is the closest to  $r_0$  thus it is the most  
736 compatible element. In the trivalent series, the octahedral site  $r_0$  values are similar to the ionic radii

737 of Ga and Sc (0.062 and 0.0745 nm, respectively) and positively correlate with the biotite alumina  
738 content thus implying that the size of the octahedral cation sites for divalent and trivalent elements  
739 is altered by the abundance of Al. Ionic radii of several highly-charged ions are close to the  $r_0$  of the  
740 octahedral site:  $Ti^{4+}$  ( $r_0=0.0605$  nm),  $V^{3+}$  (0.064 nm),  $V^{4+}$  (0.058 nm),  $Nb^{5+}$  and  $Ta^{5+}$  (both 0.064 nm),  
741  $Sn^{4+}$  (0.069 nm), which explains their compatibility in the analyzed biotite suites. Given that the  $D_i-r_i$   
742 curves for the highly charged elements would be much narrower than that of divalent elements  
743 (Blundy & Wood, 1994), even a minor change in the  $r_0$  of the site due change to the crystal  
744 chemistry can strongly alter the  $D_i$  values of the HFSE, therefore biotite  $Al^{VI}$  could be important  
745 when considering and comparing the  $D$  values of other, octahedrally coordinated elements.

746 In general, the natural partitioning measurements are consistent with experimental  
747 measurements, either as overlapping values, or on the extension of trends with other melt  
748 composition parameters (e.g., wt% CaO, wt%  $SiO_2$ ). Onuma diagrams defined for biotite- and  
749 apatite-melt partitioning of similarly-sized isovalent cations display parabolic relations with values of  
750  $r_0$  and  $D_0$  consistent with the major substituent cations for a particular site. Results therefore  
751 suggest that the mineral/melt partitioning of the trace elements measured for the natural samples  
752 broadly adhere to the systematics established by the experimental database, and by extension,  
753 reflect crystal-melt equilibrium.

#### 754 **4.2. Redox control on heterovalent element partitioning**

755 Amongst the group of elements for which natural partition coefficients have been  
756 determined, several are expected to have multiple valence states over the range in  $fO_2$  of terrestrial  
757 magmas. These include V (2+, 3+, 4+, 5+), As (3+, 5+), Eu (2+, 3+), Mo (4+, 6+), Sn (2+, 4+) and W (4+,  
758 6+) (Canil, 1999; Mallman and O'Neill, 2009; Maciag & Brenan, 2020; Drake, 1975; Linnen et al.,  
759 1995; 1996; Holzheid et al., 1975; Fonseca et al., 2014). As shown in Figure 10, all of these elements  
760 show a systematic variation in values of  $D^{mineral/glass}$  with the estimated  $fO_2$  of each magmatic suite,  
761 which here we ascribe to a predominant control of  $fO_2$  on the ionic radius and charge of  
762 progressively changing proportions of cation species.

763 The partitioning of V between biotite and melt is highest (up to 585) in the most reduced  
764 end of the sample suite (Macusani subvolcanics), while the lowest  $D_V^{bt/gl}$  is found in the most

765 oxidized rocks (Fish Canyon tuff). The opposite trend is observed for  $D_{V^{ap/gl}}$ . The difference is further  
766 amplified if apatite/biotite partitioning is considered –  $D_{V^{ap/bt}}$  changes from 0.001 in the reduced  
767 MAC137 to 0.547 in the oxidized Mascota minette. As described in the introduction, the VI-fold  
768 coordination ionic radii of the species  $V^{2+}$ ,  $V^{3+}$ ,  $V^{4+}$ ,  $V^{5+}$  are 0.079, 0.064, 0.058 and 0.054 nm,  
769 respectively, hence the  $V^{2+}$ ,  $V^{3+}$ ,  $V^{4+}$  species are suitable substitutes for  $Fe^{2+}$ ,  $Ga^{3+}$ , and  $Ti^{4+}$ , leading to  
770 their compatibility in biotite at lower  $fO_2$ , but relative exclusion of  $V^{5+}$  at higher  $fO_2$ . Only  $V^{5+}$   
771 exhibits a potential for being compatible in the apatite structure, as the oxyanion  $(VO_4)^{-3}$  can  
772 substitute for  $(PO_4)^{-3}$  (Pan & Fleet, 2002). Apatite VII- and IX-fold coordinated sites (usually occupied  
773 by  $Ca^{2+}$ ), however are too large to accommodate any of the other V species. As the higher charged  
774 V species are stabilized in oxidized melts, the higher abundance of more compatible  $V^{5+}$  is expected  
775 to enhance the overall V compatibility in apatite, which is consistent with the observed increase in  
776  $D_{V^{ap/gl}}$  with  $fO_2$ .

777 In contrast to V, values of  $D_{Sn^{mineral/melt}}$  increase with  $fO_2$  for *both* biotite and apatite, and this  
778 systematic relationship results in essentially constant values of  $D_{Sn^{ap/bt}}$  ( $0.40 \pm 0.24$ ) over the  $fO_2$   
779 range of the sample suites. The change in the biotite- and apatite-melt partition coefficients likely  
780 reflects the difference in compatibility of the  $Sn^{2+}$  and  $Sn^{4+}$  species, and their changes in proportion  
781 with  $fO_2$ . At ~FMQ and below,  $Sn^{2+}$  is the predominant species in peraluminous melt compositions  
782 (Linnen et al., 1996; Farges et al., 2006), with an estimated ionic radius of 0.111 nm in VI-fold  
783 coordination (Uchida et al., 2002). Divalent Sn is therefore a poor fit for isovalent substitution with  
784  $Mg^{2+}$  (IR = 0.072 nm) or  $Fe^{2+}$  (IR = 0.078 nm) in biotite, whereas  $Sn^{4+}$  (IR=0.069 nm) is close in size to  
785  $Ti^{4+}$  (IR = 0.061 nm). The increase in  $D_{Sn^{bt/gl}}$  with increasing  $fO_2$  is therefore consistent with an  
786 increased abundance of  $Sn^{4+}$  and its preferential substitution for  $Ti^{4+}$  in the biotite structure. This  
787 interpretation is consistent with the experimental results of Wei et al. (2024) who found strong  
788 positive correlations between  $D_{Sn}$  and  $D_{Ti}$  for biotite and other ferromagnesium minerals obtained  
789 under highly oxidized conditions, at which the  $Sn^{4+}$  species would dominate. As for apatite,  
790 although the  $Sn^{2+}$  species would be a suitable fit for either of the two large cation sites in apatite (IR  
791 = 0.106 and 0.118 nm in VII- and IX-fold coordination), this is inconsistent with low values of  $D_{Sn^{ap/gl}}$   
792 for the lowest  $fO_2$  samples. However, when ionized to the  $2^+$  state, tin donates two 5p electrons

793 and obtains a stable filled  $5s^2$  electron configuration, resulting in an inert pair effect. This likely  
794 plays an inhibiting role for the incorporation of  $Sn^{2+}$  into apatite (and likely biotite as well), which  
795 would otherwise be a suitable fit from size considerations alone. In contrast to the  $2^+$  species,  $Sn^{4+}$   
796 lacks the filled shell configuration, and therefore would have a higher affinity for the apatite  
797 structure. In tetrahedral coordination, the IR of Sn (0.055 nm) is relatively close to the IR of Ge  
798 (0.039 nm), which is one of the most compatible trace elements in the apatite structure ( $D_{Ge}^{ap/gl}$  of  
799  $\sim 8-20$ ). Therefore, despite  $Sn^{4+}$  being a poorer fit than  $Sn^{2+}$ , the more favorable bonding  
800 environment for the former seems to overcome this size mismatch, accounting for the increase in  
801  $D_{Sn}^{ap/gl}$  with  $fO_2$ . High melt oxidation is experimentally demonstrated to enhance Sn compatibility in  
802 Ti-oxide minerals (Huang et al., 2024), ferromagnesian minerals, Ti-magnetite, and spinel (Wei et al.,  
803 2024) with the latter study explaining the low compatibility of  $Sn^{2+}$  to its electron configuration  
804 (“lone electron pair effect”). This effect on orbital interaction of post-transitional metal cations such  
805 as  $Sn^{2+}$  and  $Pb^{2+}$  is reviewed by Walsh et al. (2011) and its influence on mineral/melt partitioning has  
806 been recognized by Wood & Blundy (2013).

807 Arsenic is found to become more compatible in apatite with increasing  $fO_2$  (from 0.04 to  
808 1.6). This element was not detected in biotite from most samples, however, thus precluding  $D_{As}^{bt/gl}$   
809 estimates. In silicate melts, arsenic is present as  $As^{3+}$  and  $As^{5+}$  in proportions primarily controlled by  
810 the  $fO_2$  with the  $As^{3+}$  being the dominant species in natural silicate melts (Maciag & Brenan, 2020).  
811 Pentavalent arsenic, however, likely is compatible with apatite as it enters solid solutions with  
812 apatites forming the arsenate endmembers (Pan & Fleet, 2002), where  $As^{5+}$  (IR = 0.0335 nm in  
813 tetrahedral coordination) substitutes for  $P^{5+}$  (IR = 0.017 nm). Due to the size and charge mismatch  
814  $As^{3+}$  (IR = 0.058 in octahedral coordination) is much less likely to enter any of the cation sites in  
815 apatite structure. Thus, the increasing compatibility of As in apatite could be caused by a shift to  
816 higher melt  $As^{5+}/As^{3+}$  values, a prediction borne out by the apatite/melt partitioning experiments  
817 reported by Maciag (2023) involving felsic melt compositions.

818 Tungsten is incompatible in both minerals, with  $D_W^{bt/gl}$  decreasing with  $fO_2$ , but no  
819 systematic change in  $D_W^{ap/gl}$  across the same  $fO_2$  interval. The decrease in  $D_W^{bt/gl}$  could result from a  
820 change in speciation from  $W^{4+}$  to  $W^{6+}$ , as  $W^{4+}$  has an IR=0.066 nm, allowing a good fit into the biotite  
821 octahedral site, with an appropriate charge compensation mechanism (e.g.,  ${}^VI Fe^{3+} + {}^IV Si^{4+} = {}^VI W^{4+} +$

822 <sup>IV</sup>Al<sup>3+</sup>). On the contrary, partitioning of W<sup>6+</sup> into either biotite or apatite is inhibited by the large  
823 excess of charge, and the general exclusion of W<sup>6+</sup> from silicate minerals is well documented (e.g.,  
824 Fonseca et al., 2014). Although the change in  $D_W^{bt/gl}$  seems consistent with a change in speciation,  
825 available W solubility data indicates that the  $fO_2$  at which the transition from W<sup>4+</sup> to W<sup>6+</sup> takes place  
826 is ~FMQ-7 (O'Neill et al., 2008), which is far more reduced than the conditions recorded by the  
827 sample suite. In contrast, Fonseca et al. (2014) provide evidence from mineral-melt partitioning  
828 experiments for the presence of W<sup>4+</sup> and W<sup>6+</sup> in the range of FMQ to FMQ-4, as revealed by large  
829 changes in the  $D_W^{mineral/melt}$  for olivine and pyroxene. Fonseca et al. (2014) account for this  
830 discrepancy with the solubility data by proposing that melt composition plays a role in W speciation  
831 and the activity coefficients of the species (O'Neill et al., 2008), which amplify even minor changes in  
832 the abundance of W<sup>4+</sup> and W<sup>6+</sup>. Similarly, the transition from Mo<sup>4+</sup> to Mo<sup>6+</sup> is detectable in the MgO-  
833 Al<sub>2</sub>O<sub>3</sub>-SiO<sub>2</sub> system at almost 2 log units higher  $fO_2$  than melts in the CaO-Al<sub>2</sub>O<sub>3</sub>-SiO<sub>2</sub> system (O'Neill  
834 and Eggins, 2002). Our results for Mo partitioning between biotite and glass, indeed, follow a similar  
835 pattern to tungsten with decreasing compatibility ( $D_W^{bt/gl} = 2 - 0.1$ ) reflecting a transition from the  
836 compatible Mo<sup>4+</sup> (IR = 0.065 nm in octahedral coordination) to the highly charged, incompatible  
837 Mo<sup>6+</sup> (IR = 0.059 nm), which takes place at more oxidized conditions (~FMQ-4; Holzheid et al., 1994),  
838 closer to the  $fO_2$  range of the sample group. Therefore, a higher proportion of the compatible Mo<sup>4+</sup>  
839 could lead to a higher  $D_{Mo}^{bt/gl}$  values in comparison  $D_W^{bt/gl}$ . As molybdenum was not detected in  
840 most of the sampled apatite compositions,  $D_{Mo}^{ap/gl}$  could not be determined.

841 The values of  $D_{Eu}^{ap/gl}$  increase with more oxidizing conditions, but  $D_{Eu}^{bt/gl}$  appears to be in a  
842 negative correlation with the igneous  $fO_2$  (Figure 10b,c), however, in the Revancha samples, the Eu  
843 content in biotite and glasses is close to the detection limits thus resulting in a high uncertainty of  
844  $D_{Eu}^{bt/gl}$ . Europium in silicate melts is present in two valence states – Eu<sup>2+</sup> and Eu<sup>3+</sup> (Drake, 1975).  
845 Experimental studies have shown that both valence states are present over the  $fO_2$  range  
846 represented by the sample suite, and that the  $Eu^{3+}/\Sigma Eu$  increases with  $fO_2$  (as well as T, and  
847 decreasing melt polymerization; Burnham et al., 2015). Due to the larger size (0.120 nm in VII-fold  
848 coordination), Eu<sup>2+</sup> is expected to be less compatible than Eu<sup>3+</sup> (0.101 pm in VII-fold coordination)  
849 with either cation site in apatite. The observed increase in  $D_{Eu}^{ap/gl}$  with increasing  $fO_2$  is therefore  
850 consistent with the preferential uptake of the more compatible Eu<sup>3+</sup> relative to Eu<sup>2+</sup>.

851 Among the heterovalent elements reviewed in this study, vanadium D values appear to be  
852 redox-sensitive both in mineral/melt and intermineral partitioning. As the  $D_V^{ap/gl}$  and  $D_V^{bt/gl}$  exhibit  
853 distinctly diverging trends with  $fO_2$ , the redox sensitivity of vanadium intermineral partitioning is  
854 amplified, which suggests that  $D_V^{ap/bt}$  has the most potential for using as an oxybarometer. Hence,  
855 we focus the subsequent discussion on V partitioning systematics.

#### 856 **4.3. Estimate of the redox control on vanadium intermineral partitioning systematics**

857 As discussed above, the observed change in  $D_V^{ap/bt}$  is generally consistent with differences in  
858 species compatibility into the apatite and biotite structures as predicted from ionic radius and  
859 charge. However, a concern is whether the increase in  $D_V^{ap/bt}$  with  $fO_2$  is simply due to the  $fO_2$   
860 control on vanadium speciation, or reflects other factors that could influence species proportions  
861 without a change in  $fO_2$ , notably melt composition. To verify that the observed vanadium  
862 partitioning patterns originate predominantly from the redox control on heterovalent element  
863 species, we likewise plot a set of  $D^{ap/bt}$  for homovalent elements against the sample  $fO_2$  (Fig. 11).  
864 Partitioning of these elements should not be redox sensitive, but may be affected by other  
865 parameters such as melt composition or temperature. The recorded  $D^{ap/bt}$  are similar in most of the  
866 samples except the Mascota minette, which stands out as most of the homovalent  $D^{ap/bt}$  for this  
867 suite deviate from the rest of the group. The Mascota minette is set apart from the other samples  
868 both by its higher alkali content (Figure 2) and crystallization temperature (Table 1), which may have  
869 affected both the homovalent element and vanadium partitioning. The rest of the group is  
870 comprised of weakly to strongly peraluminous rocks which have crystallized at a lower T. The  
871 recorded  $D^{ap/bt}$  values of homovalent elements in these samples show no correlation with the  $fO_2$ ,  
872 thus precluding any role of other parameters overprinting the redox effect on heterovalent element  
873 partitioning.

874 The discrepancy between the trace element  $D^{ap/bt}$  in the Mascota minette and the other  
875 samples likely reflects influence of other factors that affect species proportions without a change in  
876  $fO_2$ , notably melt composition. This latter effect arises because the redox equilibria between the  
877 species of multivalent elements are controlled by the balance between the three kinds of oxygen  
878 bonding in the silicate melts: singly bonded  $O^-$ , doubly bonded  $O^0$ , and  $O^{2-}$ , free oxygen (Fincham &  
879 Richardson, 1954; Moretti, 2005).  $O^0$  forms a covalent bond with  $Si^{4+}$  or other highly charged

880 network formers in tetrahedral coordination (thus earning the name of bridging oxygens or T), but  
881 O- form ionic bonds with network modifiers and are therefore denoted as 'non-bridging oxygens'  
882 (NBO). The balance between the three kinds of oxygens in silicate melts is described in the following  
883 equation:



885 The ratio of NBO/T describes the melt structure and viscosity with values ranging between 0  
886 (fully polymerized melt) and 4 (fully depolymerized melt), yet in natural silicate melts, it generally  
887 varies between 0 and 1 (Mysen, 1983). As argued by Cicconi et al. (2020), melt alkali content  
888 inversely correlates with melt polymerization and optical basicity ( $\Lambda$ ), as the higher activity of alkalis  
889 increase  $\Lambda$  and depolymerizes the melt (increase NBO/T). Thus, the melt polymerization and its acid-  
890 base character, which determines the stability of heterovalent element ligands, are linked.  
891 Generally, the oxidation-reduction equilibria are expected to shift toward the more oxidized species  
892 with increasing melt basicity (higher NBO/T), which coincides with a lower degree of polymerization  
893 (Cicconi et al., 2020). However, as the heterovalent element equilibria are subject to both redox and  
894 acid-base chemistry, the potential amphoteric nature of one of the species (e.g.,  $\text{Fe}^{3+}$ ) can be  
895 affected by additional significant variables. For example, in peraluminous systems, increasing alkali  
896 content leads to stabilization of  $\text{Fe}^{2+}$ , while the opposite is true in metaluminous and peralkaline  
897 systems. This illustrates the necessity for experimental investigations of compositional controls of  
898 each equilibrium, which have proven to be essential in a number of studies on heterovalent element  
899 species and partitioning including iron (Cicconi et al., 2015; Dingwell & Virgo, 1987; Lange &  
900 Carmichael, 1987; Ottonello et al., 2001), sulphur (Nash et al., 2019; O'Neill & Mavrogenes, 2002),  
901 tin (Linnen et al., 1996), cerium (Smythe & Brenan, 2015), and vanadium (Arató & Audétat, 2017a;  
902 Leuthold et al., 2023; Mallmann & O'Neill, 2013; Sossi et al., 2018). The melt structural control of  
903 vanadium species in silicate systems was studied in experiments done by McKeown et al. (2011) and  
904 Wang et al. (2016). McKeown et al. measured the V speciation in borosilicate glasses synthesized at  
905 1050 °C and 0.1 MPa with varying alkali contents. They found a positive correlation between the  
906 melt  $\text{Na}_2\text{O}$  content and the average V oxidation state in the glass, measured by XANES. They remark  
907 that this is consistent with the results for Cr in less polymerized melts reported by Berry et al.  
908 (2006), in which a higher proportion of network modifying cations stabilizes the  $\text{Cr}^{3+}$  over  $\text{Cr}^{2+}$ .

909 Similarly, in their study of the CaO-MgO-Al<sub>2</sub>O<sub>3</sub>-SiO<sub>2</sub>-VO<sub>x</sub> system, Wang et al (2016) found that a  
 910 higher basicity, which they defined as (CaO+MgO)/(SiO<sub>2</sub>+Al<sub>2</sub>O<sub>3</sub>), stabilizes the higher oxidation state  
 911 of vanadium. As redox reactions are endothermic, higher temperatures are expected to stabilize the  
 912 reduced species – this is confirmed by the Wang et al., (2016) experiments for several compositions.  
 913 Therefore, we interpret the unusually large values of D<sub>V<sup>ap/bt</sup></sub> for the Mascota sample as likely the  
 914 result of melt composition (see below), even though the equilibration temperatures (1080-1100°C)  
 915 are higher than for the other sample suites (634-825°C). This illustrates the intricate interplay  
 916 between the intensive parameters controlling the speciation of vanadium and its partitioning  
 917 between the igneous species.

## 918 **5.0 Geological implications**

### 919 **5.1. Preliminary formulation of an apatite-biotite oxybarometer**

920 Towards quantifying the redox control on vanadium partitioning between apatite and biotite,  
 921 and its use in oxygen barometry, we present a preliminary partitioning model that takes into  
 922 account the change in proportion of the vanadium species with *f*O<sub>2</sub>, with estimates of the  
 923 partitioning of the endmember vanadium species.

924 The relevant model parameters are identified by first considering the relation describing the  
 925 individual mineral-melt coefficients (D<sub>V<sup>min/gl</sup></sub>), expressed as:

$$926 \quad D_V^{\text{min/gl}} = \frac{C_{V^{3+}}^{\text{min}} + C_{V^{4+}}^{\text{min}} + C_{V^{5+}}^{\text{min}}}{C_{V^{3+}}^{\text{gl}} + C_{V^{4+}}^{\text{gl}} + C_{V^{5+}}^{\text{gl}}} \quad (5)$$

927 In which C(V<sup>x+</sup>)<sup>min</sup> and C(V<sup>x+</sup>)<sup>gl</sup> are the concentrations of the vanadium species in the respective  
 928 mineral and melt. The contribution from V<sup>2+</sup> is assumed to be insignificant under the relatively  
 929 oxidized conditions of the sample suites considered (Sutton et al., 2005). For each vanadium  
 930 species, the individual mineral/melt partition coefficients can be expressed as:

$$931 \quad D_{V^{x+}}^{\text{min/gl}} = \frac{C_{V^{x+}}^{\text{min}}}{C_{V^{x+}}^{\text{gl}}} \quad (6)$$

932 Which can be substituted into equation 5 to remove the apatite or biotite compositional terms to  
 933 yield:

934

$$D_{V^{+}}^{\text{min/gl}} = \frac{D_{V^{3+}}^{\text{min/gl}} C_{V^{3+}}^{\text{min}} + D_{V^{4+}}^{\text{min/gl}} C_{V^{4+}}^{\text{min}} + D_{V^{5+}}^{\text{min/gl}} C_{V^{5+}}^{\text{min}}}{C_{V^{\text{total}}}^{\text{melt}}} \quad (7)$$

935

in which  $C_{V^{\text{total}}}^{\text{melt}}$  is the sum of the contributions of each vanadium species to the total

936

concentration in the melt. Considering just apatite/biotite partitioning ( $D_V^{\text{ap/bt}}$ ) yields the relation:

937

$$D_V^{\text{ap/bt}} = \frac{D_{V^{3+}}^{\text{ap/gl}} C_{V^{3+}}^{\text{gl}} + D_{V^{4+}}^{\text{ap/gl}} C_{V^{4+}}^{\text{gl}} + D_{V^{5+}}^{\text{ap/gl}} C_{V^{5+}}^{\text{gl}}}{D_{V^{3+}}^{\text{bt/gl}} C_{V^{3+}}^{\text{gl}} + D_{V^{4+}}^{\text{bt/gl}} C_{V^{4+}}^{\text{gl}} + D_{V^{5+}}^{\text{bt/gl}} C_{V^{5+}}^{\text{gl}}} \quad (8)$$

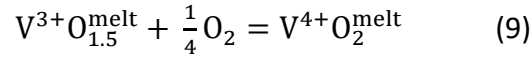
938

In terms of the speciation of vanadium, the relative proportions are governed by the homogenous

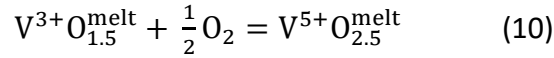
939

redox equilibria:

940



941



942

Assuming ideal solution behavior of the vanadium species (the activity of  $V^{x+}$  is therefore equal to

943

the mole fraction,  $X_{V^{x+}}$ ), the corresponding equilibrium constants,  $K_9$  and  $K_{10}$  are:

944

$$K_9 = \frac{X_{V^{4+}O_2}^{\text{melt}}}{X_{V^{3+}O_{1.5}}^{\text{melt}} \cdot f_{O_2}^{\frac{1}{4}}} \quad (11)$$

945

$$K_{10} = \frac{X_{V^{5+}O_{2.5}}^{\text{melt}}}{X_{V^{3+}O_{1.5}}^{\text{melt}} \cdot f_{O_2}^{\frac{1}{2}}} \quad (12)$$

946

The abundance of vanadium species at a given  $fO_2$  is determined using values of  $K_9$  and  $K_{10}$

947

estimated by Sossi et al. (2018) for a granitic composition measured from experiments done at 0.5

948

GPa and 800°C using magnetite-melt partitioning systematics. Estimates of  $D^{\text{ap/bt}}$  for the

949

endmember vanadium species were chosen from similar, homovalent “surrogate” trace elements,

950

i.e., Ga (IR = 0.062 nm) for  $V^{3+}$  and Ti (IR = 0.060 nm) for  $V^{4+}$ . For  $D_{V^{5+}}^{\text{ap/bt}}$ , however, no suitable

951

“surrogate” homovalent elements are available as both Nb and Ta have almost 2x larger ionic radii

952

in comparison to  $V^{5+}$ , therefore the value of  $D_{V^{5+}}^{\text{ap/bt}}$  was determined by least squares minimization

953

to match the modeled  $D_{\Sigma V}^{\text{ap/bt}}$  values to the measured ones while keeping the  $D_{V^{3+}}^{\text{ap/bt}}$  and  $D_{V^{4+}}^{\text{ap/bt}}$

954

equal to their “surrogate” values. Estimates for the endmember  $D_{V^{x+}}$  are provided in Table 6. The

955

value for  $D_{V^{5+}}^{\text{ap/bt}}$  of 0.165, regressed from the measured  $D_{\Sigma V}^{\text{ap/bt}}$  values, is consistent with the

956 lattice strain-based  $D^{ap/bt}$  systematics for other pentavalent elements –  $P^{5+}$  (IR = 0.017 nm) and  
 957 identically-sized  $Ta^{5+}$  and  $Nb^{5+}$  (IR=0.064 nm). Assuming  $D_P^{ap/bt}$  as the upper D limit (element strongly  
 958 concentrated in apatite) and  $D_{Ta}^{ap/bt}$  as the lower limit (element strongly concentrated in biotite),  
 959 the modeled  $D_{V^{5+}}^{ap/bt}$  value falls within the expected D interval, describing a lesser compatibility in  
 960 apatite and a moderate compatibility with biotite.

961 The apatite/biotite vanadium partitioning systematics were subsequently calculated using  
 962 equations 8, 11 and 12 and a comparison of the calculated and measured partitioning is provided in  
 963 Figure 12. The associated uncertainty of the model is propagated from the uncertainties of the  
 964 equilibrium constants ( $\Delta K_9$  and  $\Delta K_{10}$ ), used for calculating the abundances of the vanadium species  
 965 ( $X_{V^{x+}} = \frac{V^{x+}}{\Sigma V}$ ), and the uncertainties of the  $D_{V^{x+}}^{ap/bt}$  values (Table 6) using the following equations:

$$966 \quad \sigma_{z_{V^{x+}}} = z_{V^{x+}} \sqrt{\left(\frac{\Delta D_{V^{x+}}^{ap/bt}}{D_{V^{x+}}^{ap/bt}}\right)^2 + \left(\frac{\Delta X_{V^{x+}}}{X_{V^{x+}}}\right)^2} \quad (13)$$

967 where  $z_{V^{x+}}$  is the product of intermineral partitioning coefficient ( $D_{V^{x+}}^{ap/bt}$ ),  $\sigma_{z_{V^{x+}}}$ ,  $\Delta D_{V^{x+}}^{ap/bt}$ ,  
 968  $\Delta X_{V^{x+}}$  are the associated uncertainties.  $\Delta X_{V^{x+}}$  is determined using the following equation:

$$969 \quad \Delta X_{V^{x+}} = X_{V^{x+}} \sqrt{\left(\frac{\Delta K_9}{K_9}\right)^2 + \left(\frac{\Delta K_{11}}{K_{11}}\right)^2} \quad (14).$$

970 The uncertainty of the modeled vanadium intermineral partition coefficient is determined using  
 971 the following equation:

$$972 \quad \sigma_{D_V^{ap/bt}} = \sqrt{\sigma_{z_{V^{3+}}}^2 + \sigma_{z_{V^{4+}}}^2 + \sigma_{z_{V^{5+}}}^2} \quad (15).$$

973 As presented in Figure 12, with the exception of the Mascota minette sample, the model  
 974 provides a very good description of the data for the suites with similar, peraluminous compositions,  
 975 capturing values largely within analytical uncertainty. Results of this modelling indicate that the  
 976 high compatibility of  $V^{3+}$  and  $V^{4+}$  in biotite and their low compatibility in apatite leads to  $V^{5+}$  as being  
 977 the most important species, as its abundance and  $D^{ap/bt}$  almost entirely determines the total  $D_V^{ap/bt}$ .  
 978 The model, although preliminary, therefore provides a first insight into the controls of vanadium  
 979 intermineral partitioning, and it seems clear that factors that affect the  $V^{5+}$  speciation and

partitioning will influence the accuracy of this method in oxybarometry. As mentioned in section 4.3, a number of studies have already shown that aspects of melt composition, particularly the presence of network-modifying cations, such as alkalis and alkaline earth elements, will affect the species proportions, and hence vanadium partitioning, at a given  $fO_2$ . Thus the model represents peraluminous melts and it can be used only in systems close to those used for its calibration.

## 5.2. Example of application to natural apatite and biotite-bearing samples

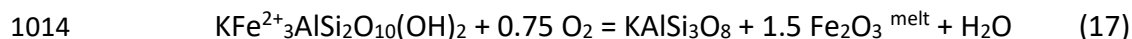
Currently, the most precise oxybarometry methods are based on the equilibrium between coexisting Fe-Ti oxides (Andersen & Lindsley, 1988; Carmichael, 1967; Ghiorso & Evans, 2008; Spencer & Lindsley, 1981) with other methods formulated from the mineral/melt partitioning of heterovalent elements (Arató & Audétat, 2017c; Burnham et al., 2015; Smythe & Brenan, 2016). Despite the widespread application of these approaches, oxybarometry of plutonic igneous systems, or those lacking one or both Fe-Ti-oxides, remains a challenge. Although a comprehensive application of apatite-biotite oxygen barometry awaits additional experimental calibration, and the more widespread availability of vanadium concentration data for apatite, we present here an example of how the method could be applied to rock suites for which direct  $fO_2$  determinations are unavailable.

The chosen suites represent samples provided from our own research collection for which coexisting apatite and biotite were measured using the identical analytical protocols as described in section 2.2. The suites comprise samples from the peraluminous South Mountain Batholith (SMB), Nova Scotia, Canada (Brenan et al., 2023). Petrographic evidence in the SMB suggest co-saturation in apatite and biotite as reflected by ubiquitous biotite-hosted apatite inclusions (Figure 13). Biotite crystallization temperatures for the SMB are estimated to be in the range of 603-722°C (Brenan et al., 2023), so temperatures and melt compositions are similar to the natural calibration dataset.

The vanadium content of apatite and biotite from 18 samples encompassing 9 constituent plutons of the SMB are reported in Supplementary Table ST4 and ST5. The resulting sample-specific mean values of  $D_V^{ap/bt}$  were used to determine the  $fO_2$  following the V intermineral partitioning model (Figure 12a) using the following approximation:

$$f_{O_2}[\Delta FMQ] = 1.25 \ln \left( \frac{D_V^{ap/bt}}{0.1284 - D_V^{ap/bt}} \right) - \frac{0.0033}{D_V^{bt}} + 18.3401 \left( D_V^{ap/bt} - \frac{0.1284}{2} \right) + 4.2802 \quad (16)$$

1007 Vanadium intermineral partitioning oxybarometry of the SMB suggest broad  $fO_2$  ranges and  
 1008 generally reduced to strongly reduced conditions in the complex (FMQ-5.5 to FMQ+1) and individual  
 1009 plutons (Figure 12b). In comparison, SMB Ce-in-zircon oxybarometry Bickerton et al. (2022) produce  
 1010 similarly broad  $fO_2$  ranges (Figure 12c), which overlap with the  $D_V^{ap/bt}$ -based determinations. The  
 1011 wide  $fO_2$  ranges measured by both methods are consistent with melt oxidation during the granitoid  
 1012 differentiation. This is suggested by alternative SMB  $fO_2$  estimates based on biotite Fe#, which is  
 1013 affected by a heterogenous redox equilibrium:



1015 Applying this equilibrium to the multicomponent natural system, Brenan et al. (2023) used the  
 1016 MELTS thermodynamic model to track biotite compositional evolution in SMB samples as a function  
 1017 of  $fO_2$ . Their results indicate biotite crystallization  $fO_2$  of FMQ to FMQ-1 in majority of the SMB, but  
 1018 evolved biotite compositions in the stage 2 plutons are consistent with equilibration at  $fO_2$  of FMQ  
 1019 and above it. This is consistent with the highest  $fO_2$  values determined from  $D_V^{ap/bt}$  in Davis Lake  
 1020 Pluton (FMQ+1). Melt oxidation during granitoid fractionation has been documented in several  
 1021 other systems, for example, Beauvoir granite (France; Cuney et al., 1992; Pichavant, 2022),  
 1022 Finnmarka Complex (Norway; Czamanske & Wones, 1973), Gangotri leucogranites (Northern India;  
 1023 Scaillet et al., 1995), and Mogok-Mergui magmatic belt (Myanmar; Li et al., 2024).

## 1024 **6. Conclusions**

1025 Results reported in this study show that the partitioning of vanadium and other heterovalent  
 1026 elements (As, Eu, Mo, Sn, W) between apatite, biotite and high silica glass change with sample redox  
 1027 state. With increasing  $fO_2$  from FMQ-3.6 to FMQ+2.9, vanadium becomes more compatible in  
 1028 apatite, ( $D_V^{ap/gl}$  from  $\sim 0.6$  to  $\sim 5$ ), and less compatible in biotite, ( $D_V^{bt/gl}$  from  $\sim 580$  to  $\sim 50$ ). Over the  
 1029 same  $fO_2$  interval, tin compatibility increases in both minerals ( $D_{Sn}^{ap/gl}$  from 0.05-0.3,  $D_{Sn}^{bt/gl}$  from 0.1-  
 1030 1), europium compatibility increases in apatite ( $D_{Eu}^{ap/gl}$  from  $\sim 20$ - $\sim 90$ ), and tungsten compatibility  
 1031 decreases in biotite ( $D_W^{bt/gl}$  from  $\sim 0.13$  to  $\sim 0.02$ ). Given the diverging  $fO_2$  trends for  $D_V^{bt/gl}$  and  
 1032  $D_V^{ap/gl}$ , the vanadium partitioning between apatite and biotite is amplified from values of  $\sim 0.001$  at  
 1033 FMQ-3.6 to  $\sim 0.5$  at FMQ+6.2. Comparison of partitioning for an internally consistent dataset of  
 1034 homovalent elements also collected in this study suggests that the changes in partitioning behaviour

1035 of the heterovalent elements are primarily controlled by the  $fO_2$ . Based on these results, a  
1036 preliminary model of  $D_V^{ap/bt}$  applicable to high-silica, peraluminous systems is developed. The model  
1037 reveals that the species abundance and  $D^{ap/bt}$  of  $V^{5+}$  almost entirely determines the total  $D_V^{ap/bt}$ .  
1038 Vanadium intermineral partitioning in the peraluminous South Mountain Batholith (SMB) implies  
1039 reducing conditions ( $\sim$ FMQ-5.5 to FMQ+1 with mean value of FMQ-1.5) consistent with  $fO_2$   
1040 determinations from independent phase-equilibria-based models and zircon-melt partitioning.  
1041 Further experimental studies of vanadium partitioning between apatite and biotite are necessary to  
1042 quantify melt and/or mineral compositional effects.

1043 Previous experimental studies of mineral-melt partitioning relations involving  
1044 ferromagnesian phases (pyroxene, olivine, Fe-Ti oxides; Arató & Audétat, 2017a; Mallmann &  
1045 O'Neill, 2009, 2013) for vanadium have established that  $D_V$  decreases with increasing  $fO_2$ , owing to  
1046 the increasingly poor mismatch between the higher valence vanadium species and the dominant  
1047 substituent cations in these phases. Because of this systematic partitioning relationship,  
1048 intermineral partitioning of vanadium involving these phases shows little change with  $fO_2$ . Minerals  
1049 that exhibit exceptions to this behavior are rutile (Holycross & Cottrell, 2020, 2022) and apatite (this  
1050 study), in which the  $V^{5+}$  species is the most compatible. Although the distribution of rutile is  
1051 somewhat more restricted to specific igneous bulk compositions, apatite is a ubiquitous phase in  
1052 compositions ranging from lunar basalts to high silica rhyolites (McCubbin & Jones, 2015; Webster &  
1053 Piccoli, 2015). Hence, the change in apatite/biotite partitioning of vanadium documented in this  
1054 study is almost certainly to be seen for the cases of apatite in equilibrium with pyroxenes, olivine  
1055 and Fe-Ti oxides, providing the basis for a number of potentially new oxybarometers applicable to a  
1056 range of rock-types.

#### 1057 **Author statement**

1058 **Peteris Rozenbaks:** methodology, investigation, formal analysis, validation, data curation, writing,  
1059 visualization. **James Brennan:** conceptualization, supervision, writing, visualization, project  
1060 administration, funding acquirement.

1061 **Acknowledgements**

1062           The authors acknowledge research funding provided by the Natural Resources Canada  
1063 Targeted Geoscience Initiative and the NSERC Discovery Grant program. Student support was  
1064 provided to Rozenbaks through a Doctoral Award from the Department of Earth and Environmental  
1065 Sciences at Dalhousie University and a Nova Scotia Graduate Scholarship. Drs Ray Donelick, Craig  
1066 Chesner, Hamish Sandeman, John Hanchar, Jacob Hanley, and the Smithsonian Institution are  
1067 thanked for providing rock samples analysed in this study. Ms. Natasha Drage, Drs Yanan Liu, Xiang  
1068 Yang, Brandon Boucher and Bryan Maciag are thanked for their support in the SEM, EPMA, and LA-  
1069 ICP-MS analyses. The manuscript has greatly benefited from reviews by Drs Saskia Erdman, Austin  
1070 Gion, and an anonymous reviewer.

1071 **Data availability**

1072           Data are available via Mendeley Data at DOI: [10.17632/fb37x69jcd.1](https://doi.org/10.17632/fb37x69jcd.1)

1073 **List of figures**

1074 **Figure 1.** Backscattered electron (BSE) images of biotite and apatite occurrences in the investigated  
1075 rock suites. A) Fish Canyon tuff showing chemically uniform biotite with typical bent and broken  
1076 textures. B) MAC137 is a biotite microphenocryst-rich sample of the glassy, flow-banded Revancha  
1077 dike facies showing both zoned and “spongy-textured” generation of biotite in apparent  
1078 disequilibrium (biotite on left side) along with relatively unzoned, euhedral biotites (e.g., crystal with  
1079 bt02, bt03 labels and laser ablation analysis scars). C) MAC2 is a sample of the crystal-poor facies of  
1080 the Revancha dike glassy chill margin, however, the biotite shows a similar textural distinction  
1081 between the older and younger biotite generations. D) Apatite occurrences in Revancha dyke  
1082 (MAC137) – subhedral, inclusion-rich apatite (on the right) and euhedral, inclusion-poorer apatite  
1083 (on the left). E) Biotite and apatite occurrences in Cerro Esquinani stock (MAC160): euhedral and  
1084 subhedral biotite, apatite phenocryst with a partially resorbed core and a biotite-hosted apatite  
1085 inclusion. F) Mascota minette euhedral and subhedral biotite with laser ablation scars and acicular  
1086 apatite set in a microcrystalline matrix. G) Occurrences of subhedral and euhedral apatite in  
1087 Mascota minette. H) Large euhedral biotite phenocryst in Tuk-Tuk tuff (TT). I) Apatite occurrences in  
1088 Tuk-Tuk tuff (TT7) as subhedral crystals set in vitreous matrix and hosted in a bent biotite crystal. J)  
1089 Unzoned subhedral and euhedral biotite occurrences in TT7. K) Biotite flake, extracted from  
1090 Umiakovik granite, contains apatite, ilmenite, and zircon inclusions. L) Zoned apatite in heavy  
1091 mineral separate from UP. Mineral abbreviations from (Whitney & Evans, 2010).

1092 **Figure 2.** Aluminium saturation and alkalinity of the analysed rock suites and glasses. Sources of the  
1093 whole rock compositional data provided in Table 1. Glass compositions from the Supplementary  
1094 Table 6.

1095 **Figure 3.** Plots of biotite compositional parameters: tetrahedral Al (a), Ti (b), Mn (c), Na (d), F/Cl (e),  
1096 Rb/K (f) as a function of Fe/(Fe+Mg) in biotite from the glassy volcanic suites from which natural  
1097 partitioning data were obtained. All values are calculated on the basis of 22 oxygen equivalents. The  
1098 field of peraluminous and metaluminous granites is taken from data compiled by Gion et al. (2022).  
1099 Field of lamprophyres taken from compilation by Saha et al. (2021). Demarcation based on Mn  
1100 content and Rb/K ratio is described in the text.

1101 **Figure 4.** Anion and rare earth element composition of apatite. a) Occupancy of the apatite anionic  
1102 site. OH abundance calculated assuming 2 anions per formula unit and subtracting the measured F  
1103 and Cl abundances. b) Mean chondrite-normalized REE composition of the apatites. Error bars  
1104 represent 1 SD of the apatite populations selected for D value calculations.

1105 **Figure 5.** Trace element concentration in the analyzed matrix glasses normalized to the average  
1106 upper crust (Rudnick & Gao, 2003). Symbols from the Figure 4.

1107 **Figure 6.** Summary of apatite/glass (a) and biotite/glass (b) partitioning coefficients determined in  
1108 this study compared to other studies of natural and experimental systems.

1109 **Figure 7.** Mineral/melt chemical equilibria in the glass-phyric suites analyzed in this study. **A)**  
1110 Biotite-glass Mg-Fe equilibrium. Gray lines represent the  $K_D$  for Mg-Fe exchange between biotite  
1111 and melt established by Were and Keppler (2021), mean value marked as a solid line, dashed lines  
1112 mark the maximal and minimal  $K_D(\text{Fe-Mg})$  values. Black dashed lines mark the range of  $K_D(\text{Fe-Mg})$   
1113 values determined by Icenhower & London (1997). Equilibrium in Were & Keppler experiments was  
1114 approached by a prolonged duration of the experiments (30-45 days) and was confirmed using  
1115 textural evidence and chemical uniformity of the phenocrysts and matrix glass. **B)** Apatite/glass  
1116 partition coefficient of strontium ( $D_{\text{Sr}}^{\text{ap/gl}}$ ) as a function of glass CaO. Experimental data from  
1117 Prowatke & Klemme (2006) and Watson & Green (1981). Prowatke and Klemme suggested trend of  
1118  $D_{\text{Sr}}$  in the mafic compositions in a correlation with the melt CaO. Data in this study lay near the  
1119 minimum CaO with high  $D_{\text{Sr}}$  values suggesting a continuation from the felsic Watson & Green  
1120 compositions. **C)** Comparison of natural and experimental ap/gl partition coefficients for samarium  
1121 as a function of the  $\text{SiO}_2$  content of the coexisting melt demonstrating the large increase in partition  
1122 coefficients with increasing  $\text{SiO}_2$ . Experimental data from Prowatke and Klemme (2006) and Watson  
1123 and Green (1981); natural partitioning studies from Brophy et al (2011), Li et al. (2023) and this  
1124 study.

1125 **Figure 8.** Major and trace element  $D^{\text{ap/gl}}$  values as a function of ionic radius in VIII-fold coordination.  
1126 Curves are produced as least square regressions to Eq. 3 for Na, K, Rb in monovalent array, Zn, Mg,  
1127 Fe, Ca, Sr, Ba in divalent array, REE and Y in trivalent array, Hf, Zr, Th in tetravalent array.  
1128 Pentavalent elements (P, Nb, Ta) lack sufficient datapoints to model the  $r_i$ - $D_i$  relationships. When  
1129 selecting the D values for the isovalent array fits, several elements were excluded from the  
1130 regression (Li for monovalent, Ga for trivalent, Si, Ti, Ge for tetravalent array) as their IR are  
1131 sufficiently small to enter the tetrahedral site, thus reducing the IR. Similarly, the heterovalent  
1132 elements (V, W, U) are not included in the fitting. Symbols from Fig. 4. Error bars depict uncertainty  
1133 of D, propagated from standard errors of element concentrations in apatite and glass.

1134 **Figure 9.** Major and trace element  $D^{\text{bt/gl}}$  values as a function of ionic radii. Curves are produced as  
1135 least square regressions to Eq. 3 for Na, K, Cs in XII-fold coordinated monovalent array, Mg, Co, Fe,  
1136 Mn in VI-fold coordinated divalent array, Si, Ge, Hf, Zr in IV-fold coordinated tetravalent array. In the  
1137  $\text{Al}^{\text{VI}}$ -rich Macusani biotite, it is assumed that the trivalent trace elements (Ga, In, Sc, Lu, Yb, Y)  
1138 exclusively enter the octahedral sites, whereas in the less-aluminous biotites of FCT and TT the two  
1139 smallest trivalent trace elements (Ga, In) enter the tetrahedral site and the other, larger trivalent  
1140 ions enter the octahedral site. Symbols from Fig. 4. Error bars depict uncertainty of D, propagated  
1141 from standard deviations of element concentrations in biotite and glass.

1142 **Figure 10.** Redox sensitive heterovalent element partitioning between biotite and melt (a,b),  
1143 apatite and melt (c,d), apatite and biotite (e,f). Error bars depict the reported range of  $f\text{O}_2$  and D  
1144 uncertainty propagated from standard errors of the element concentrations.

1145 **Figure 11.** Redox-sensitivity of homovalent element intermineral partitioning: trivalent (a),  
1146 tetravalent (b) and pentavalent (c) apatite/biotite partitioning coefficients as a function of oxygen  
1147 fugacity.

1148 **Figure 12.** A) Model of the  $D_{\Sigma V}^{ap/bt}$  as a function of oxygen fugacity in peraluminous melts. Inputs:  
1149 surrogate intermineral partitioning coefficient values from Table 6, abundances of V species from  
1150 Sossi et al. (2018). B) Variation of  $fO_2$  in the South Mountain Batholith determined using  $D_V^{ap/bt}$  and  
1151 Eq. 16. C) Variation of the  $fO_2$  in the South Mountain Batholith determined using Ce-in-zircon  
1152 oxybarometry by Bickerton et al. (2022).

1153 **Figure 13.** Backscattered electron images showing the textural relations for biotite and apatite  
1154 indicating co-crystallization of both phases in the peraluminous South Mountain Batholith (sample  
1155 BM0001, Cloud Lake Pluton).

1156 **List of tables**

1157 **Table 1.** Summary of the analysed samples. Sources of the compiled information and methodology:  
1158 Carmichael et al. (1996) – **1**, Chesner (1998) – **2**, Chesner (2012) – **3**, Emslie & Stirling (1993) – **4**,  
1159 Johnson & Rutherford (1989) – **5**, Kress & Carmichael (1991) – **6**, Loucks et al. (2020) – **7**, Righter &  
1160 Carmichael (1996) – **8**, Sandeman & Clark (2003) – **9**, Sandeman et al. (1997) – **10**, Smythe & Brennan  
1161 (2016) – **11**, Whitney & Stormer (1985) – **12**. Oxybarometry methods: zircon Ce-U-Ti for FCT<sup>7</sup>, MAC  
1162 (this study)<sup>7</sup>, TT<sup>7</sup>, Ce-in-zircon for UP<sup>11</sup>; melt Fe oxidation state<sup>6</sup> for MM<sup>1</sup>. All oxygen fugacity values  
1163 here are reported relative to the fayalite-magnetite-quartz mineral redox buffer ( $\Delta$ FMQ) defined by  
1164 O'Neill (1987).

1165 **Table 2.** Microanalytical conditions of EPMA and LA-ICP-MS used in this study.

1166 **Table 3.** Trace element partitioning between apatite and glass.

1167 **Table 4.** Trace element partitioning between biotite and glass.

1168 **Table 5.** Trace element partitioning between apatite and biotite.

1169 **Table 6.**  $D_V^{ap/bt}$  values used for the vanadium species in the partitioning model.

1170

1171 Appendix A. Supplementary Material

1172 Supplementary Material 1 – Descriptions of the analysed samples

1173

1174 Supplementary Figure S1 – Examples of Macusani zircon textures

1175 Supplementary Figure S2 – Summary of the sampled matrix glass major element compositions

1176 Supplementary Figure S3 – Summary of the sample suite whole-rock compositions

1177 Supplementary Figure S4 – Apatite trace element compositions

1178 Supplementary Figure S5 – Biotite trace element compositions

1179 Supplementary Figure S6 – Glass trace element compositions

1180 Supplementary Figure S7 – Comparison of trace element  $D^{bt/gl}$  values obtained from Macusani tuffs

1181 (Pichavant et al., 2024) and subvolcanics (this study)

1182 Supplementary Figure S8 – Comparison of trace element  $D^{bt/gl}$  values modelled by Bachmann et al.

1183 (2005) and measured in this study

1184 Supplementary Figure S9 – Chondrite-normalized REE abundance in Macusani apatites

1185 Supplementary Figure S10 – Homovalent element  $D^{ap/bt}$  values as a function of melt polymerization

1186

1187 Supplementary Table 1 - Summary of apatite, biotite, and glass major element compositions

1188 Supplementary Table 2 – Summary of apatite, biotite, and glass trace element compositions

1189 Supplementary Table 3 – Results of zircon analyses

1190 Supplementary Table 4 – Results of apatite EPMA analyses

1191 Supplementary Table 5 – Results of biotite EPMA analyses

1192 Supplementary Table 6 – Results of glass EPMA analyses

1193 Supplementary Table 7 – Results of apatite LA-ICP-MS analyses

1194 Supplementary Table 8 – Results of biotite LA-ICP-MS analyses

1195 Supplementary Table 9 – Results of glass LA-ICP-MS analyses

1196 Supplementary Table 10 – Mineral/melt partitioning Onuma plot parameters

1197 **References**

- 1198 Acosta-Vigil, A., Buick, I., Cesare, B., London, D., & Morgan, G. B. (2012). The extent of equilibration between  
1199 melt and residuum during regional anatexis and its implications for differentiation of the continental  
1200 crust: A study of partially melted metapelitic enclaves. *Journal of Petrology*, 53(7), 1319–1356.
- 1201 Andersen, D. J., & Lindsley, D. H. (1988). Internally consistent solution models for Fe-Mg-Mn-Ti oxides: Fe-Ti  
1202 oxides. *American Mineralogist*, 7(3), 714–726.
- 1203 Arató, R., & Audétat, A. (2017a). Experimental calibration of a new oxybarometer for silicic magmas based on  
1204 vanadium partitioning between magnetite and silicate melt. *Geochimica et Cosmochimica Acta*, 209,  
1205 284–295.
- 1206 Arató, R., & Audétat, A. (2017b). FeTiMM - A new oxybarometer for mafic to felsic magmas. *Geochemical  
1207 Perspectives Letters*, 5, 19–23.
- 1208 Arató, R., & Audétat, A. (2017c). Vanadium magnetite–melt oxybarometry of natural, silicic magmas: a  
1209 comparison of various oxybarometers and thermometers. *Contributions to Mineralogy and Petrology*,  
1210 172(7).
- 1211 Arevalo, R., & McDonough, W. F. (2008). Tungsten geochemistry and implications for understanding the  
1212 Earth's interior. *Earth and Planetary Science Letters*, 272(3–4), 656–665.
- 1213 Bachmann, O., Dungan, M. A., & Bussy, F. (2005). Insights into shallow magmatic processes in large silicic  
1214 magma bodies: the trace element record in the Fish Canyon magma body, Colorado. *Contributions to  
1215 Mineralogy and Petrology*, 149(3), 338–349.
- 1216 Bailey, S. W. (1984). Classification and structures of the micas. In S. W. Bailey (Ed.), *Micas. Reviews in  
1217 Mineralogy* (1st Edition, Vol. 13).
- 1218 Ballhaus, C., Berry, R. F., & Green, D. H. (1991). High-pressure experimental calibration of the olivine-  
1219 orthopyroxene-spinel oxygen geobarometer: implications for the oxidation state of the upper mantle.  
1220 *Contributions to Mineralogy and Petrology*, 107, 27–40.
- 1221 Ballouard, C., Massuyeau, M., Elburg, M. A., Tappe, S., Viljoen, F., & Brandenburg, J. T. (2020). The magmatic  
1222 and magmatic-hydrothermal evolution of felsic igneous rocks as seen through Nb-Ta geochemical  
1223 fractionation, with implications for the origins of rare-metal mineralizations. *Earth-Science Reviews*,  
1224 203.
- 1225 Beattie, P. (1994). Systematics and energetics of trace-element partitioning between olivine and silicate  
1226 melts: Implications for the nature of mineral/melt partitioning. *Chemical Geology*, 117, 57–71.
- 1227 Belousova, E. A., Walters, S., Griffin, W. L., & O'Reilly, S. Y. (2001). Trace-element signatures of apatites in  
1228 granitoids from the Mt Isa Inlier, Northwestern Queensland. *Australian Journal of Earth Sciences*, 48(4),  
1229 603–619.
- 1230 Berry, A. J., O'Neill, H. S. C., Scott, D. R., Foran, G. J., & Shelley, J. M. G. (2006). The effect of composition on  
1231 Cr<sup>2+</sup>/Cr<sup>3+</sup> in silicate melts. *American Mineralogist*, 91(11–12), 1901–1908.

- 1232 Bickerton, L., Kontak, D. J., Murphy, J. B., Kellett, D. A., Samson, I. M., Marsh, J. H., Dunning, G., & Stern, R.  
1233 (2022). The age and origin of the South Mountain Batholith (Nova Scotia, Canada) as constrained by  
1234 zircon U–Pb geochronology, geochemistry, and O–Hf isotopes. *Canadian Journal of Earth Sciences*,  
1235 59(7), 418–454.
- 1236 Bindeman, I. N., & Davis, A. M. (2000). Trace element partitioning between plagioclase and melt:  
1237 Investigation of dopant influence on partition behavior. *Geochimica et Cosmochimica Acta*, 64, 2863–  
1238 2878.
- 1239 Blundy, J., & Wood, B. (1994). Prediction of crystal-melt partition coefficients from elastic moduli. *Nature*,  
1240 372, 452–454.
- 1241 Brenan, J. M., Maciag, B. J., & Hanley, J. J. (2023). Geochemical variation in biotite from the Devonian South  
1242 Mountain Batholith, Nova Scotia: Constraints on emplacement pressure, temperature, magma redox  
1243 state and the development of a magmatic vapor phase (MVP). *American Mineralogist*, 108(11), 2004–  
1244 2023.
- 1245 Burnham, A. D., Berry, A. J., Halse, H. R., Schofield, P. F., Cibin, G., & Mosselmans, J. F. W. (2015). The  
1246 oxidation state of europium in silicate melts as a function of oxygen fugacity, composition and  
1247 temperature. *Chemical Geology*, 411, 248–259.
- 1248 Canil, D. (1999). Vanadium partitioning between orthopyroxene, spinel and silicate melt and the redox states  
1249 of mantle source regions for primary magmas. *Geochimica et Cosmochimica Acta*, 63(3/4), 557–572.
- 1250 Carmichael, I. S. E. (1967). The Iron-Titanium Oxides of Salic Volcanic Rocks and their Associated  
1251 Ferromagnesian Silicates. *Contributions to Mineralogy and Petrology*, 14, 36–64.
- 1252 Carmichael, I. S. E., & Ghiorso, M. S. (1990). The Effect of Oxygen Fugacity on the Redox State of Natural  
1253 Liquids and Their Crystallizing Phases. *Reviews in Mineralogy and Geochemistry*, 24, 191–212.
- 1254 Carmichael, I. S. E., Lange, R. A., & Luhr, J. F. (1996). Quaternary minettes and associated volcanic rocks of  
1255 Mascota, western Mexico: a consequence of plate extension above a subduction modified mantle  
1256 wedge. *Contributions to Mineralogy and Petrology*, 124, 302–333.
- 1257 Chesner, C. A. (1998). Petrogenesis of the Toba Tuffs, Sumatra, Indonesia. *Journal of Petrology*, 39(3), 397–  
1258 438.
- 1259 Chesner, C. A. (2012). The Toba Caldera Complex. *Quaternary International*, 258, 5–18.
- 1260 Chesner, C. A., Barbee, O. A., & McIntosh, W. C. (2020). The enigmatic origin and emplacement of the  
1261 Samosir Island lava domes, Toba Caldera, Sumatra, Indonesia. *Bulletin of Volcanology*, 82(3).
- 1262 Cicconi, M. R., Giuli, G., Ertel-Ingrisch, W., Paris, E., & Dingwell, D. B. (2015). The effect of the [Na/(Na+K)]  
1263 ratio on Fe speciation in phonolitic glasses. *American Mineralogist*, 100(7), 1610–1619.
- 1264 Cicconi, M. R., Le Losq, C., Moretti, R., & Neuville, D. R. (2020). Magmas are the Largest Repositories and  
1265 Carriers of Earth’s Redox Processes. *Elements*, 16(3), 173–178.
- 1266 Clarke, D. B., Renno, A. D., Hamilton, D. C., Gilbricht, S., & Bachmann, K. (2021). The spatial association of  
1267 accessory minerals with biotite in granitic rocks from the South Mountain Batholith, Nova Scotia,  
1268 Canada. *Geosphere*, 18(1), 1–18.

- 1269 Clarke, R. S., & Altschuler, Z. S. (1958). Determination of the oxidation state of uranium in apatite and  
1270 phosphorite deposits. *Geochimica et Cosmochimica Acta*, *13*, 127–141.
- 1271 Cottrell, E., Birner, S. K., Brounce, M., Davis, F. A., Waters, L. E., & Kelley, K. A. (2021). Oxygen Fugacity Across  
1272 Tectonic Settings. In *Magma Redox Geochemistry* (pp. 33–61).
- 1273 Cuney, M., Marignac, C., & Weisbrod, A. (1992). The Beauvoir Topaz-Lepidolite Albite Granite (Massif Central,  
1274 France): The Disseminated Magmatic Sn-Li-Ta-Nb-Be Mineralization. *Economic Geology*, *87*, 1766–179.
- 1275 Czamanske, G. K., & Wones, D. R. (1973). Oxidation During Magmatic Differentiation, Finnmarka Complex,  
1276 Oslo Area, Norway: Part 2, The Mafic Silicates. *Journal of Petrology*, *14*, 349–380.
- 1277 Dailey, S. R., Christiansen, E. H., Dorais, M. J., Kowallis, B. J., Fernandez, D. P., & Johnson, D. M. (2018). Origin  
1278 of the fluorine- and beryllium-rich rhyolites of the Spor Mountain Formation, Western Utah. *American  
1279 Mineralogist*, *103*(8), 1228–1252.
- 1280 Dingwell, D. B., & Virgo, D. (1987). The effect of oxidation state on the viscosity of melts in the system Na<sub>2</sub>O-  
1281 FeO-Fe<sub>2</sub>O<sub>3</sub>-SiO<sub>2</sub>. *Geochimica et Cosmochimica Acta*, *51*, 195–205.
- 1282 Drake, M. (1975). The oxidation state of europium as an indicator of oxygen fugacity. *Geochimica and  
1283 Cosmochimica Acta*, *39*, 55–64.
- 1284 Dymek, R. F. (1983). Titanium, aluminum and interlayer cation substitutions in biotite from high-grade  
1285 gneisses, West Greenland. *American Mineralogist*, *6*, 880–399.
- 1286 Elliott, J. C. (1994). Fluorapatite and Chlorapatite. In *Studies in Inorganic Chemistry* (Vol. 18, Issue C, pp. 63–  
1287 110).
- 1288 Emslie, R. F., & Loveridge, W. D. (1992). Fluorite-bearing Early and Middle Proterozoic granites, Okak Bay  
1289 area, Labrador: Geochronology, geochemistry and petrogenesis. *Lithos*, *28*, 87–109.
- 1290 Emslie, R. F., & Stirling, J. A. R. (1993). Rapakivi and related granitoids of the Nain plutonic suite:  
1291 geochemistry, mineral assemblages and fluid equilibria. *Canadian Mineralogist*, *31*(4), 821–847.
- 1292 Engel, G., Krieg, F., & Reif, G. (1975). Mischkristallbildung und Kationenordnung im System Bleihydroxylapatit-  
1293 Calciumhydroxylapatit. *Journal of Solid State Chemistry*, *15*, 117–126.
- 1294 Fincham, C. J. B., & Richardson, F. D. (1954). The behaviour of sulphur in silicate and aluminate melts.  
1295 *Proceedings of the Royal Society of London. Series A. Mathematical and Physical Sciences*, *223*, 40–62.
- 1296 Fonseca, R. O. C., Mallmann, G., Sprung, P., Sommer, J. E., Heuser, A., Speelmanns, I. M., & Blanchard, H.  
1297 (2014). Redox controls on tungsten and uranium crystal/silicate melt partitioning and implications for  
1298 the U/W and Th/W ratio of the lunar mantle. *Earth and Planetary Science Letters*, *404*, 1–13.
- 1299 Frost, B. R. (1991). Introduction to Oxygen Fugacity and Its Petrologic Importance. In D. H. Lindsley (Ed.),  
1300 *Oxide minerals: Petrologic and Magnetic Significance, Reviews in Mineralogy* (Vol. 25, pp. 1–10).
- 1301 Gaillard, F., Scaillet, B., Pichavant, M., & Iacono-Marziano, G. (2015). The redox geodynamics linking basalts  
1302 and their mantle sources through space and time. *Chemical Geology*, *418*, 217–233.

- 1303 Gao, M., Xiong, X., Huang, F., Wang, J., & Wei, C. (2023). Key Factors Controlling Biotite–Silicate Melt Nb and  
1304 Ta Partitioning: Implications for Nb–Ta Enrichment and Fractionation in Granites. *Journal of Geophysical*  
1305 *Research: Solid Earth*, 128(7).
- 1306 Giorso, M. S., & Evans, B. W. (2008). Thermodynamics of rhombohedral oxide solid solutions and a revision  
1307 of the Fe-Ti two-oxide geothermometer and oxygen-barometer. *American Journal of Science*, 308, 957–  
1308 1039.
- 1309 Giorso, M. S., & Sack, R. O. (1991). Fe-Ti oxide geothermometry: thermodynamic formulation and the  
1310 estimation of intensive variables in silicic magmas. *Contributions to Mineralogy and Petrology*, 108,  
1311 485–510.
- 1312 Gion, A. M., Piccoli, P. M., & Candela, P. A. (2018). Partitioning of indium between ferromagnesian minerals  
1313 and a silicate melt. *Chemical Geology*, 500, 30–45.
- 1314 Gion, A. M., Piccoli, P. M., & Candela, P. A. (2022). Characterization of biotite and amphibole compositions in  
1315 granites. *Contributions to Mineralogy and Petrology*, 177(4).
- 1316 Gleadow, A., Harrison, M., Kohn, B., Lugo-Zazueta, R., & Phillips, D. (2015). The Fish Canyon Tuff: A new look  
1317 at an old low-temperature thermochronology standard. *Earth and Planetary Science Letters*, 424, 95–  
1318 108.
- 1319 Henry, D. J., Guidotti, C. V., & Thomson, J. A. (2005). The Ti-saturation surface for low-to-medium pressure  
1320 metapelitic biotites: Implications for geothermometry and Ti-substitution mechanisms. *American*  
1321 *Mineralogist*, 90(2–3), 316–328.
- 1322 Holycross, M., & Cottrell, E. (2020). Partitioning of V and 19 other trace elements between rutile and silicate  
1323 melt as a function of oxygen fugacity and melt composition: Implications for subduction zones.  
1324 *American Mineralogist*, 105(2), 244–254.
- 1325 Holycross, M., & Cottrell, E. (2022). Experimental quantification of vanadium partitioning between eclogitic  
1326 minerals (garnet, clinopyroxene, rutile) and silicate melt as a function of temperature and oxygen  
1327 fugacity. *Contributions to Mineralogy and Petrology*, 177(2).
- 1328 Holzheid, A., Borisov, A., & Palme, H. (1994). The effect of oxygen fugacity and temperature on solubilities of  
1329 nickel, cobalt, and molybdenum in silicate melts. *Geochimica et Cosmochimica Acta*, 58(8).
- 1330 Huang, F., Wang, J., Xiong, X., Gao, M., Li, L., & Wei, C. (2024). Experimental determination of tin partitioning  
1331 between titanite, ilmenite and granitic melts using improved capsule designs. *American Mineralogist*.
- 1332 Icenhower, J., & London, D. (1995). An experimental study of element partitioning among biotite, muscovite,  
1333 and coexisting peraluminous silicic melt at 200 MPa (H<sub>2</sub>O). *American Mineralogist*, 80(11–12), 1229–  
1334 1251.
- 1335 Icenhower, J. P., & London, D. (1997). Partitioning of fluorine and chlorine between biotite and granitic melt:  
1336 experimental calibration at 200 MPa H<sub>2</sub>O. *Contributions to Mineralogy and Petrology*, 127, 17–29.
- 1337 Ji, D., & Dygert, N. (2024). Trace element partitioning between apatite and silicate melts: Effects of major  
1338 element composition, temperature, and oxygen fugacity, and implications for the volatile element  
1339 budget of the lunar magma ocean. *Geochimica et Cosmochimica Acta*, 369, 141–159.

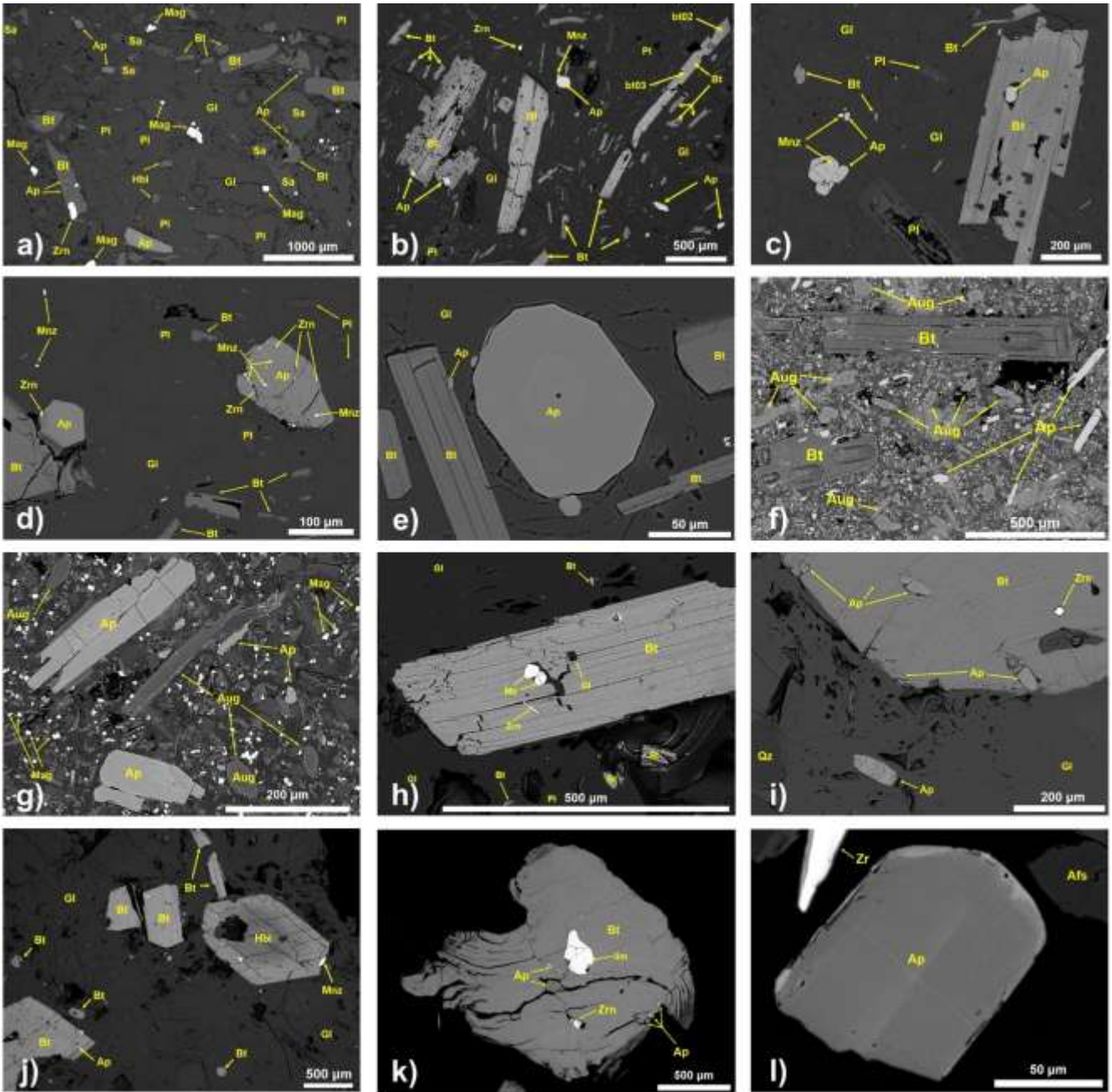
- 1340 Jochum, K. P., Nohl, U., Herwig, K., Lammel, E., Stoll, B., & Hofmann, A. W. (2005). GeoReM: A New  
1341 Geochemical Database for Reference Materials and Isotopic Standards. *Geostandards and Geoanalytical*  
1342 *Research*, 29(3), 333–338.
- 1343 Johnson, M. C., & Rutherford, M. J. (1989). Experimentally Determined Conditions in the Fish Canyon Tuff,  
1344 Colorado, Magma Chamber. *Journal of Petrology*, 30(3), 711–737.
- 1345 Klemme, S., & Dalpé, C. (2003). Trace-element partitioning between apatite and carbonatite melt. *American*  
1346 *Mineralogist*, 88, 639–646.
- 1347 Kreidler, E. R., & Hummel, F. A. (1970). The crystal chemistry of apatite: structure fields of fluor- and  
1348 chlorapatite. *The American Mineralogist*, 55, 170–184.
- 1349 Kress, V. C., & Carmichael, I. S. E. (1991). The compressibility of silicate liquids containing Fe<sub>2</sub>O<sub>3</sub> and the  
1350 effect of composition, temperature, oxygen fugacity and pressure on their redox states. *Contributions to*  
1351 *Mineralogy and Petrology*, 108, 82–92.
- 1352 Lange, R., & Carmichael, I. S. E. (1987). Densities of Na<sub>2</sub>O-K<sub>2</sub>O-CaO-MgO-FeO-Fe<sub>2</sub>O<sub>3</sub>-Al<sub>2</sub>O<sub>3</sub>-TiO<sub>2</sub>-SiO<sub>2</sub> liquids:  
1353 New measurements and derived partial molar properties. *Geochimica et Cosmochimica Acta*, 51, 293–  
1354 2946.
- 1355 LaTourrette, T., Hervig, R. L., & Holloway, J. R. (1995). Trace element partitioning between amphibole,  
1356 phlogopite, and basanite melt. *Earth and Planetary Science Letters*, 135, 13–30.
- 1357 Lee, C. T. A., Harbert, A., & Leeman, W. P. (2007). Extension of lattice strain theory to mineral/mineral rare-  
1358 earth element partitioning: An approach for assessing disequilibrium and developing internally  
1359 consistent partition coefficients between olivine, orthopyroxene, clinopyroxene and basaltic melt.  
1360 *Geochimica et Cosmochimica Acta*, 71(2), 481–496.
- 1361 Leuthold, J., Blundy, J., & Ulmer, P. (2023). Trace element partitioning in basaltic systems as a function of  
1362 oxygen fugacity. *Contributions to Mineralogy and Petrology*, 178(12).
- 1363 Li, J. X., Ding, L., Evans, N. J., Xu, F., Fan, W. M., Zhang, L. Y., Cai, F. L., Guan, Q. Y., Yue, Y. H., & Xie, J. (2024).  
1364 Garnet geochemistry reveals late-stage oxidation of tin-bearing fractionated granite. *Lithos*, 464–465.
- 1365 Li, W., Costa, F., Oppenheimer, C., & Nagashima, K. (2023). Volatile and trace element partitioning between  
1366 apatite and alkaline melts. *Contributions to Mineralogy and Petrology*, 178(2).
- 1367 Linnen, R. L., Pichavant, M., & Holtz, F. (1996). The combined effects of fO<sub>2</sub> and melt composition on SnO<sub>2</sub>  
1368 solubility and tin diffusivity in haplogranitic melts. *Geochimica et Cosmochimica Acta*, 60(24), 4965–  
1369 4976.
- 1370 Loucks, R. R., Fiorentini, M. L., & Henriquez, G. J. (2020). New magmatic oxybarometer using trace elements  
1371 in zircon. *Journal of Petrology*, 61(3).
- 1372 Luo, Y., Hughes, J. M., Rakovan, J., & Pan, Y. (2009). Site preference of U and Th in Cl, F, and Sr apatites.  
1373 *American Mineralogist*, 94(2–3), 345–351.
- 1374 Maciag, B. J., & Brenan, J. M. (2020). Speciation of arsenic and antimony in basaltic magmas. *Geochimica et*  
1375 *Cosmochimica Acta*, 276, 198–218.

- 1376 Mallmann, G., & O'Neill, H. St. C. (2009). The crystal/melt partitioning of V during mantle melting as a  
 1377 function of oxygen fugacity compared with some other elements (Al, P, Ca, Sc, Ti, Cr, Fe, Ga, Y, Zr and  
 1378 Nb). *Journal of Petrology*, 50(9), 1765–1794.
- 1379 Mallmann, G., & O'Neill, H. St. C. (2013). Calibration of an Empirical Thermometer and Oxybarometer Based  
 1380 on the Partitioning of Sc, Y and V between Olivine and Silicate melt. *Journal of Petrology*, 54(5), 933–  
 1381 949.
- 1382 Marks, M. A. W., Wenzel, T., Whitehouse, M. J., Loose, M., Zack, T., Barth, M., Worgard, L., Krasz, V., Eby, G.  
 1383 N., Stosnach, H., & Markl, G. (2012). The volatile inventory (F, Cl, Br, S, C) of magmatic apatite: An  
 1384 integrated analytical approach. *Chemical Geology*, 291, 241–255.
- 1385 McCubbin, F. M., & Jones, R. H. (2015). Extraterrestrial apatite: Planetary geochemistry to astrobiology.  
 1386 *Elements*, 11(3), 183–188.
- 1387 McDonough, W. F., & Sun, S. -s. (1995). The composition of the Earth. *Chemical Geology*, 120, 223–253.
- 1388 McFarlane, C. R. M., & Luo, Y. (2012). U-Pb Geochronology Using 193 nm Excimer LA-ICP-MS Optimized for In Situ  
 1389 Accessory Mineral Dating in Thin Sections. *Geoscience Canada*, 39(3), 158.
- 1390 McKeown, D. A., Muller, I. S., Gan, H., Feng, Z., Viragh, C., & Pegg, I. L. (2011). Vanadium and chromium redox  
 1391 behavior in borosilicate nuclear waste glasses. *Journal of Non-Crystalline Solids*, 357(14), 2735–2743.
- 1392 Moretti, R. (2005). Polymerisation, basicity, oxidation state and their role in ionic modelling of silicate melts.  
 1393 *Annals of Geophysics*, 48, 583–608.
- 1394 Moretti, R., & Neuville, D. (2021). Redox Equilibria: From Basic Concepts to the Magmatic Realm. In R.  
 1395 Moretti & D. Neuville (Eds.), *Magma Redox Geochemistry. Geophysical Monograph Series* (Vol. 266, pp.  
 1396 1–18).
- 1397 Mungall, J. E. (2002). Roasting the mantle: Slab melting and the genesis of major Au and Au-rich Cu deposits.  
 1398 *Geology*, 30, 915–918.
- 1399 Mysen, B. O. (1983). The structure of silicate melts. *Annual Review of Earth and Planetary Sciences*, 11, 75–  
 1400 97.
- 1401 Nash, W. M., Smythe, D. J., & Wood, B. J. (2019). Compositional and temperature effects on sulfur speciation  
 1402 and solubility in silicate melts. *Earth and Planetary Science Letters*, 507, 187–198.
- 1403 Nickel, E. H. (1954). The distribution of major and minor elements among some co-existing ferromagnesian  
 1404 silicates. *American Mineralogist*, 39, 486–493.
- 1405 O'Neill, H. S. C., Berry, A. J., & Eggins, S. M. (2008). The solubility and oxidation state of tungsten in silicate  
 1406 melts: Implications for the comparative chemistry of W and Mo in planetary differentiation processes.  
 1407 *Chemical Geology*, 255(3–4), 346–359.
- 1408 O'Neill, H. St. C. (1987). Quartz-fayalite-iron and quartz-fayalite-magnetite equilibria and the free energy of  
 1409 formation of fayalite (Fe<sub>2</sub>SiO<sub>4</sub>) and magnetite (Fe<sub>3</sub>O<sub>4</sub>). *American Mineralogist*, 72, 67–75.
- 1410 O'Neill, H. St. C., & Mavrogenes, J. A. (2002). The Sulfide Capacity and the Sulfur Content at Sulfide Saturation  
 1411 of Silicate Melts at 1400°C and 1 bar. *Journal of Petrology*, 43, 1049–1087.

- 1412 Onuma, N., Higuchi, H., Wakita, H., & Nagasawa, H. (1968). Trace element partition between two pyroxenes  
1413 and the host lava. *Earth and Planetary Science Letters*, 5, 47–51.
- 1414 Ottonello, G., Moretti, R., Marini, L., & Zuccolini, M. V. (2001). Oxidation state of iron in silicate glasses and  
1415 melts: a thermochemical model. *Chemical Geology*, 174, 157–179.
- 1416 Padilla, A. J., & Gualda, G. A. R. (2016). Crystal-melt elemental partitioning in silicic magmatic systems: An  
1417 example from the Peach Spring Tuff high-silica rhyolite, Southwest USA. *Chemical Geology*, 440, 326–  
1418 344.
- 1419 Pan, Y., & Fleet, M. E. (2002). Compositions of the Apatite-Group Minerals: Substitution Mechanisms and  
1420 Controlling Factors. *Phosphates: Geochemical, Geobiological and Materials Importance. Reviews in  
1421 Mineralogy and Geochemistry*, 48, 13–50.
- 1422 Paton, C., Hellstrom, J., Paul, B., Woodhead, J., & Hergt, J. (2011). Lolite: Freeware for the visualisation and  
1423 processing of mass spectrometric data. *Journal of Analytical Atomic Spectrometry*, 26(12), 2508–2518.
- 1424 Pichavant, M. (2022). Experimental crystallization of the Beauvoir granite as a model for the evolution of  
1425 Variscan rare metal magmas. *Journal of Petrology*, 63(12), egac120.
- 1426 Pichavant, M., Erdmann, S., Kontak, D. J., Michaud, J. A. S., & Villaros, A. (2024). Trace element partitioning in  
1427 strongly peraluminous rare-metal silicic magmas – Implications for fractionation processes and for the  
1428 origin of the Macusani Volcanics (SE Peru). *Geochimica et Cosmochimica Acta*, 229–252.
- 1429 Pichavant, M., Kontak, D. J., Briqueu, L., Herrera, J. V., & Clark, A. H. (1988a). The Miocene-Pliocene Macusani  
1430 Volcanics, SE Peru. *Contributions to Mineralogy and Petrology*, 100(3), 300–324.
- 1431 Pichavant, M., Kontak, D. J., Briqueu, L., Herrera, J. V., & Clark, A. H. (1988b). The Miocene-Pliocene Macusani  
1432 Volcanics, SE Peru II. Geochemistry and origin of a felsic peraluminous magma. *Contributions to  
1433 Mineralogy and Petrology*, 100(3), 325–338.
- 1434 Pichavant, M., Villaros, A., Deveaud, S., Scaillet, B., & Lahfafi, M. (2016). The influence of redox state on mica  
1435 crystallization in leucogranitic and pegmatitic liquids. *Canadian Mineralogist*, 54, 559–581.
- 1436 Pidgeon, R. T. (1992). Recrystallisation of oscillatory zoned zircon: some geochronological and petrological  
1437 implications. *Contributions to Mineralogy and Petrology*, 110, 463–472.
- 1438 Prowatke, S., & Klemme, S. (2006). Trace element partitioning between apatite and silicate melts. *Geochimica  
1439 et Cosmochimica Acta*, 70(17), 4513–4527.
- 1440 Righter, K., & Carmichael, I. S. E. (1996). Phase equilibria of phlogopite lamprophyres from western Mexico:  
1441 biotite-liquid equilibria and P-T estimates for biotite-bearing igneous rocks. *Contrib Mineral Petrol*, 123,  
1442 1–21.
- 1443 Rudnick, R. L., & Gao, S. (2003). Composition of the Continental Crust. In *Treatise on Geochemistry* (Vols. 3–9,  
1444 pp. 1–64). Elsevier Inc.
- 1445 Saha, R., Upadhyay, D., & Mishra, B. (2021). Discriminating Tectonic Setting of Igneous Rocks Using Biotite  
1446 Major Element chemistry—A Machine Learning Approach. *Geochemistry, Geophysics, Geosystems*,  
1447 22(11).

- 1448 Sandeman, H. A., & Clark, A. H. (2003). Glass-rich, Cordierite-Biotite Rhyodacite, Valle Ninahuisa, Puno, SE  
1449 Peru: Petrological evidence for hybridization of “Lachlan S-type” and potassic mafic magmas. *Journal of*  
1450 *Petrology*, 44(2), 355–385.
- 1451 Sandeman, H. A., & Clark, A. H. (2004). Commingling and mixing of S-type peraluminous, ultrapotassic and  
1452 basaltic magmas in the Cayconi volcanic field, Cordillera de Carabaya, SE Peru. *Lithos*, 73(3–4), 187–213.
- 1453 Sandeman, H. A., Clark, A. H., Farrar, E., & Arroyo-Pauca, G. (1997). Lithostratigraphy, petrology and <sup>40</sup>Ar-  
1454 <sup>39</sup>Ar geochronology of the Crucero Supergroup, Puno Department, SE Peru. *Journal of South American*  
1455 *Earth Sciences*, 10(3–4), 223–245.
- 1456 Scaillet, B., Pichavant, M., & Roux, J. (1995). Experimental Crystallization of Leucogranite Magmas. *Journal of*  
1457 *Petrology*, 36, 663–705.
- 1458 Schmidt, K. H., Bottazzi, P., Vannucci, R., & Mengel, K. (1999). Trace element partitioning between  
1459 phlogopite, clinopyroxene and leucite lamproite melt. *Earth and Planetary Science Letters*, 168, 287–  
1460 299.
- 1461 Schreiber, H. D. (1983). The chemistry of uranium in glass-forming aluminosilicate melts. *Journal of the Less-*  
1462 *Common Metals*, 91, 129–147.
- 1463 Shimizu, K., Liang, Y., Sun, C., Jackson, C. R. M., & Saal, A. E. (2017). Parameterized lattice strain models for  
1464 REE partitioning between amphibole and silicate melt. *American Mineralogist*, 102(11), 2254–2267.
- 1465 Smythe, D. J., & Brenan, J. M. (2015). Cerium oxidation state in silicate melts: Combined fO<sub>2</sub>, temperature  
1466 and compositional effects. *Geochimica et Cosmochimica Acta*, 170, 173–187.
- 1467 Smythe, D. J., & Brenan, J. M. (2016). Magmatic oxygen fugacity estimated using zircon-melt partitioning of  
1468 cerium. *Earth and Planetary Science Letters*, 453, 260–266.
- 1469 Sossi, P. A., Prytulak, J., & O’Neill, H. S. C. (2018). Experimental calibration of vanadium partitioning and  
1470 stable isotope fractionation between hydrous granitic melt and magnetite at 800 °C and 0.5 GPa.  
1471 *Contributions to Mineralogy and Petrology*, 173(4).
- 1472 Spencer, K. J., & Lindsley, D. H. (1981). A solution model for coexisting iron-titanium oxides. *American*  
1473 *Mineralogist*, 66, 1189–1201.
- 1474 Stokes, T. N., Bromiley, G. D., Potts, N. J., Saunders, K. E., & Miles, A. J. (2019). The effect of melt composition  
1475 and oxygen fugacity on manganese partitioning between apatite and silicate melt. *Chemical Geology*,  
1476 506, 162–174.
- 1477 Sutton, S. R., Karner, J., Papike, J., Delaney, J. S., Shearer, C., Newville, M., Eng, P., Rivers, M., & Dyar, M. D.  
1478 (2005). Vanadium K edge XANES of synthetic and natural basaltic glasses and application to microscale  
1479 oxygen barometry. *Geochimica et Cosmochimica Acta*, 69(9), 2333–2348.
- 1480 Taylor, W. R., & Green, D. H. (1988). Measurement of reduced peridotite-C-O-H solidus and implications for  
1481 redox melting of the mantle. *Nature*, 332(6162), 349–352.
- 1482 Virgo, D., Mysen, B. O., & Kushiro, I. (1980). Anionic Constitution of 1-Atmosphere Silicate Melts: Implications  
1483 for the Structure of Igneous Melts. *Science*, 208(4450), 1371–1373.

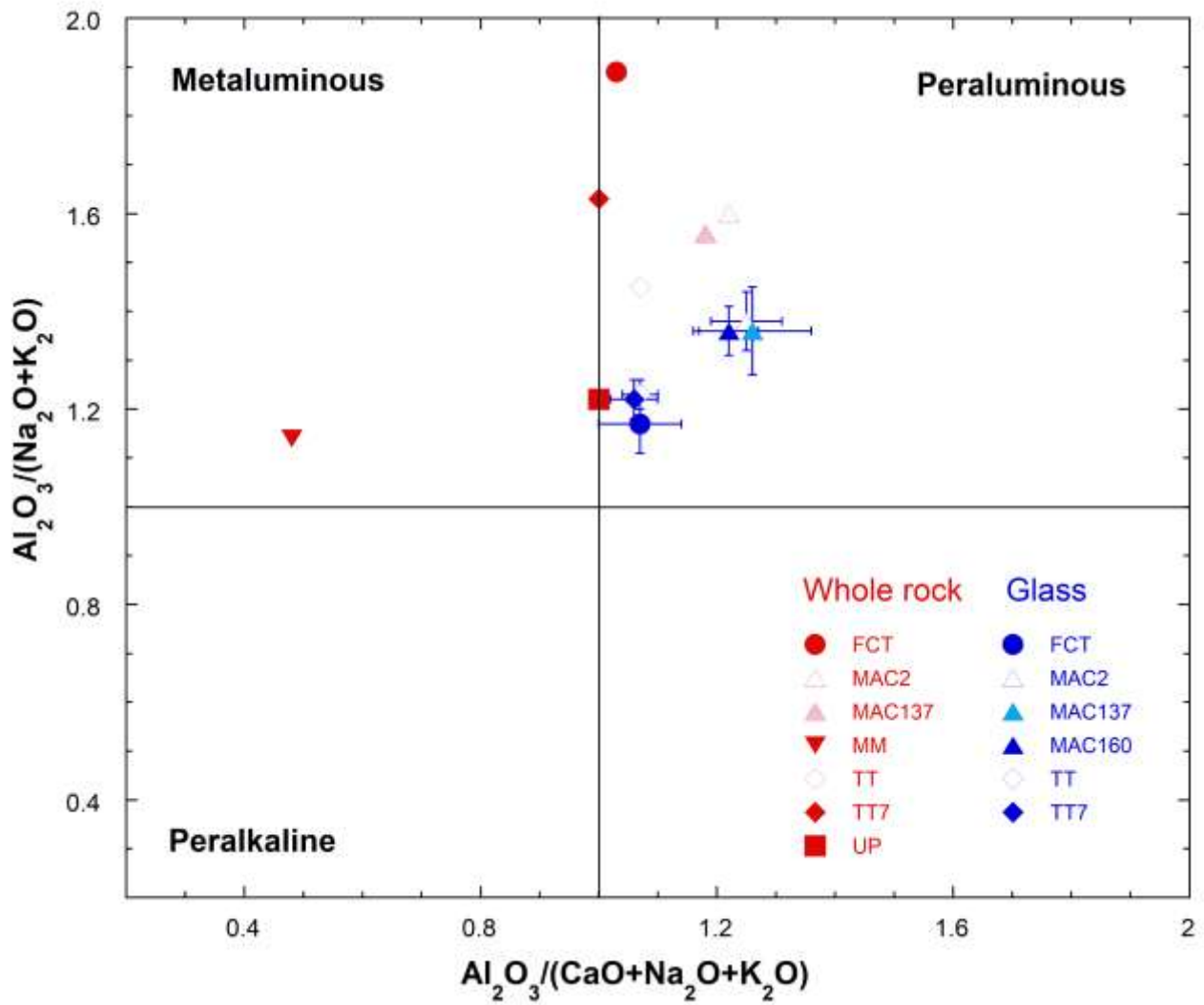
- 1484 Walsh, A., Payne, D. J., Egde, R. G., & Watson, G. W. (2011). Stereochemistry of post-transition metal oxides:  
1485 Revision of the classical lone pair model. *Chemical Society Reviews*, 40(9), 4455–4463.
- 1486 Wang, H., Wang, L., & Seetharaman, S. (2016). Determination of Vanadium Oxidation States in CaO-MgO-  
1487 Al<sub>2</sub>O<sub>3</sub>-SiO<sub>2</sub>-VO<sub>x</sub> System by K Edge XANES Method. *Steel Research International*, 87(2), 199–209.
- 1488 Watson, E. B., & Green, T. H. (1981). Apatite/liquid partition coefficients for the rare earth elements and  
1489 strontium. *Earth and Planetary Science Letters*, 56, 405–421.
- 1490 Webster, J. D., & Piccoli, P. M. (2015). Magmatic apatite: A powerful, yet deceptive, mineral. *Elements*, 11(3),  
1491 177–182.
- 1492 Wei, C., Xiong, X., Wang, J., Huang, F., & Gao, M. (2024a). Partitioning of tin between mafic minerals, Fe-Ti  
1493 oxides and silicate melts: Implications for tin enrichment in magmatic processes. *Geochimica et  
1494 Cosmochimica Acta*, 372, 81–100.
- 1495 Wei, C., Xiong, X., Wang, J., Huang, F., & Gao, M. (2024b). Partitioning of tin between mafic minerals, Fe-Ti  
1496 oxides and silicate melts: Implications for tin enrichment in magmatic processes. *Geochimica et  
1497 Cosmochimica Acta*, 372, 81–100.
- 1498 Were, P., & Keppler, H. (2021). Trace element fractionation between biotite, allanite, and granitic melt.  
1499 *Contributions to Mineralogy and Petrology*, 176(9).
- 1500 Westrenen van, W., & Draper, D. S. (2007). Quantifying garnet-melt trace element partitioning using lattice-  
1501 strain theory: New crystal-chemical and thermodynamic constraints. *Contributions to Mineralogy and  
1502 Petrology*, 154(6), 717–730.
- 1503 Whitney, D. L., & Evans, B. W. (2010). Abbreviations for names of rock-forming minerals. *American  
1504 Mineralogist*, 95(1), 185–187.
- 1505 Whitney, J. A., & Stormer, J. C. (1985). Mineralogy, Petrology, and Magmatic Conditions from the Fish Canyon  
1506 Tuff, Central San Juan Volcanic Field, Colorado. *Journal of Petrology*, 26(3), 726–762.
- 1507 Wood, B. J., & Blundy, J. D. (2013). Trace Element Partitioning: The Influences of Ionic Radius, Cation Charge,  
1508 Pressure, and Temperature. In K. K. Turekian & Holland, H. D. (Eds.), *Treatise on Geochemistry: Second  
1509 Edition* (Vol. 3, pp. 421–448). Elsevier Inc.
- 1510 Young, E. J., Myers, A. T., Munson, E. L., & Conklin, N. M. (1969). Mineralogy and geochemistry of fluorapatite  
1511 from Cerro de Mercado, Durango, Mexico. *U.S. Geological Survey Paper*, 650D, 84–93.
- 1512 Zajacz, Z., & Halter, W. (2007). LA-ICPMS analyses of silicate melt inclusions in co-precipitated minerals:  
1513 Quantification, data analysis and mineral/melt partitioning. *Geochimica et Cosmochimica Acta*, 71(4),  
1514 1021–1040.
- 1515 Zhan, Q. Y., Zhu, D. C., Weinberg, R. F., Wang, Q., Xie, J. C., Zhang, L. L., & Zhao, Z. D. (2022). Cumulate  
1516 granites: A perspective from new apatite MgO partition coefficients. *Geology*, 50(6), 681–685.
- 1517
- 1518



1520

1521 Figure 1.

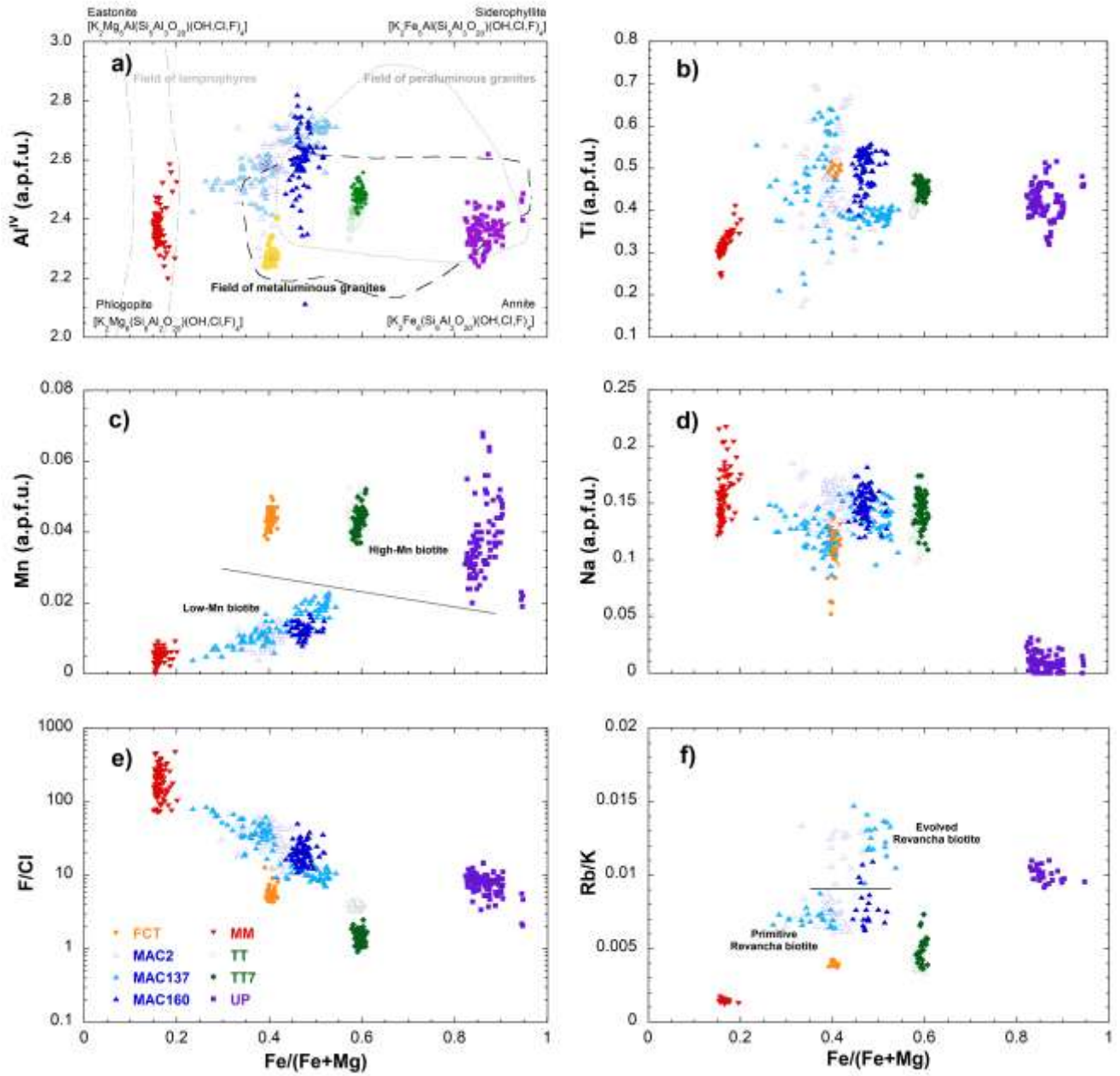
1522



1523

1524 **Figure 2.**

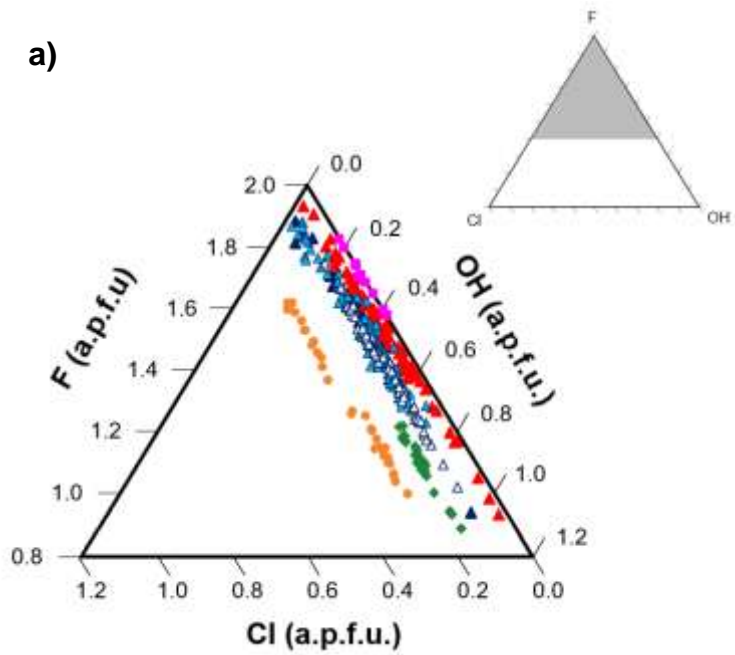
1525



1526

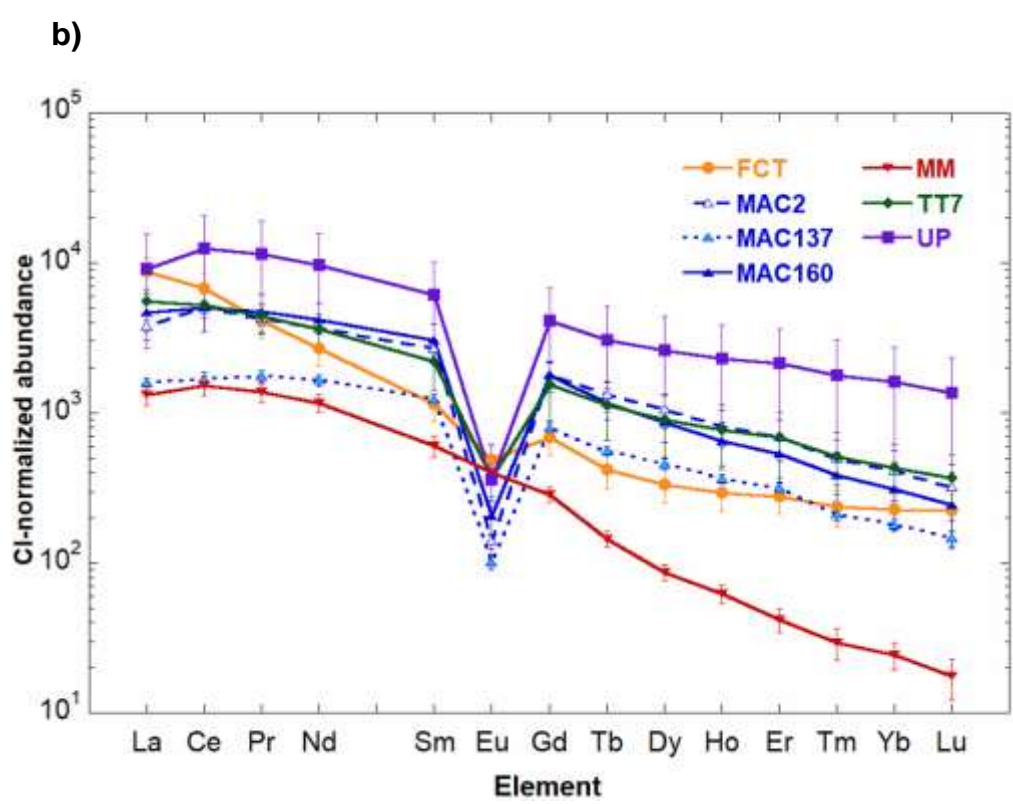
1527 **Figure 3.**

1528



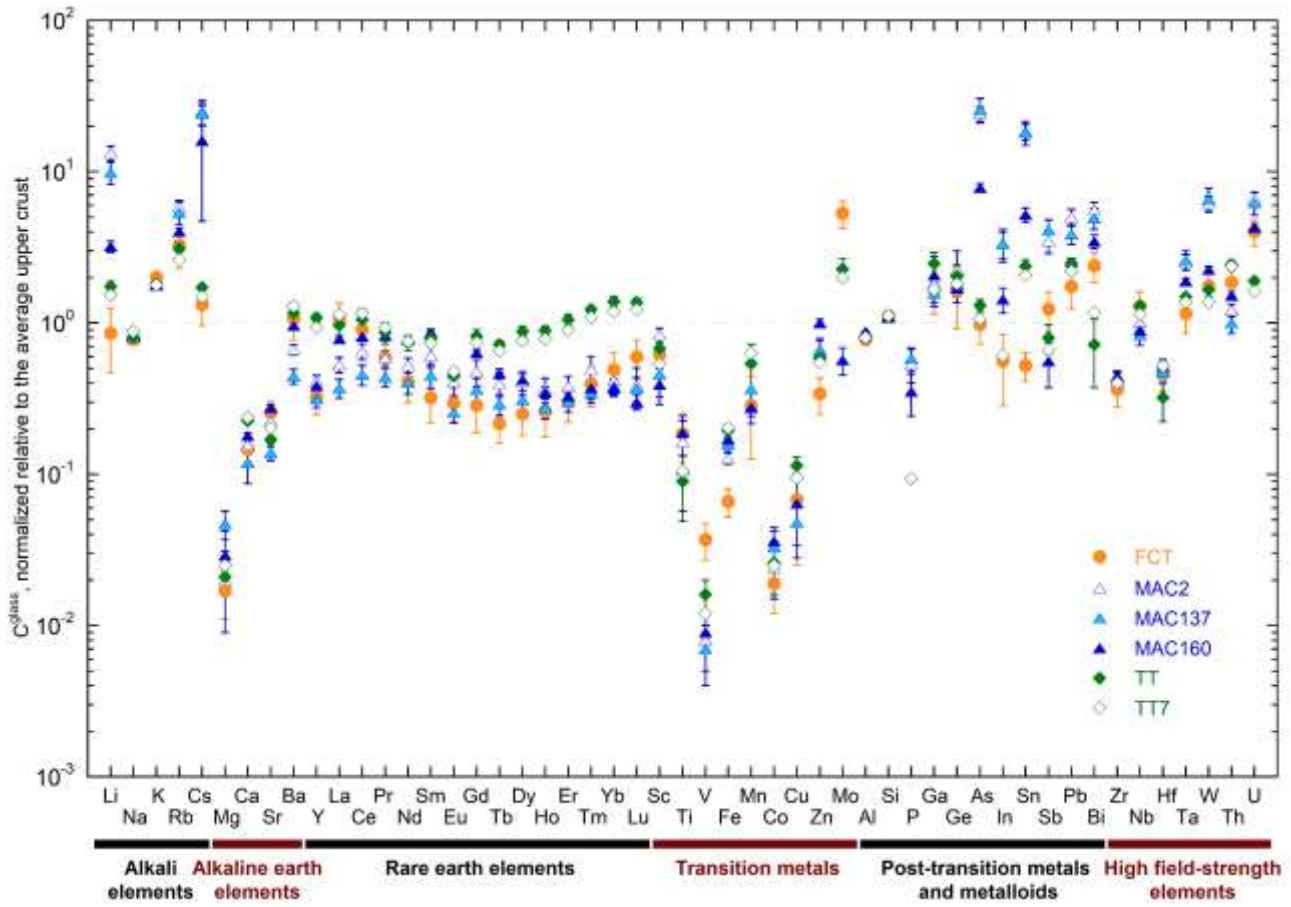
1529

1530



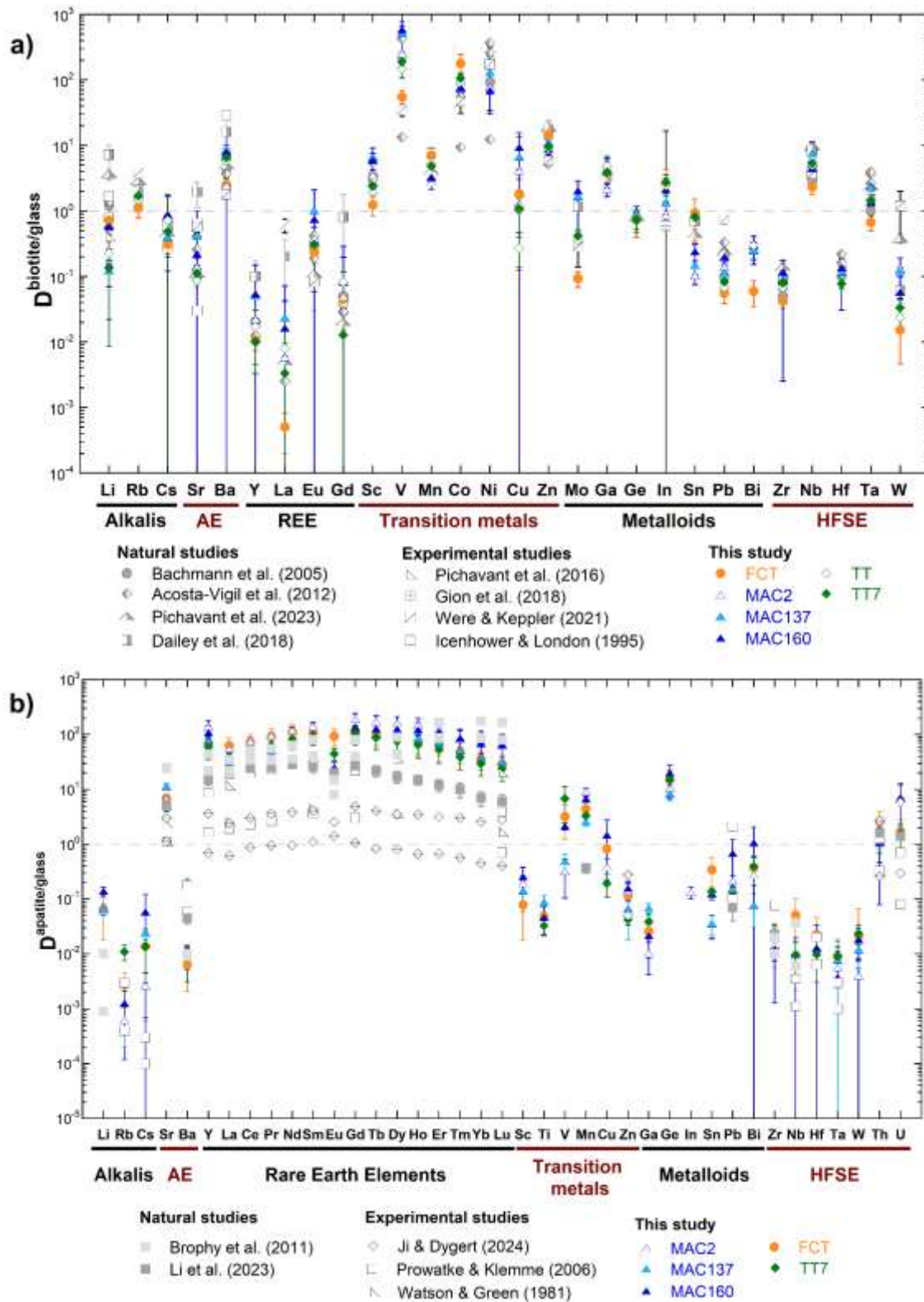
1531

1532 **Figure 4.**



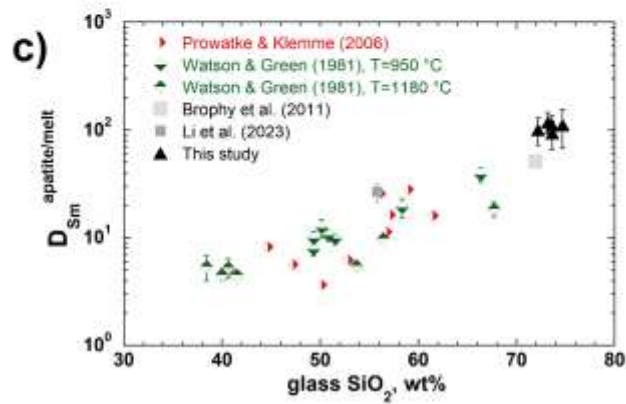
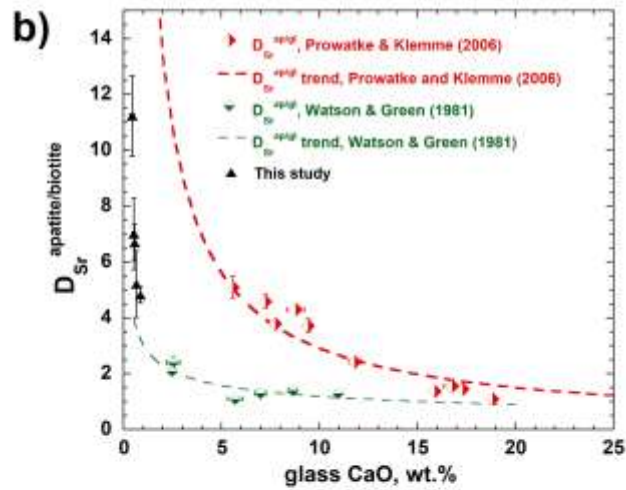
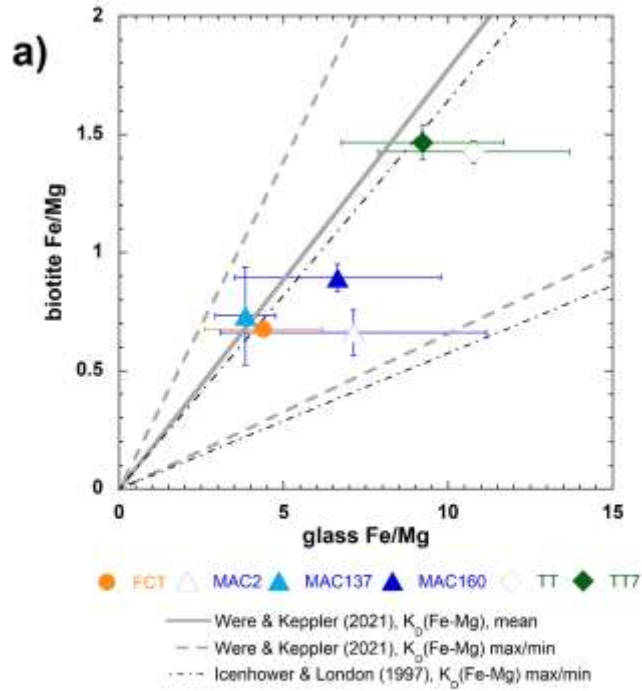
1533  
1534

Figure 5.



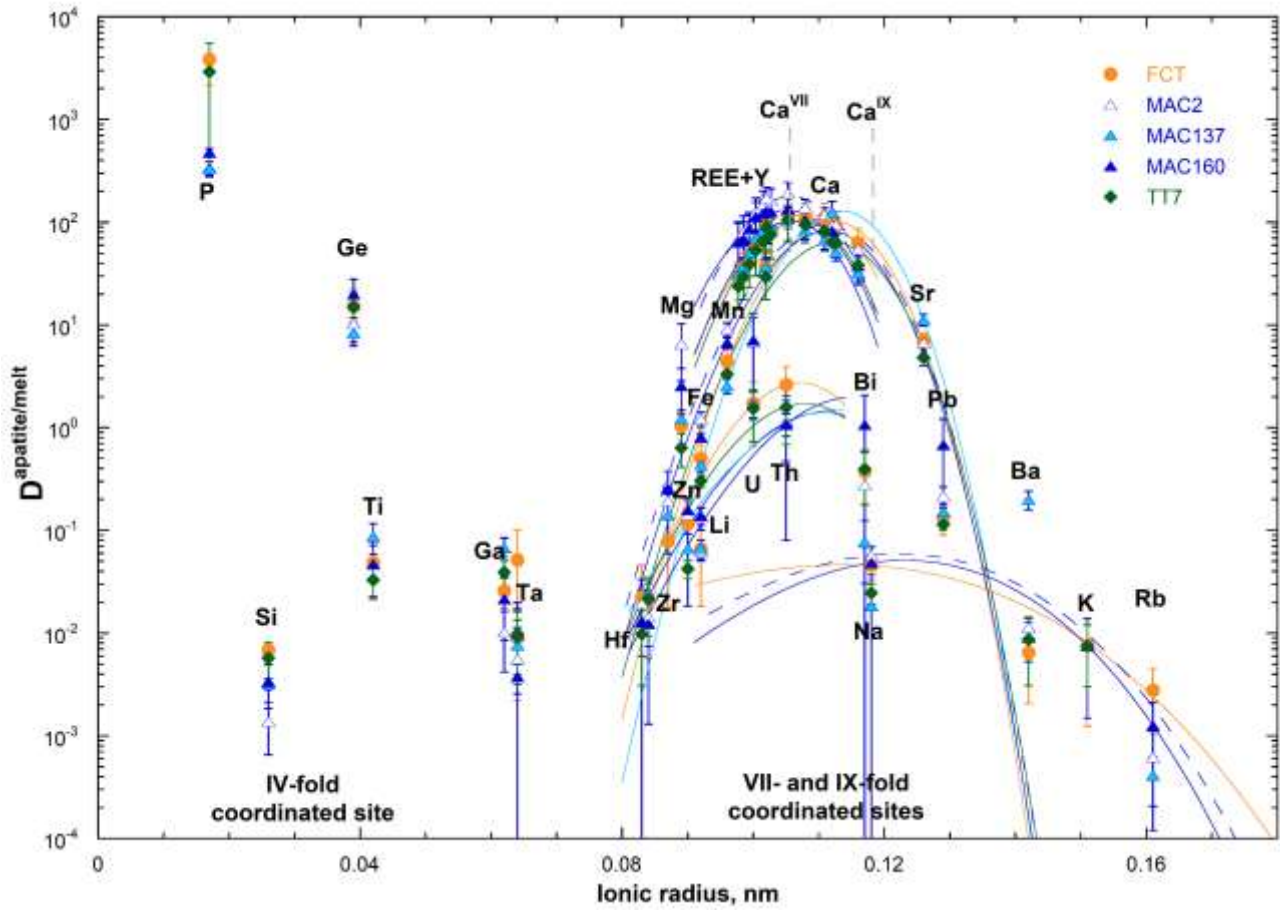
1535

1536 **Figure 6.**



1537

1538 **Figure 7.**

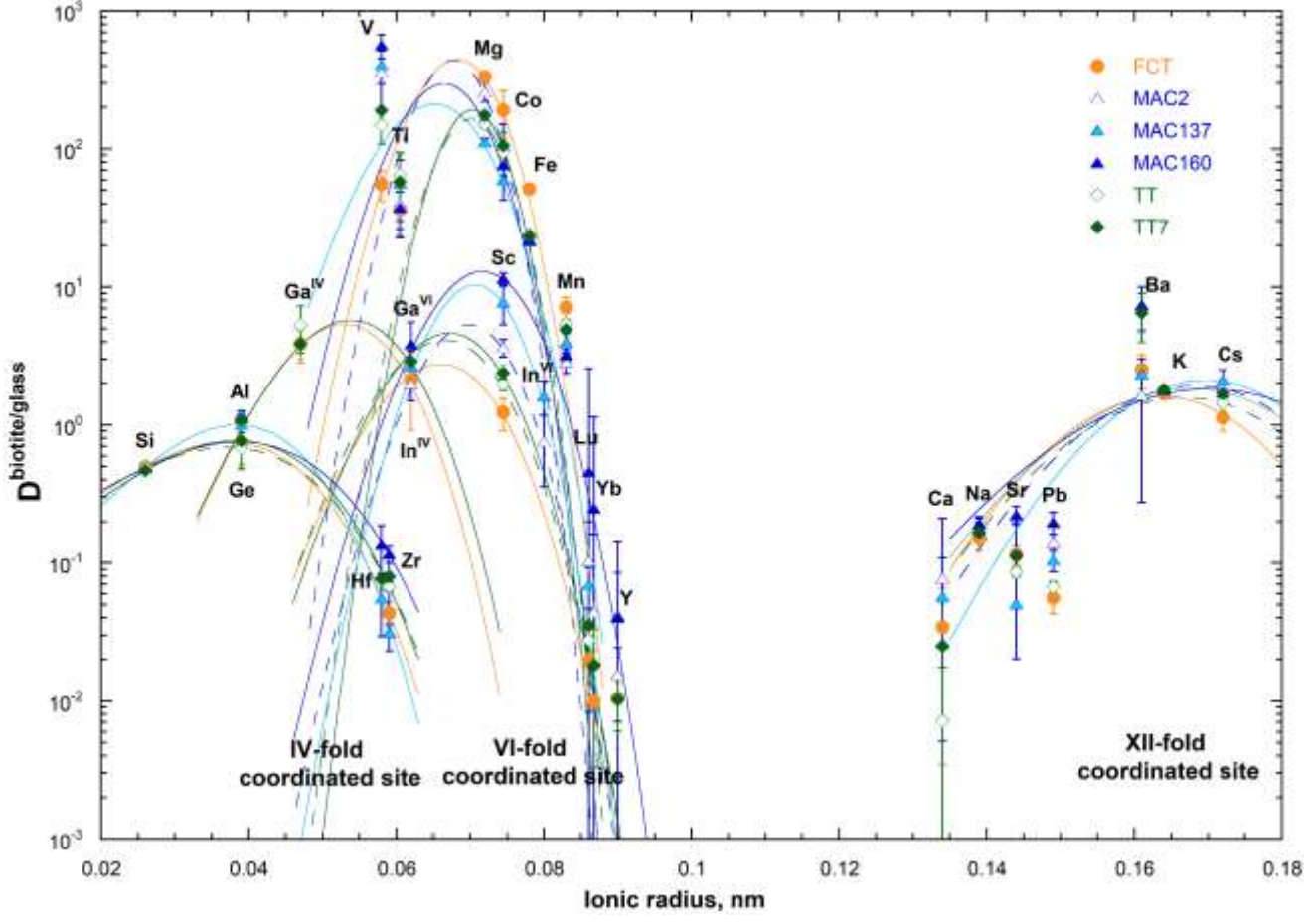


1539

1540 **Figure 8.**

1541

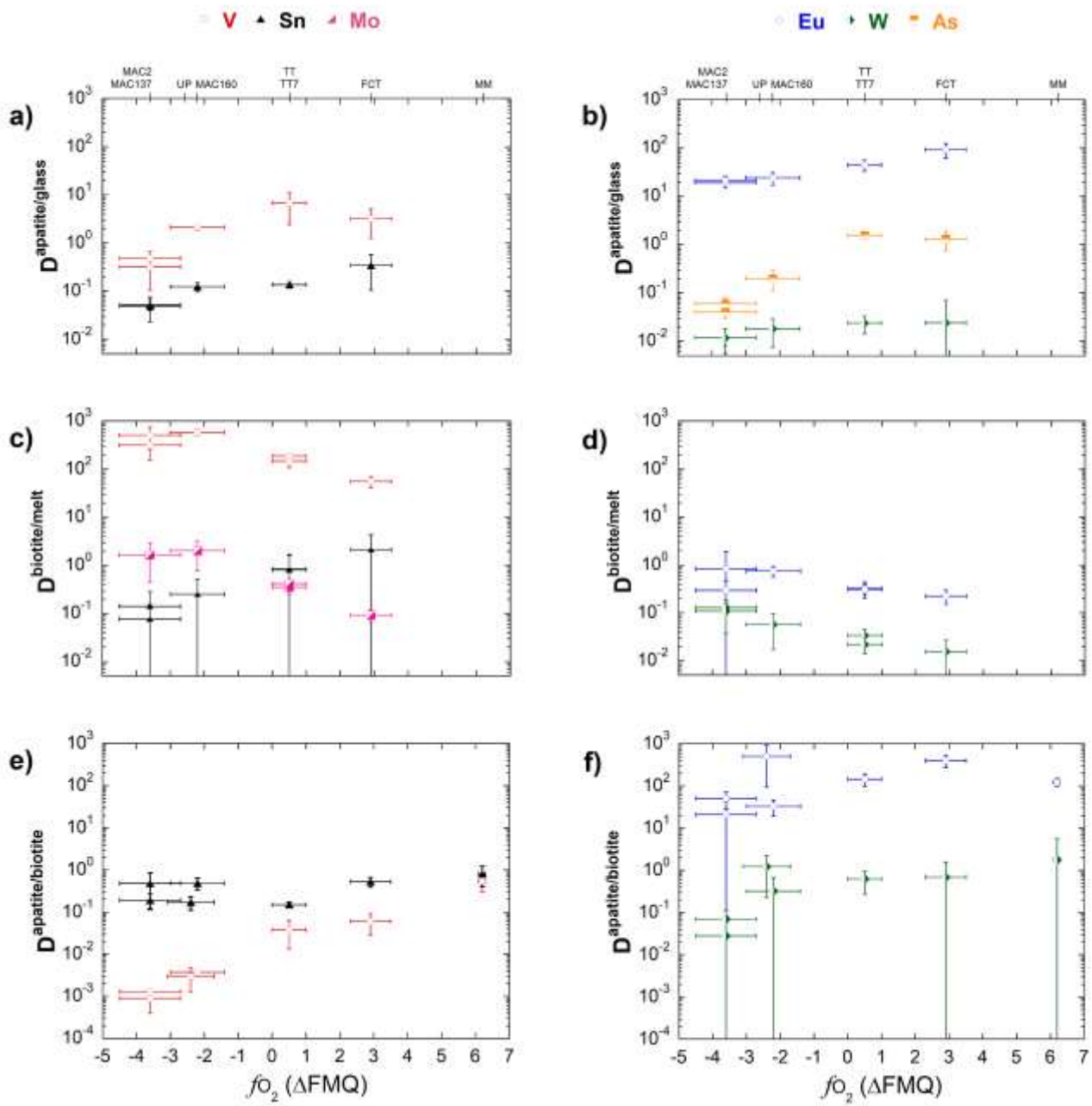
1542



1543

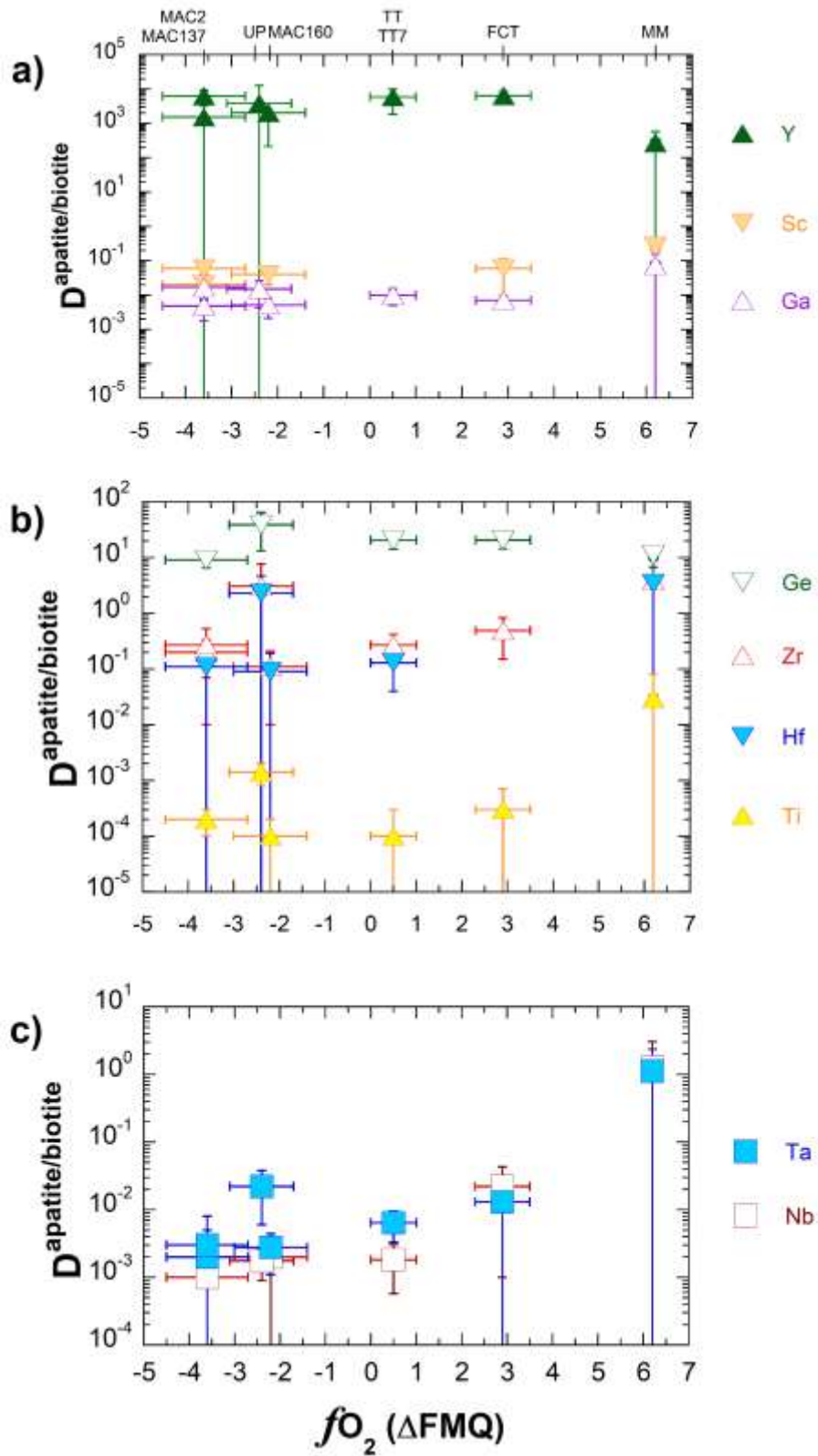
1544 **Figure 9.**

1545



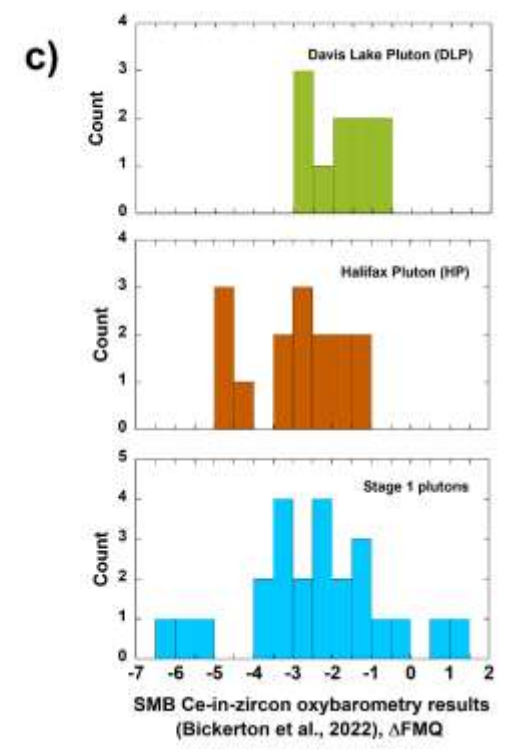
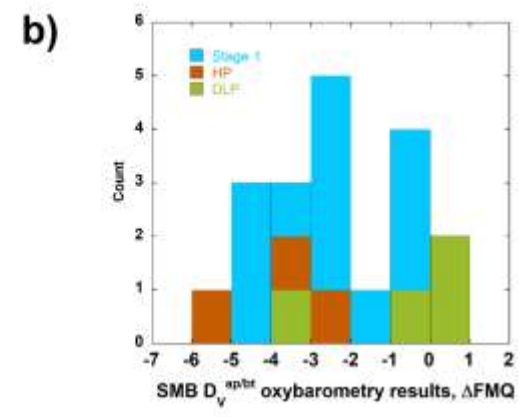
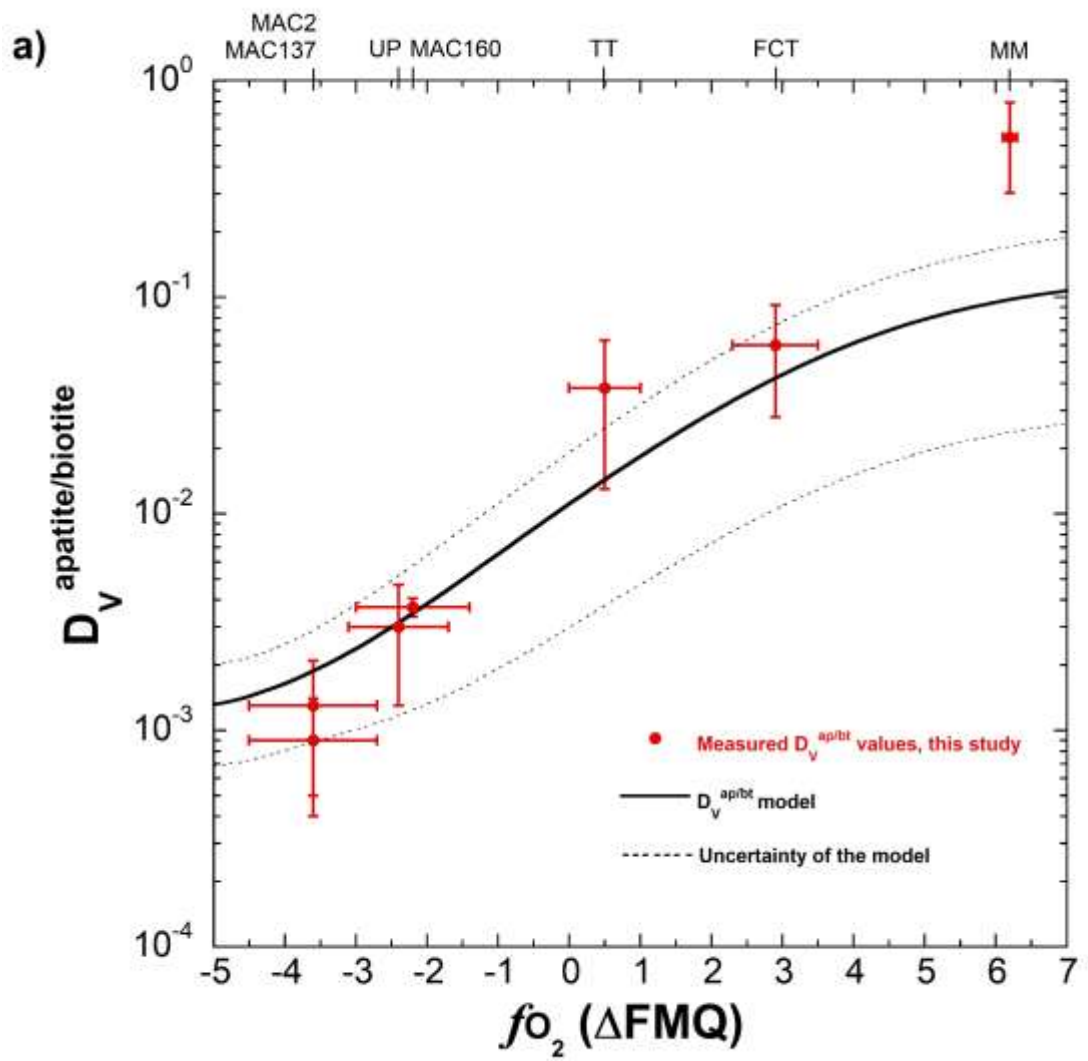
1546

1547 **Figure 10.**

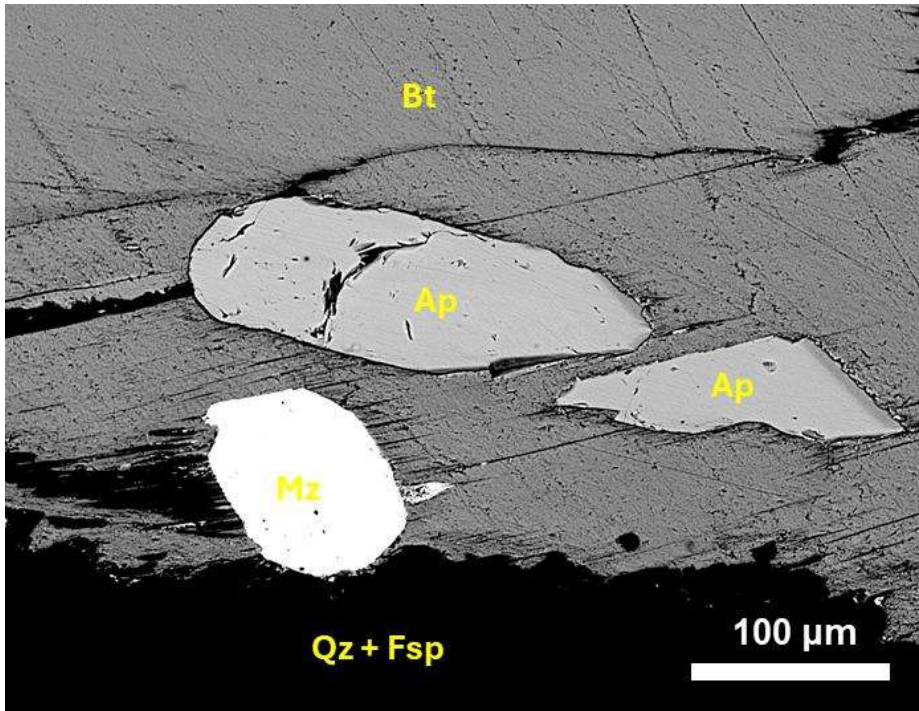


1548

1549 **Figure 11.**



1550  
1551 **Figure 12.**



1552

1553 **Figure 13.**

1554 **Tables**

1555 **Table 1.** Summary of the analysed samples. Sources of the compiled information and methodology:  
 1556 Carmichael et al. (1996) – **1**, Chesner (1998) – **2**, Chesner (2012) – **3**, Emslie & Stirling (1993) – **4**,  
 1557 Johnson & Rutherford (1989) – **5**, Kress & Carmichael (1991) – **6**, Loucks et al. (2020) – **7**, Righter &  
 1558 Carmichael (1996) – **8**, Sandeman & Clark (2003) – **9**, Sandeman et al. (1997) – **10**, Smythe & Brenan  
 1559 (2016) – **11**, Whitney & Stormer (1985) – **12**. Oxybarometry methods: zircon Ce-U-Ti for FCT<sup>7</sup>, MAC  
 1560 (this study)<sup>7</sup>, TT<sup>7</sup>, Ce-in-zircon for UP<sup>11</sup>; melt Fe oxidation state<sup>6</sup> for MM<sup>1</sup>. All oxygen fugacity values  
 1561 here are reported relative to the fayalite-magnetite-quartz mineral redox buffer ( $\Delta\text{FMQ}$ ) defined by  
 1562 O'Neill (1987).

| Sample                        | Petrology (phase assemblage)  | SiO <sub>2</sub> (wt%)   | A/CNK                    | fO <sub>2</sub> ( $\Delta\text{FMQ}$ ) | T (°C)                  |
|-------------------------------|---|--------------------------|--------------------------|--|-------------------------|
| Fish Canyon tuff, FCT         | Dacitic ignimbrite (Pl + Gl + Afs + Qz + Hbl + Bt + Ttn + Mag + Ilm + Ap + Zrn) <sup>12</sup>     | 62.4-65.2 <sup>12</sup>  | 1.03 <sup>12</sup>       | +2.9 ± 0.6 <sup>7</sup>                | 700–760° <sup>8</sup>   |
| Revancha dyke, MAC2, MAC137   | Cordierite-biotite rhyodacite (Gl + Pl + Bt + Crd + Qz + Afs + Ap + Ilm + Mnz + Zrn) <sup>9</sup> | 67.7-67.8 <sup>9</sup>   | 1.18-1.22 <sup>9</sup>   | -3.6 ± 0.9                             | 634-693° <sup>9</sup>   |
| Cerro Esquinani stock, MAC160 | Biotite rhyodacite (Gl + Pl + Bi + Qz + Sil + Ap + Ilm + Mnz + Zrn) <sup>9</sup>                  | 66.8-71.7 <sup>10</sup>  | 1.13-1.28 <sup>10</sup>  | -2.2 ± 0.8                             | -                       |
| Mascota minette, MM           | Augite minette (Aug + Bt + Ap + Mag) <sup>1</sup>   | 48.7 <sup>1</sup>        | 0.47 <sup>1</sup>        | +6.2 ± 0.1 <sup>8</sup>                | 1080-1100° <sup>8</sup> |
| Tuk-Tuk tuff, TT, TT7         | Rhyolite (Gl + Pl + Qz + Bt + Afs + Hbl + Zr + Aln + Mag + Ilm + Mnz ± Ap) <sup>2,3</sup>         | 69.8-72.7 <sup>2,3</sup> | 1.00-1.07 <sup>2,3</sup> | +0.5 ± 0.5 <sup>8</sup>                | 701-780° <sup>3</sup>   |
| Umiakovik granite, UP         | Biotite-hornblende granite (Afs + Qz + Pl + Bt + Hbl + Ilm + Ap + Zrn + Fl) <sup>4</sup>          | 73.2 <sup>4</sup>        | 1.00 <sup>4</sup>        | -2.4 ± 0.7 <sup>11</sup>               | 725-825° <sup>4</sup>   |

1563

**Table 2.** Microanalytical conditions of EPMA and LA-ICP-MS used in this study.

| Phase   | Zircon (n=25)  | Apatite (n=319)  | Biotite (n=374)  | Glass (n=289)  |
|---|--|--|--|--|
| EPMA conditions                               | 15 kV accelerating voltage, 10 nA beam current, 10 µm spot size  |  |  | 15 kV accelerating voltage, 10 nA beam current, 10 µm spot   |
| Primary standards                             | Standards for zircon analysis were zircon (Zr), (Hf), (Y), (P)   | synthetic fluorapatite (Ca, P, F); tugtupite (Cl); garnet (Fe, Si, Al); pyrolusite (Mn); albite (Na); biotite (K, Mg); K kaersutite (Ti)   | Biotite (Fe, Al, Si, K, Mg), pyrolusite (Mn), kaersutite (Ca, Ti), albite (Na), tugtupite (Cl) and apatite (F) | BHVO-1 (Ca, Na, Mg, Al, Fe, Si); sanidine (K); rutile (Ti); chromite (Cr); pyrolusite (Mn); synthetic fluorapatite (P, F); tugtupite (Cl); barite (Ba); celestite (Sr); pyrrhotite (S) |
| Count time                                    | 20 s for all analytes, except F (90 s) and Cl (40 s) in apatite, biotite, and glass  |  |  |  |
| Secondary standards                           | Synthetic zircon   | Durango apatite  | San Carlos biotite, DJ biotite   | BIR-1 and CAM66  |
| LA-ICP-MS conditions                          | 10 Hz repetition rate, ~5 J/cm <sup>2</sup> , 15-100 µm spot size depending on the crystal size and availability of crystal-free domains in glass. 15-25 µm spot size for zircon.  |  |  |  |
| Analytes                                      | <sup>23</sup> Na, <sup>27</sup> Al, <sup>29</sup> Si, <sup>31</sup> P, <sup>43</sup> Ca, <sup>44</sup> Ca, <sup>49</sup> Ti, <sup>55</sup> Mn, <sup>56</sup> Fe, <sup>89</sup> Y, <sup>90</sup> Zr, <sup>139</sup> La, <sup>140</sup> Ce, <sup>141</sup> Pr, <sup>146</sup> Nd, <sup>147</sup> Sm, <sup>153</sup> Eu, <sup>157</sup> Gd, <sup>159</sup> Tb, <sup>163</sup> Dy, <sup>165</sup> Ho, <sup>166</sup> Er, <sup>169</sup> Tm, <sup>172</sup> Yb, <sup>175</sup> Lu, <sup>178</sup> Hf, <sup>232</sup> Th, <sup>238</sup> U | <sup>7</sup> Li, <sup>27</sup> Al, <sup>29</sup> Si, <sup>31</sup> P, <sup>43</sup> Ca, <sup>45</sup> Sc, <sup>47</sup> Ti (glass, biotite), <sup>49</sup> Ti (apatite), <sup>51</sup> V, <sup>52</sup> Cr, <sup>55</sup> Mn, <sup>57</sup> Fe, <sup>59</sup> Co, <sup>61</sup> Ni, <sup>63</sup> Cu, <sup>65</sup> Cu, <sup>66</sup> Zn, <sup>69</sup> Ga, <sup>73</sup> Ge, <sup>75</sup> As, <sup>85</sup> Rb, <sup>88</sup> Sr, <sup>89</sup> Y, <sup>90</sup> Zr, <sup>93</sup> Nb, <sup>95</sup> Mo, <sup>111</sup> Cd, <sup>113</sup> In, <sup>115</sup> In, <sup>118</sup> Sn, <sup>121</sup> Sb, <sup>133</sup> Cs, <sup>137</sup> Ba, <sup>139</sup> La, <sup>140</sup> Ce, <sup>141</sup> Pr, <sup>146</sup> Nd, <sup>147</sup> Sm, <sup>153</sup> Eu, <sup>157</sup> Gd, <sup>159</sup> Tb, <sup>163</sup> Dy, <sup>165</sup> Ho, <sup>166</sup> Er, <sup>169</sup> Tm, <sup>172</sup> Yb, <sup>175</sup> Lu, <sup>178</sup> Hf, <sup>181</sup> Ta, <sup>182</sup> W, <sup>206</sup> Pb, <sup>208</sup> Pb, <sup>209</sup> Bi, <sup>232</sup> Th, <sup>238</sup> U |  |  |
| Dwell time                                    | 10 ms (most analytes), 30 ms ( <sup>139</sup> La, <sup>141</sup> Pr)   | 10 ms (most analytes), 30 ms ( <sup>51</sup> V), 5 ms ( <sup>27</sup> Al, <sup>29</sup> Si, <sup>31</sup> P, <sup>57</sup> Fe)   |  |  |
| Primary standard                              | NIST 610 glass   |  |  |  |
| Secondary standard, internal standard isotope | Zircon 91500, <sup>90</sup> Zr   | Durango apatite, apatite nano-powder pellet (myStandards GmbH), <sup>43</sup> Ca   | DJ biotite, <sup>27</sup> Al   | BIR-1, BHVO-1, <sup>43</sup> Ca  |

1566 **Table 3.** Trace element partitioning between apatite and glass.  
 1567

|    | FCT           |            | MAC2          |            | MAC137        |            | MAC160        |            | TT7           |            |
|----|---------------|------------|---------------|------------|---------------|------------|---------------|------------|---------------|------------|
|    | Mean          | 1 $\sigma$ | Mean          | 1 $\sigma$ | Mean          | 1 $\sigma$ | Mean          | 1 $\sigma$ | Mean          | 1 $\sigma$ |
| Li | <b>0.06</b>   | 0.05       | <b>0.06</b>   | 0.01       | <b>0.07</b>   | 0.01       | <b>0.14</b>   | 0.02       | -             | -          |
| Rb | <b>0.0027</b> | 0.0016     | <b>0.0006</b> | 0.0005     | <b>0.0004</b> | 0.0002     | <b>0.0012</b> | 0.0009     | -             | -          |
| Cs | <b>0.014</b>  | 0.013      | <b>0.003</b>  | 0.002      | <b>0.024</b>  | 0.006      | <b>0.050</b>  | 0.054      | <b>0.014</b>  | 0.011      |
| Sr | <b>7.0</b>    | 1.3        | <b>6.7</b>    | 0.6        | <b>11.4</b>   | 1.5        | <b>5.3</b>    | 1.2        | <b>4.8</b>    | 0.3        |
| Ba | <b>0.006</b>  | 0.004      | <b>0.011</b>  | 0.003      | <b>0.207</b>  | 0.041      | <b>0.009</b>  | 0.004      | <b>0.009</b>  | 0.006      |
| Y  | <b>69</b>     | 22         | <b>136</b>    | 40         | <b>78</b>     | 10         | <b>110</b>    | 37         | <b>60</b>     | 25         |
| La | <b>62</b>     | 20         | <b>55</b>     | 8          | <b>33</b>     | 5          | <b>46</b>     | 16         | <b>38</b>     | 6          |
| Ce | <b>71</b>     | 25         | <b>76</b>     | 12         | <b>36</b>     | 7          | <b>61</b>     | 19         | <b>45</b>     | 8          |
| Pr | <b>90</b>     | 31         | <b>94</b>     | 15         | <b>52</b>     | 9          | <b>75</b>     | 22         | <b>63</b>     | 12         |
| Nd | <b>109</b>    | 35         | <b>119</b>    | 18         | <b>69</b>     | 12         | <b>91</b>     | 28         | <b>83</b>     | 19         |
| Sm | <b>110</b>    | 43         | <b>140</b>    | 27         | <b>86</b>     | 17         | <b>112</b>    | 31         | <b>95</b>     | 31         |
| Eu | <b>91</b>     | 29         | <b>19</b>     | 4          | <b>22</b>     | 4          | <b>25</b>     | 7          | <b>45</b>     | 11         |
| Gd | <b>118</b>    | 49         | <b>191</b>    | 51         | <b>110</b>    | 21         | <b>140</b>    | 33         | <b>106</b>    | 42         |
| Tb | <b>98</b>     | 35         | <b>172</b>    | 47         | <b>99</b>     | 17         | <b>131</b>    | 31         | <b>89</b>     | 36         |
| Dy | <b>82</b>     | 30         | <b>164</b>    | 50         | <b>94</b>     | 16         | <b>129</b>    | 36         | <b>75</b>     | 31         |
| Ho | <b>72</b>     | 29         | <b>148</b>    | 50         | <b>87</b>     | 15         | <b>123</b>    | 41         | <b>65</b>     | 28         |
| Er | <b>63</b>     | 22         | <b>126</b>    | 44         | <b>73</b>     | 12         | <b>114</b>    | 43         | <b>53</b>     | 23         |
| Tm | <b>48</b>     | 19         | <b>83</b>     | 33         | <b>51</b>     | 9          | <b>86</b>     | 39         | <b>39</b>     | 16         |
| Yb | <b>36</b>     | 14         | <b>80</b>     | 34         | <b>38</b>     | 6          | <b>68</b>     | 33         | <b>29</b>     | 12         |
| Lu | <b>29</b>     | 12         | <b>66</b>     | 33         | <b>32</b>     | 7          | <b>65</b>     | 33         | <b>24</b>     | 10         |
| Sc | <b>0.08</b>   | 0.06       | <b>0.20</b>   | 0.07       | <b>0.14</b>   | 0.09       | <b>0.50</b>   | 0.20       | -             | -          |
| Ti | <b>0.05</b>   | 0.03       | -             | -          | <b>0.09</b>   | 0.03       | <b>0.05</b>   | 0.02       | <b>0.03</b>   | 0.01       |
| V  | <b>3.2</b>    | 2.0        | <b>0.4</b>    | 0.3        | <b>0.5</b>    | 0.2        | <b>2.1</b>    | 1.4        | <b>6.8</b>    | 4.4        |
| Mn | <b>4.4</b>    | 1.4        | <b>9.0</b>    | 1.3        | <b>2.6</b>    | 0.4        | <b>6.7</b>    | 0.7        | <b>3.3</b>    | 0.2        |
| Cu | <b>0.83</b>   | 0.64       | <b>0.39</b>   | 0.16       | -             | -          | <b>1.47</b>   | 1.29       | <b>0.19</b>   | 0.09       |
| Zn | <b>0.11</b>   | 0.09       | <b>0.15</b>   | 0.05       | <b>0.04</b>   | 0.01       | <b>0.15</b>   | 0.04       | <b>0.04</b>   | 0.01       |
| Ga | <b>0.025</b>  | 0.007      | <b>0.011</b>  | 0.002      | <b>0.069</b>  | 0.018      | <b>0.020</b>  | 0.007      | <b>0.039</b>  | 0.016      |
| Ge | <b>15</b>     | 7          | <b>12</b>     | 5          | <b>9</b>      | 2          | <b>23</b>     | 9          | <b>15</b>     | 6          |
| As | <b>1.31</b>   | 0.56       | <b>0.06</b>   | 0.02       | <b>0.04</b>   | 0.01       | <b>0.21</b>   | 0.08       | <b>1.58</b>   | 0.56       |
| In | -             | -          | <b>0.13</b>   | 0.03       | -             | -          | -             | -          | -             | -          |
| Sn | <b>0.34</b>   | 0.22       | <b>0.04</b>   | 0.02       | <b>0.04</b>   | 0.01       | <b>0.12</b>   | 0.03       | <b>0.14</b>   | 0.02       |
| Pb | <b>0.14</b>   | 0.05       | <b>0.20</b>   | 0.04       | <b>0.15</b>   | 0.03       | <b>0.69</b>   | 0.55       | <b>0.12</b>   | 0.02       |
| Bi | <b>0.38</b>   | 0.19       | <b>0.27</b>   | 0.29       | <b>0.08</b>   | 0.05       | <b>1.10</b>   | 0.95       | <b>0.39</b>   | 0.22       |
| Zr | <b>0.020</b>  | 0.015      | <b>0.014</b>  | 0.007      | <b>0.025</b>  | 0.006      | <b>0.012</b>  | 0.011      | <b>0.021</b>  | 0.012      |
| Nb | <b>0.052</b>  | 0.049      | <b>0.010</b>  | 0.010      | -             | -          | <b>0.004</b>  | -          | <b>0.010</b>  | 0.007      |
| Hf | <b>0.022</b>  | 0.024      | <b>0.018</b>  | 0.013      | <b>0.014</b>  | 0.015      | <b>0.017</b>  | 0.012      | <b>0.010</b>  | 0.007      |
| Ta | <b>0.0090</b> | 0.0097     | <b>0.0053</b> | 0.0052     | <b>0.0085</b> | 0.0105     | <b>0.0037</b> | 0.0012     | <b>0.0092</b> | 0.0042     |
| W  | <b>0.021</b>  | 0.046      | <b>0.004</b>  | 0.004      | <b>0.011</b>  | 0.007      | <b>0.020</b>  | 0.012      | <b>0.024</b>  | 0.009      |
| Th | <b>2.6</b>    | 1.3        | <b>1.2</b>    | 0.7        | <b>1.1</b>    | 0.3        | <b>4.7</b>    | 7.1        | <b>1.6</b>    | 0.9        |
| U  | <b>1.7</b>    | 1.1        | <b>6.8</b>    | 4.9        | <b>1.7</b>    | 0.5        | <b>7.5</b>    | 5.8        | <b>1.5</b>    | 0.8        |

1568

1569 **Table 4.** Trace element partitioning between biotite and glass.  
 1570

|    | FCT           |            | MAC2          |            | MAC137        |            | MAC160        |            | TT            |            | TT7           |            |
|----|---------------|------------|---------------|------------|---------------|------------|---------------|------------|---------------|------------|---------------|------------|
|    | Mean          | 1 $\sigma$ | Mean          | 1 $\sigma$ | Mean          | 1 $\sigma$ | Mean          | 1 $\sigma$ | Mean          | 1 $\sigma$ | Mean          | 1 $\sigma$ |
| Li | <b>0.70</b>   | 0.35       | <b>0.15</b>   | 0.05       | <b>0.12</b>   | 0.05       | <b>0.57</b>   | 0.18       | <b>0.23</b>   | 0.21       | <b>0.14</b>   | 0.13       |
| Rb | <b>1.1</b>    | 0.3        | <b>1.6</b>    | 0.2        | <b>1.8</b>    | 0.6        | <b>1.6</b>    | 0.2        | <b>1.5</b>    | 0.2        | <b>1.7</b>    | 0.3        |
| Cs | <b>0.31</b>   | 0.09       | <b>0.40</b>   | 0.12       | <b>0.40</b>   | 0.20       | <b>0.89</b>   | 0.77       | <b>0.72</b>   | 1.06       | <b>0.48</b>   | 0.21       |
| Sr | <b>0.11</b>   | 0.02       | <b>0.14</b>   | 0.07       | <b>0.42</b>   | 0.57       | <b>0.22</b>   | 0.03       | <b>0.09</b>   | 0.01       | <b>0.11</b>   | 0.01       |
| Ba | <b>2.5</b>    | 0.7        | <b>2.4</b>    | 1.8        | <b>8.4</b>    | 10.0       | <b>7.9</b>    | 2.1        | <b>5.8</b>    | 2.6        | <b>6.5</b>    | 1.8        |
| Y  | <b>0.0102</b> | 0.0031     | <b>0.0221</b> | 0.0087     | <b>0.0497</b> | 0.0997     | <b>0.0536</b> | 0.0442     | <b>0.0172</b> | 0.0139     | <b>0.0102</b> | 0.0057     |
| La | <b>0.0004</b> | 0.0003     | <b>0.0058</b> | 0.0041     | <b>0.0234</b> | 0.0480     | <b>0.0162</b> | 0.0261     | <b>0.0079</b> | 0.0144     | <b>0.0030</b> | 0.0062     |
| Eu | <b>0.220</b>  | 0.067      | <b>0.379</b>  | 0.173      | <b>1.020</b>  | 1.073      | <b>0.743</b>  | 0.179      | <b>0.310</b>  | 0.116      | <b>0.310</b>  | 0.077      |
| Gd | <b>0.045</b>  | 0.030      | <b>0.050</b>  | 0.031      | <b>0.081</b>  | 0.205      | <b>0.082</b>  | 0.113      | <b>0.082</b>  | 0.036      | <b>0.014</b>  | 0.017      |
| Sc | <b>1.2</b>    | 0.3        | <b>3.5</b>    | 0.7        | <b>6.7</b>    | 2.5        | <b>11.4</b>   | 1.2        | <b>1.9</b>    | 0.2        | <b>2.4</b>    | 0.3        |
| V  | <b>54</b>     | 14         | <b>319</b>    | 161        | <b>515</b>    | 255        | <b>586</b>    | 85         | <b>146</b>    | 39         | <b>190</b>    | 25         |
| Mn | <b>7.1</b>    | 2.1        | <b>2.7</b>    | 0.6        | <b>3.3</b>    | 1.1        | <b>3.2</b>    | 0.3        | <b>5.3</b>    | 0.4        | <b>4.9</b>    | 0.6        |
| Co | <b>177</b>    | 66         | <b>102</b>    | 41         | <b>73</b>     | 28         | <b>77</b>     | 19         | <b>94</b>     | 35         | <b>106</b>    | 19         |
| Ni | -             | -          | <b>77</b>     | 31         | <b>130</b>    | 96         | <b>68</b>     | 7          | -             | -          | -             | -          |
| Cu | <b>3.6</b>    | 4.5        | -             | -          | <b>7.7</b>    | 6.9        | <b>10.3</b>   | 6.6        | <b>0.8</b>    | 0.2        | <b>1.5</b>    | 0.6        |
| Zn | <b>14.3</b>   | 3.1        | <b>8.8</b>    | 1.9        | <b>11.1</b>   | 3.9        | <b>8.8</b>    | 1.1        | <b>9.0</b>    | 0.8        | <b>9.6</b>    | 1.4        |
| Mo | <b>0.09</b>   | 0.03       | -             | -          | <b>1.66</b>   | 1.21       | <b>2.03</b>   | -          | <b>0.35</b>   | 0.10       | <b>0.42</b>   | 0.09       |
| Ga | <b>3.7</b>    | 1.2        | <b>2.1</b>    | 0.5        | <b>4.0</b>    | 2.3        | <b>4.2</b>    | 1.6        | <b>4.8</b>    | 2.1        | <b>3.9</b>    | 0.9        |
| Ge | <b>0.7</b>    | 0.3        | -             | -          | <b>0.9</b>    | 0.3        | -             | -          | <b>0.7</b>    | 0.2        | <b>0.8</b>    | 0.3        |
| In | <b>2.4</b>    | 1.5        | <b>0.9</b>    | 0.4        | <b>1.3</b>    | 0.6        | <b>2.2</b>    | 0.8        | -             | -          | <b>2.9</b>    | 1.0        |
| Sn | <b>0.93</b>   | 0.61       | <b>0.10</b>   | 0.05       | <b>0.15</b>   | 0.07       | <b>0.24</b>   | 0.07       | <b>0.80</b>   | 0.10       | <b>0.84</b>   | 0.20       |
| Pb | <b>0.06</b>   | 0.02       | <b>0.14</b>   | 0.04       | <b>0.11</b>   | 0.03       | <b>0.21</b>   | 0.03       | <b>0.07</b>   | 0.01       | -             | -          |
| Bi | -             | -          | <b>0.26</b>   | 0.08       | <b>0.24</b>   | 0.09       | <b>0.29</b>   | 0.11       | <b>0.30</b>   | 0.14       | -             | -          |
| Zr | <b>0.04</b>   | 0.01       | <b>0.07</b>   | 0.03       | <b>0.09</b>   | 0.09       | <b>0.12</b>   | 0.02       | <b>0.07</b>   | 0.01       | <b>0.08</b>   | 0.01       |
| Nb | <b>2.3</b>    | 0.6        | <b>6.4</b>    | 1.8        | <b>7.4</b>    | 3.8        | <b>4.4</b>    | 1.6        | <b>5.0</b>    | 0.7        | <b>5.4</b>    | 0.7        |
| Hf | -             | -          | -             | -          | <b>0.12</b>   | 0.08       | <b>0.13</b>   | 0.05       | -             | -          | <b>0.08</b>   | 0.01       |
| Ta | <b>0.7</b>    | 0.2        | <b>2.3</b>    | 0.9        | <b>2.3</b>    | 1.3        | <b>1.4</b>    | 0.7        | <b>1.5</b>    | 0.3        | <b>1.4</b>    | 0.3        |
| W  | <b>0.02</b>   | 0.01       | <b>0.13</b>   | 0.03       | <b>0.12</b>   | 0.07       | <b>0.06</b>   | 0.04       | <b>0.02</b>   | 0.01       | <b>0.03</b>   | 0.01       |

1571

1572 **Table 5.** Trace element partitioning between apatite and biotite.

|    | FCT    |            | MAC2   |            | MAC137 |            | MAC160 |            | MM     |            | TT7    |            | UP     |            |
|----|--------|------------|--------|------------|--------|------------|--------|------------|--------|------------|--------|------------|--------|------------|
|    | Mean   | 1 $\sigma$ | Mean   | 1 $\sigma$ | Mean   | 1 $\sigma$ | Mean   | 1 $\sigma$ | Mean   | 1 $\sigma$ | Mean   | 1 $\sigma$ | Mean   | 1 $\sigma$ |
| Li | 0.091  | 0.057      | 0.409  | 0.136      | 0.560  | 0.232      | 0.241  | 0.083      | 0.405  | 0.370      | -      | -          | 0.003  | 0.002      |
| Rb | 0.0025 | 0.0014     | 0.0004 | 0.0003     | 0.0002 | 0.0001     | 0.0007 | 0.0005     | 0.1300 | 0.1416     | -      | -          | 0.0009 | 0.0005     |
| Cs | 0.045  | 0.041      | 0.007  | 0.005      | 0.061  | 0.031      | 0.056  | 0.054      | 0.330  | 0.236      | 0.028  | 0.025      | 0.014  | 0.004      |
| Sr | 62     | 5          | 48     | 25         | 27     | 37         | 24     | 6          | 35     | 11         | 43     | 4          | 127    | 58         |
| Ba | 0.0026 | 0.0017     | 0.0047 | 0.0036     | 0.0247 | 0.0298     | 0.0012 | 0.0006     | 0.0462 | 0.0681     | 0.0013 | 0.0009     | 0.0013 | 0.0018     |
| Co | 0.009  | 0.009      | 0.020  | 0.005      | 0.008  | 0.003      | 0.008  | 0.001      | 0.037  | 0.036      | 0.009  | -          | 0.015  | 0.024      |
| Ni | 0.037  | 0.020      | 0.008  | 0.002      | 0.016  | 0.011      | 0.008  | -          | 0.004  | 0.004      | -      | -          | 0.132  | 0.060      |
| Zn | 0.008  | 0.006      | 0.017  | 0.005      | 0.004  | 0.001      | 0.017  | 0.005      | 0.279  | 0.252      | 0.004  | 0.001      | 0.003  | 0.002      |
| Pb | 2.4    | 0.6        | 1.4    | 0.4        | 1.3    | 0.4        | 3.3    | 2.7        | 4.7    | 5.7        | -      | -          | 9.2    | 10.2       |
| Y  | 6748   | 2108       | 6164   | 2900       | 1574   | 3153       | 2060   | 1830       | 273    | 302        | 5863   | 4002       | 3821   | 5558       |
| La | 143818 | 95569      | 9432   | 6549       | 1404   | 2880       | 2802   | 4608       | 247    | 501        | 12731  | 26130      | 190    | 305        |
| Gd | 2613   | 1634       | 3832   | 2390       | 1353   | 3406       | 1700   | 2363       | 633    | 1096       | 7634   | 9909       | 1847   | 2970       |
| Sc | 0.064  | 0.045      | 0.056  | 0.022      | 0.021  | 0.013      | 0.044  | 0.018      | 0.256  | 0.175      | -      | -          | 0.062  | 0.045      |
| Ga | 0.007  | 0.001      | 0.005  | 0.001      | 0.017  | 0.010      | 0.005  | 0.001      | 0.073  | 0.085      | 0.010  | 0.005      | 0.024  | 0.011      |
| In | -      | -          | 0.16   | 0.05       | -      | -          | -      | -          | -      | -          | -      | -          | -      | -          |
| Bi | -      | -          | 1.0    | 1.1        | 0.3    | 0.2        | 3.8    | 3.5        | -      | -          | -      | -          | -      | -          |
| Ge | 21.9   | 6.8        | -      | -          | 9.6    | 2.5        | -      | -          | -      | -          | 20.0   | 6.1        | -      | -          |
| Zr | 0.49   | 0.34       | 0.21   | 0.13       | 0.28   | 0.27       | 0.11   | 0.09       | 3.83   | 6.31       | 0.27   | 0.15       | 3.08   | 4.58       |
| Hf | -      | -          | -      | -          | 0.12   | 0.15       | 0.13   | 0.10       | 3.44   | 5.37       | 0.13   | 0.09       | 2.54   | 2.70       |
| Th | 3272   | 4412       | 180    | 219        | 100    | 254        | 415    | 952        | 76     | 232        | 5706   | 11921      | 2675   | 6427       |
| Si | -      | -          | -      | -          | 0.005  | 0.001      | 0.008  | 0.002      | 0.093  | 0.131      | 0.021  | 0.015      |        |            |
| Ti | -      | -          | -      | -          | 0.0018 | 0.0007     | 0.0014 | 0.0007     | 0.0338 | 0.0577     | 0.0007 | 0.0002     |        |            |
| Nb | 0.022  | 0.021      | 0.002  | 0.002      | -      | -          | 0.001  | -          | 1.288  | 1.772      | 0.002  | 0.001      | 0.002  | 0.001      |
| Ta | 0.013  | 0.014      | 0.002  | 0.002      | 0.004  | 0.005      | 0.003  | 0.002      | 1.118  | 1.249      | 0.006  | 0.003      | 0.022  | 0.016      |
| P  | -      | -          | -      | -          | 2513   | 1986       | 2344   | 2586       | 2804   | 2521       | -      | -          |        |            |
| Eu | 415    | 135        | 51     | 22         | 22     | 23         | 34     | 12         | 123    | 43         | 144    | 48         | 506    | 412        |
| V  | 0.0589 | 0.0326     | 0.0012 | 0.0007     | 0.0010 | 0.0005     | 0.0036 | 0.0024     | 0.5468 | 0.2493     | 0.0358 | 0.0226     | 0.0029 | 0.0019     |
| Mn | 0.62   | 0.08       | 3.32   | 0.62       | 0.78   | 0.26       | 2.08   | 0.26       | 1.08   | 0.36       | 0.68   | 0.07       | -      | -          |
| Cu | 0.46   | 0.38       | 0.09   | 0.10       | -      | -          | 0.16   | 0.12       | 0.36   | 0.31       | 0.18   | 0.12       | -      | -          |
| Sn | 0.37   | 0.10       | 0.35   | 0.22       | 0.26   | 0.15       | 0.52   | 0.17       | 0.81   | 0.41       | 0.16   | 0.04       | 0.18   | 0.06       |
| W  | 1.41   | 3.17       | 0.03   | 0.03       | 0.09   | 0.08       | 0.35   | 0.31       | 2.62   | 3.32       | 0.70   | 0.34       | 1.20   | 0.94       |

1573

1574

**Table 6.**  $D_V^{ap/bt}$  values used for the vanadium species in the partitioning model.

| <b>V species</b> | <b>D surrogate</b>    | <b>D value</b> |
|------------------|-----------------------|----------------|
| $V^{3+}$         | Minimal $D_{Ga^{3+}}$ | 0.0019         |
| $V^{4+}$         | Mean $D_{Ti^{4+}}$    | 0.0004         |
| $V^{5+}$         | Least squares fitting | 0.1458         |

1575